

Combined Author Index

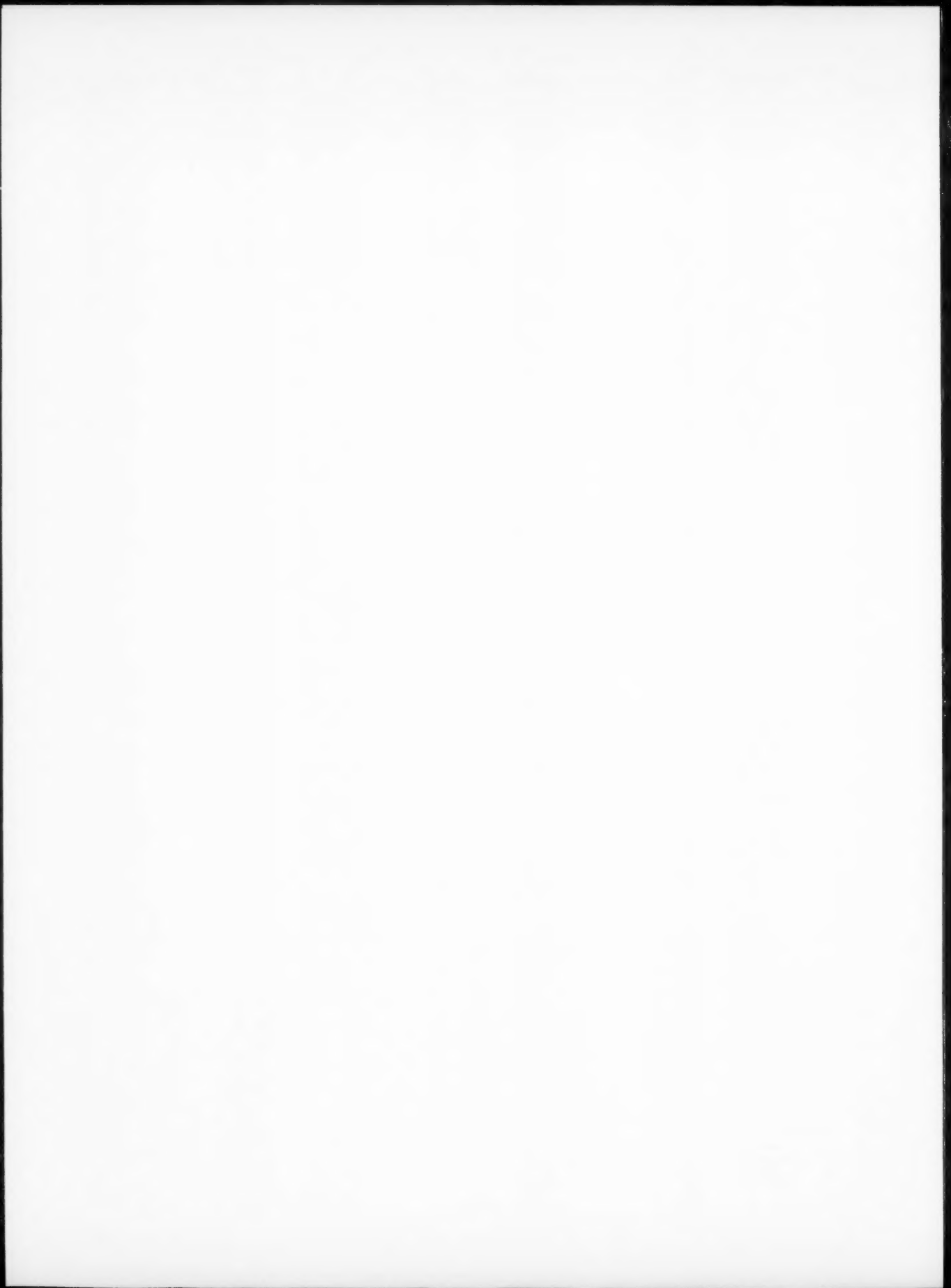
- Aaronson, H.I. 2377-2379A
 Abedian, B. 171-178B
 Ablitzer, D. 381-390B
 391-402B
 845-854B
 Achary, J. 2575-2585A
 Acosta, F.A.G. 491-502B
 503-513B
 Adiguzel, O. 349-354A
 Agarwal, A. 401-408A
 461-473A
 195-211A
 801A
 Ahn, J.P. 2361-2368A
 Ahn, S. 3041-3052A
 Akahori, T. 1937-1948A
 1949-1958A
 Ali, M. 1857-1865A
 Allison, J.A. 139-151A
 Allison, J.E. 531-540A
 951-957A
 Amadou, T. 2015-2024A
 An, G.Y. 1959-1964A
 Andes, C. 951-957A
 Andrade-Gamboa, J. 1439-1446B
 Andres, C. 531-540A
 Andrieu, E. 679-690A
 Angell, C.A. 587-596B
 Annigeri, R. 959-974A
 Ansel, D. 3198-3199A
 Apte, S.K. 35-41B
 Arai, Y. 981-991B
 Archer, R. 1133-1135B
 Ardakani, M.G. 2877-2886A
 2887-2893A
 1611-1625A
 Ares, A.E. 75-86B
 Argyropoulos, S. 87-96B
 Armster, S.Q. 1333-1344B
 Arnberg, L. 3149-3153A
 Asakuma, Y. 327-329B
 Atkinson, H.V. 2981-3000A
 Auburtin, P. 801-811B
 Babu, S.S. 161-169B
 Bae, C.M. 2665-2669A
 Bakker, A. 1475-1482B
 Balancin, O. 1353-1364A
 Ban-Ya, S. 945-955B
 Bandyopadhyay, S.K. 2405-2410A
 Banovic, S.W. 1805-1817A
 Barat, P. 2405-2410A
 Barrallier, L. 213-224A
 Barreto, J.D.J. 1505-1515B
 Barreto-Sandoval, J.D.J. 63-74B
 Barron-Meza, M.A. 63-74B
 Barsoum, M.W. 333-337A
 373-378A
 1857-1865A
 57-62A
 Basner, T. 1687-1692A
 Basu, B. 63-69A
 Baxter, W.J. 1653-1662A
 Bay, B. 2545-2557A
 Beckermann, C. 1247-1259B
 Behera, C.K. 1323-1332B
 911-920A
 Belardinelli, R. 845-854B
 Bellot, J.P. 1023-1030B
 Belton, G.R. 889-898A
 Bennett, K. 477-490B
 Berg, K.L. 171-178B
 Besson, J. 679-690A
 Bewlay, B.P. 2119-2125A
 Beynon, J.H. 1483-1490B
 Bhattacharya, B. 3001-3010A
 3011-3021A
 2163-2168A
 585-597A
 1985-1996A
 2439-2448A
 579-586B
 597-602B
 197-206B
 2917-2929A
 1419-1427B
 2545-2557A
 Boghosian, S. 597-602B
 Bojarevics, V. 179-189B
 Boom, R. 913-919B
 Bor, H.Y. 1365-1373A
 Bounds, S. 515-527B
 Bourke, M.A.M. 889-898A
 Bowen, P. 2083-2092A
 Boyce, B.L. 1571-1583A
 Boyce, D. 1543-1555A
 Braham, C. 2015-2024A
 Brewer, L. 603-607B
 Britten, S.C. 733-753B
 Brooks, C.R. 911-920A
 1307-1310A
 Bustnes, J.A. 540-542B
 Cadec, J. 2229-2237A
 Cady, C. 1007-1016A
 Cady, C.M. 2439-2448A
 Caffery, G.A. 1005-1012B
 Cahoon, J.R. 1343-1352A
 Cai, K. 253-266B
 Campbell, C.E. 2835-2847A
 Capocchi, J.D.T. 3137-3148A
 Castillejos, A.H.E. 491-502B
 503-513B
 Catalina, A. 1700-1704A
 Catalina, A.V. 2559-2568A
 Cerjak, H. 975-984A
 Cerovic, K.P. 723-731B
 Cha, P.-R. 317-326B
 Chae, D. 995-1005A
 Chai, Y.H. 1591-1597A
 Chakoumakos, B. 2739-2745A
 Chakrabarti, A.K. 1599-1610A
 Chan, K.S. 71-80A
 1075-1084A
 3029-3040A
 2615-2625A
 151-159B
 Chang, K. 2569-2574A
 Chang, K.-M. 291-298A
 Chang, S.-Y. 1519-1524A
 Chang, Y.A. 2351-2359A
 Chao, C.G. 1365-1373A
 Chatterjee, S.K. 2405-2410A
 Chattopadhyay, K. 1833-1842A
 Chattopadhyay, S.K. 2405-2410A
 Chaturvedi, M.C. 1531-1541A
 2823-2834A
 Chawla, N. 531-540A
 951-957A
 1679-1682A
 Chen, C.-M. 2351-2359A
 Chen, C.-Y. 1531-1541A
 Chen, D.L. 1025-1034A
 Chen, G.S. 2369-2376A
 Chen, L. 275-281A
 Chen, L.H. 2193-2203A
 2005-2013A
 Chen, S.-W. 1679-1682A
 Chen, S.R. 1985-1996A
 2439-2448A
 2569-2574A
 Chen, W. 1959-1964A
 Chen, Y.Y. 469-475B
 Chen, Z.-P. 1959-1964A
 Chen, Z.Y. 2449-2456A
 1907-1916A
 1135-1139B
 Cheng, L.M. 537-540B
 Chevrier, V.F. 191-196B
 Chi, R. 1163-1168B
 213-224A
 Chiron, R. 3179-3186A
 Chiu, Y.L. 1685-1687A
 Cho, W.D. 261-273A
 Choi, B.W. 355-360A
 Choi, C.-S. 2735-2738A
 2569-2674A
 Choi, S.K. 1465-1473B
 Choo, S.-H. 2849-2855A
 3041-3052A
 899-909A
 Chou, T.-W. 409-420A
 Chow, C.K. 2127-2134A
 Chowdhury, S.G. 2835-2847A
 597-602B
 179-189B
 913-919B
 1365-1373A
 515-527B
 889-898A
 2083-2092A
 1571-1583A
 1543-1555A
 2015-2024A
 603-607B
 733-753B
 911-920A
 1307-1310A
 540-542B
 2229-2237A
 1007-1016A
 2439-2448A
 1005-1012B
 1343-1352A
 253-266B
 2835-2847A
 3137-3148A
 491-502B
 503-513B
 1700-1704A
 2559-2568A
 975-984A
 723-731B
 317-326B
 995-1005A
 1591-1597A
 2739-2745A
 1599-1610A
 71-80A
 1075-1084A
 3029-3040A
 2615-2625A
 151-159B
 2569-2574A
 291-298A
 1519-1524A
 2351-2359A
 1365-1373A
 2405-2410A
 1833-1842A
 2405-2410A
 1531-1541A
 2823-2834A
 531-540A
 951-957A
 1679-1682A
 2351-2359A
 1531-1541A
 1025-1034A
 2369-2376A
 275-281A
 2193-2203A
 2005-2013A
 1679-1682A
 1985-1996A
 2439-2448A
 2569-2574A
 1959-1964A
 469-475B
 1959-1964A
 2449-2456A
 1907-1916A
 1135-1139B
 537-540B
 191-196B
 1163-1168B
 213-224A
 3179-3186A
 1685-1687A
 261-273A
 355-360A
 2735-2738A
 2569-2674A
 1465-1473B
 2849-2855A
 3041-3052A
 899-909A
 409-420A
 2127-2134A
 Christ, H.-J. 47-56A
 431-444A
 1507-1517A
 Christodoulou, N. 409-420A
 Chu, H.-S. 2587-2596A
 Chu, M. 93-98A
 Chu, Y.A. 1321-1331A
 1310-1313A
 1591-1597A
 2239-2245A
 153-161A
 Chumlyakov, Y.I. 1387-1403B
 Chung, F.K. 1925-1935A
 Chung, H.S. 763-771A
 Chung, J.C.Y. 957-971B
 Chung, Y. 853-860A
 Church, P. 1225-1232A
 Claessens, S. 641-652A
 Clark, W.A.T. 653-667A
 3063-3074A
 3075-3085A
 1201-1211A
 801-811B
 2059-2068A
 1095-1106A
 1017-1024A
 249-260A
 1429-1437B
 1419-1427B
 1917-1923A
 853-860A
 1917-1923A
 2907-2916A
 2219-2228A
 1163-1173A
 403-406B
 406-410B
 537-540B
 957-971B
 1135-1139B
 1075-1084A
 515-527B
 179-189B
 515-527B
 1965-1976A
 2205-2217A
 853-860A
 1700-1704A
 2877-2886A
 2887-2893A
 2895-2906A
 401-408A
 461-473A
 541-553A
 913-919B
 2049-2057A
 2037-2047A
 1169-1174B
 1293-1304B
 161-169B
 975-984A
 1541-1550B
 2755-2763A
 2981-3000A
 951-957A
 1543-1555A
 889-898A
 2025-2036A
 1225-1232A
 1267-1272B
 2119-2125A
 2569-2574A
 161-169B
 529-536B
 1371-1385B
 3198-3199A
 1507-1517A
 621-630B
 651-659B
 1375-1384A
 2287-2298A
 1333-1344B
 651-659B
 319-325A
 1700-1704A
 1725-1731A
 Clavel, M. 3063-3074A
 3075-3085A
 1201-1211A
 801-811B
 2059-2068A
 1095-1106A
 1017-1024A
 249-260A
 1429-1437B
 1419-1427B
 1917-1923A
 853-860A
 1917-1923A
 2907-2916A
 2219-2228A
 1163-1173A
 403-406B
 406-410B
 537-540B
 957-971B
 1135-1139B
 1075-1084A
 515-527B
 179-189B
 515-527B
 1965-1976A
 2205-2217A
 853-860A
 1700-1704A
 2877-2886A
 2887-2893A
 2895-2906A
 401-408A
 461-473A
 541-553A
 913-919B
 2049-2057A
 2037-2047A
 1169-1174B
 1293-1304B
 161-169B
 975-984A
 1541-1550B
 2755-2763A
 2981-3000A
 951-957A
 1543-1555A
 889-898A
 2025-2036A
 1225-1232A
 1267-1272B
 2119-2125A
 2569-2574A
 161-169B
 529-536B
 1371-1385B
 3198-3199A
 1507-1517A
 621-630B
 651-659B
 1375-1384A
 2287-2298A
 1333-1344B
 651-659B
 319-325A
 1700-1704A
 1725-1731A
 Cockcroft, S. 1201-1211A
 Cockcroft, S.L. 801-811B
 2059-2068A
 1095-1106A
 1017-1024A
 249-260A
 1429-1437B
 1419-1427B
 1917-1923A
 853-860A
 1917-1923A
 2907-2916A
 2219-2228A
 1163-1173A
 403-406B
 406-410B
 537-540B
 957-971B
 1135-1139B
 1075-1084A
 515-527B
 179-189B
 515-527B
 1965-1976A
 2205-2217A
 853-860A
 1700-1704A
 2877-2886A
 2887-2893A
 2895-2906A
 401-408A
 461-473A
 541-553A
 913-919B
 2049-2057A
 2037-2047A
 1169-1174B
 1293-1304B
 161-169B
 975-984A
 1541-1550B
 2755-2763A
 2981-3000A
 951-957A
 1543-1555A
 889-898A
 2025-2036A
 1225-1232A
 1267-1272B
 2119-2125A
 2569-2574A
 161-169B
 529-536B
 1371-1385B
 3198-3199A
 1507-1517A
 621-630B
 651-659B
 1375-1384A
 2287-2298A
 1333-1344B
 651-659B
 319-325A
 1700-1704A
 1725-1731A
 Combres, Y. 1095-1106A
 Cong, H.T. 1017-1024A
 Conlon, K.T. 249-260A
 Constantineau, J.P. 1429-1437B
 Coriell, S.R. 1419-1427B
 Cornish, L.A. 1917-1923A
 Cornish, R. 853-860A
 Cortie, M.B. 1917-1923A
 Courtney, T.H. 2907-2916A
 Cox, D.C. 2219-2228A
 Cragolino, G.A. 1163-1173A
 Cramb, A.W. 403-406B
 406-410B
 537-540B
 957-971B
 1135-1139B
 1075-1084A
 515-527B
 179-189B
 515-527B
 1965-1976A
 2205-2217A
 853-860A
 1700-1704A
 2877-2886A
 2887-2893A
 2895-2906A
 401-408A
 461-473A
 541-553A
 913-919B
 2049-2057A
 2037-2047A
 1169-1174B
 1293-1304B
 161-169B
 975-984A
 1541-1550B
 2755-2763A
 2981-3000A
 951-957A
 1543-1555A
 889-898A
 2025-2036A
 1225-1232A
 1267-1272B
 2119-2125A
 2569-2574A
 161-169B
 529-536B
 1371-1385B
 3198-3199A
 1507-1517A
 621-630B
 651-659B
 1375-1384A
 2287-2298A
 1333-1344B
 651-659B
 319-325A
 1700-1704A
 1725-1731A
 Ding, G.L. 2275-2285A
 Ding, H. 837-844B
 Ding, R. 197-206B
 Dippenaar, R.J. 993-1003B
 Divakar, M. 267-276B
 Doi, Y. 715-721A
 Dong, C. 15-19A
 Dong, J.X. 2135-2144A
 Dongare, M.K. 35-41B
 Dopler, T. 225-234B
 Downs, S.A. 863-872A
 Doyen, H. 1453-1459A
 Dracopoulos, V. 631-639B
 Drezet, J.-M. 1627-1634A
 Du, H. 195-211A
 801A
 Du, Y. 1795-1803A
 2907-2916A
 763-771A
 Dumitrescu, L.F.S. 615-619B
 Dunand, D.C. 781-792A
 2647-2657A
 2949-2962A
 1163-1173A
 1805-1817A
 Durand, Y. 1069-1079B
 Dutta, B. 2713-2720A
 Eadie, R.L. 1137-1145A
 Earthman, J.C. 2807-2821A
 Ebrill, N. 1069-1079B
 Ehrstrom, J.-C. 2503-2515A
 Ekroth, M. 615-619B
 El-Bealy, M. 331-343B
 345-355B
 El-Raghy, T. 333-337A
 373-378A
 1857-1865A
 1187-1194B
 Eliaz, N. 1085-1093A
 2517-2526A
 1085-1093A
 2517-2526A
 1085-1093A
 1271-1282A
 1453-1459A
 981-991B
 2299-2315A
 2785-2791A
 599-605A
 2765-2771A
 651-659B
 207-214B
 2849-2855A
 3041-3052A
 1129-1136A
 1977-1983A
 1049-1057B
 1117-1123B
 1345-1352B
 755-766B
 1081-1089B
 2678-2681A
 439-451B
 641-652A
 653-667A
 1465-1473B
 1461-1472A
 3063-3074A
 3075-3085A
 397-400A
 1283-1292B
 3129-3135A
 585-597A
 1155-1162A
 669-678A
 291-298A
 615-628A
 2025-2036A
 2145-2153A
 1231-1239B
 831-844A
 2963-2971A
 1153-1162B
 2317-2325A
 615-619B
 3129-3135A

Fruehan, R.J.	43-54B 891-898B 1059-1068B	Hata, N. Hawbolt, E.B.	1585-1589A 1247-1259A 1907-1916A	Ishikawa, T. Itagaki, K.	1261-1266B 705-712B 1231-1239B	Kim, H.S. Kim, I. Kim, J.H.	2457-2462A 1685-1687A 1107-1119A
Fujii, H.	327-329B 1585-1589A 691-701A	Hayashi, K. Hayes, P. Hayes, P.C.	299-308A 15-24B 621-630B	Ito, K. Iwasawa, K. Iza-Mendia, A.	1261-1266B 795-799B 1671-1677A	Kim, J.K. Kim, J.S.	1283-1293A 1295-1304A 1031-1047B
Fujinami, T.	2627-2636A	He, J.	1195-1201B 541-553A 555-564A	Jacob, K.T.	713-721B 1247-1259B 1323-1332B	Kim, J.Y. Kim, K.Y. Kim, S.	151-159B 2391-2394A 1107-1119A
Fukunaga, H.	3053-3061A	Heard, P.J.	615-628A	Jacot, A.	2674-2678A 1201-1211A 2059-2068A	 Kim, S.-J.	1519-1524A 1753-1760A 1713-1723A
Fukunaga, K.-I.	1937-1948A 1949-1958A	Hei, Z. Heino, S.	1193-1199A 1893-1905A 309-318A	Jahanshahi, S.	97-104B 937-943B 1105-1115B	Kim, Y.-T. Kim, Y.-W.	93-98A 2361-2368A 1635-1643A
Fukuyama, H.	25-33B 1273-1281B	Hellman, J. Hemmer, H. Henein, H.	1035-1048A 249-260A 985-994A	Jak, E.	15-24B 621-630B 1195-1201B	Kimura, S. Kipouros, G.J.	1007-1016A 1013-1021B 631-639B
Gantayat, B.P.	55-61B 21-27A	Henry, S. Herbertson, J. Hertveldt, I.	1489-1491A 487-495A 1023-1030B	Jakobsson, A.	267-276B 973-980B 439-451B	Kishi, T. Kishida, T.	2785-2791A 25-33B 2765-2771A
Gao, F.	1025-1034A 3167-3178A	Hess, E. Higo, Y.	845-854B 1435-1441A	Jaikanen, H. Jansson, B.	615-619B 2181-2192A	Kishitake, K. Klarstrom, D.L.	1307-1310A 1343-1352A
Gao, M.	1985-1996A 921-925B	Hill, M.A. Hino, M.	2457-2462A 927-935B 945-955B	Jata, K.V. Jayakumar, T. Jayaraman, N.	1053-1065A 889-896A 1345-1352B	Klassen, M. Klokkehaug, S.	1035-1048A 1733-1740A 503-510A
Garrett, R.K., Jr.	2607-2614A 3187-3193A	Hirai, T. Hirao, M.	1231-1239B 2369-2376A 1121-1128A	Jee, C.S.Y. Jena, A.K.	2127-2134A 1653-1662A	Knobloch, C. Knorr, P.	1733-1740A 503-510A 1401-1411A
Gaskell, D.R.	2093-2097A 1425-1434A	Hirosumi, T. Hirsch, T.	899-904B 1453-1459A	Jensen, D.J. Jeong, W.C.	1305-1307A 703-714A	Knowles, D.M. Ko, H.-S.	99-107A 1465-1473B 3053-3061A
Gaudett, M.A.	2247-2259A 2973-2974A	Hixson, R.S. Ho, C.-S.	845-851A 1679-1682A	Jha, S.K. Ji, F.-Z.	105-109B 837-844B	Ko, S.H. Kobayashi, T.	2669-2674A 1067-1073A 1585-1589A
Gaudette, F.G.	873-887A 1497-1506A	Ho, E.T.C. Hofer, P.	409-420A 975-984A 1353-1364A	Jia, J. Jiang, D.T.	1692-1695A 1241-1245B	Kohler-Redlich, P. Kohn, M.	1067-1073A 1585-1589A 2793-2805A
Gautier, E.	2119-2125A 3109-3122A	Hofler, P. Hoffman, W.A.M.	975-984A 1353-1364A 1203-1211B	Jiang, L. Jiang, M.-F.	1307-1310A 469-475B	Kokubo, K. Kolluru, D.V.	2793-2805A 1777-1784A 1353-1370B
Gay, H.	811-814A 2119-2125A	Holm, M. Holme, B.	339-348A 1133-1135B	Jiang, Q. Jiang, X.J.	581-584A 339-348A	Komanduri, R. Koo, J.B.	1489-1491A 2439-2448A 995-1005A
Geiger, G.H.	1867-1871A 1733-1740A	Honeyands, T. Hong, C.P.	297-305B 1107-1119A	Jin, Z. Jiricny, V.	1007-1016A 755-766B	Korzekwa, D.A. Koss, D.A.	2439-2448A 995-1005A 1883-1886A
Gell, M.	891-898B 1733-1740A	Hong, J.H. Hong, S.H.	1761-1775A 2475-2489A 2457-2462A	Johansson, J. Johnson, D.R.	1557-1570A 2463-2473A	Kozeschnik, E. Kriese, M.D.	1682-1684A 863-872A 1475-1482B
German, R.M.	1725-1731A 891-898B	Hong, S.I. Hong, T.	2457-2462A 161-169B 3123-3127A	Jonas, J.J.	511-530A 1353-1364A	Krom, A.H.M. Krupp, U.	1475-1482B 47-56A 1483-1490B
Ghosal, P.	1985-1996A 1005-1012B	Hong, Y.S. Hono, K.	607-614A 691-701A 1725-1731A	Jones, H.	1375-1384A 327-328A	Krzyzanowski, M. Kucharova, K.	2229-2237A 15-24B 747-753A
Ghosh, A.K.	679-690A 1007-1016A	Horita, Z. Horstemeyer, M.F.	691-701A 1725-1731A 1353-1370B	Jones, J.W.	2155-2162A 531-540A	Kudo, M. Kudoh, M.	15-24B 747-753A 71-80A
Ghosh, P.K.	1985-1996A 1997-2003A	Hou, Z.B. Houzelot, J.-L.	1353-1370B 381-390B 391-402B	Jones, P.T.	951-957A 1741-1752A	Kumar, K.S. Kumazawa, N.	71-80A 2627-2636A 151-159B
Ghosh, S.	2439-2448A 2503-2515A	Howden, D.G.	641-652A 653-667A 2377-2379A	Jonsson, L.	197-206B 867-875B	Kumta, P.N. Kunze, J.M.	151-159B 1271-1282A 275-281A
Ghosh, L.J.	1627-1634A 2963-2971A	Howe, J.M. Howell, P.R.	653-667A 2377-2379A 995-1005A	Jordan, A.	2739-2745A 2747-2754A	Kuo, B.C. Kwon, S.-J.	275-281A 793-798A 1107-1119A
Gialanella, S.	285-295B 1035-1048A	Howe, J.M. Hozawa, M.	995-1005A 327-329B 2661-2665A	Jordan, E.	2388-2391A 445-459A	Kwon, Y. Laboudigue, B.	93-98A 207-214B 827-836B
Gigliotti, M.F.X.	1095-1106A 1627-1634A	Hryniewicz, T. Hsiao, I.C.	2661-2665A 2169-2180A 475-485A	Jordinson, C.	445-459A 2037-2047A	Lacaze, J.	207-214B 827-836B 15-19A
Gill, T.P.S.	1627-1634A 1405-1417B	Hsieh, S.H. Hu, H.	475-485A 723-733A 1473-1478A	Joshi, S.V.	911-920A 327-328A	Lacaze, J.	827-836B 15-19A 1333-1344B
Gilman, J.J.	2545-2557A 1147-1154A	Hu, H. Hu, S.C.	723-733A 1473-1478A 2169-2180A	Joy, D.C.	327-328A 3041-3052A	Lai, J.K.L. Lai, W.-H.L.	15-19A 1333-1344B 2597-2606A
Gilmore, R.S.	3063-3074A 3075-3085A	Huang, J.C. Huang, S.	2169-2180A 1241-1245B 3155-3166A	Juarez-Hernandez, A.	327-328A 3041-3052A	Lam, Y.C.	2597-2606A 411-414B 414-418B
Gjunter, V.E.	1447-1455B 1457-1464B	Huang, S. Huang, X.	1241-1245B 3155-3166A 2295-2315A	Jung, J.-Y.	3041-3052A 1713-1723A	Langberg, D.E.	411-414B 414-418B 419-424B
Glatzel, U.	599-605A 837-844B	Huh, M.-Y. Huin, D.	2295-2315A 905-912B 29-34A	Jung, Y.-C.	1713-1723A 1700-1704A	Langdon, T.G.	691-701A 361-371A 387-396A
Glaw, P.C.	1447-1455B 1457-1464B	Hunt, J.D. Hutchinson, C.R.	905-912B 29-34A 2721-2733A	Kale, B.B.	421-430A 35-41B	Laughlin, D.E.	361-371A 387-396A 541-553A
Glock, K.	599-605A 837-844B	Hutchinson, C.R. Hutchinson, J.W.	2721-2733A 1129-1136A 793-798A	Kamiya, R.	899-909A 913-919B	Laverman, E.J.	541-553A 555-564A 723-733A
Glock, K.	1733-1740A 1725-1731A	Hwang, K.C. Hwang, K.S.	793-798A 1473-1478A 1645-1652A	Kamperman, A.A.	913-919B 99-107A	 Lee, C.S.	555-564A 723-733A 1333-1344B
Gokhale, A.M.	891-898B 1985-1996A	Hwang, N.M. Hwang, S.K.	985-994A 1925-1935A 171-178B	Kang, S.-B.	99-107A 1107-1119A	Lee, H.-I.	1843-1855A 2287-2298A 2681-2686A
Goldstein, D.	1005-1012B 679-690A	Hyers, R.W. Ice, M.	171-178B 541-553A 555-564A	Kang, S.Y.	1107-1119A 35-45A	Lee, H.-I.	2681-2686A 2917-2929A 381-390B
Goto, D.M.	1007-1016A 1985-1996A	Ichino, R. Igarashi, T.	541-553A 235-241B 715-721A	Kapoor, R.	815-823A 1695-1700A	Lee, H.-I.	381-390B 391-402B 2015-2024A
Grace, J.R.	1985-1996A 1005-1012B	Iguchi, M. Ikeda, K.	715-721A 453-460B 1635-1643A	Kaplay, G.	1695-1700A 3087-3090A	Lee, C.S.	2665-2669A 1479-1488A 475-485A
Grange, M.	1007-1016A 1985-1996A	Ilegbushi, O.J. Imaishi, N.	2069-2074A 327-329B 1949-1958A	Kar, T.	3087-3090A 35-45A	Lee, H.B.	475-485A 1479-1488A 2361-2368A
Gray, G.T., III	1447-1455B 1457-1464B	Inagaki, I. Inoue, A.	1949-1958A 607-614A 2463-2473A	Karlsson, T.	35-45A 1233-1246A	Lee, H.C.	1479-1488A 2361-2368A 1479-1488A
Gregson, P.J.	599-605A 837-844B	Inui, H. Iost, A.	2463-2473A 153-161A 1447-1455B	Kasai, N.	453-460B 1997-2003A	Lee, J.-C.	225-237A 2361-2368A 503-510A
Gremaud, M.	1692-1695A 1345-1352B	Irons, G.A. Isac, M.	1447-1455B 1457-1464B 1031-1047B	Kaschner, G.C.	216-218B 1053-1065A	Lee, J.-E.	793-798A 1107-1119A 1753-1760A
Grensing, F.C.	2647-2657A 1819-1832A	Isac, M. Ishibashi, H.	1031-1047B 299-308A 216-218B	Kashwaya, Y.	216-218B 1053-1065A	Lee, S.	1753-1760A 2475-2489A 2669-2674A
Griffiths, W.D.	1035-1048A 1095-1106A	Ishii, K.	216-218B	Katipelli, L.R.	461-473A 235-241B	 Lee, S.	2475-2489A 2669-2674A 2669-2674A
Gron, O.	1095-1106A 1627-1634A	 	 	Kato, S.	235-241B 1419-1427B	 Lebas, E.	 381-390B 391-402B
Grosdidier, T.	1627-1634A 1405-1417B	 	 	Kattnr, U.R.	565-573A 2005-2013A	 Ledion, J.	 2015-2024A
Grun, G.-U.	1405-1417B 2545-2557A	 	 	Katz, R.N.	565-573A 2005-2013A	Lee, C.S.	2665-2669A 1479-1488A 475-485A
Gruendmann, R.	1405-1417B 2545-2557A	 	 	Kawagishi, N.	2005-2013A 349-354A	Lee, H.C.	1479-1488A 2361-2368A 1479-1488A
Gu, J.P.	2545-2557A 1147-1154A	 	 	Kayali, N.	349-354A 1497-1506A	Lee, H.C.	1479-1488A 2361-2368A 503-510A
Guduru, P.R.	1147-1154A 3063-3074A	 	 	Kazior, J.	1497-1506A 1293-1304B	Lee, J.-C.	225-237A 2361-2368A 503-510A
Guillemer-Neel, C.	3063-3074A 3075-3085A	 	 	Kermanpur, A.	1293-1304B 1283-1293A	Lee, J.C.	2361-2368A 503-510A 793-798A
Guilemot, F.	1447-1455B 1457-1464B	 	 	Kestursatya, M.	1283-1293A 2755-2763A	Lee, S.	1107-1119A 1753-1760A 2475-2489A
Guo, D.	599-605A 837-844B	 	 	Khaleel, M.A.	2755-2763A 1517-1525B	 Lee, S.	 1107-1119A
Guo, H.	837-844B 1692-1695A	 	 	Khanna, R.	1517-1525B 1925-1935A	 Lee, S.	 1107-1119A
Guo, J.	1345-1352B 1873-1881A	 	 	Kim, B.K.	1925-1935A 3041-3052A	 Lee, S.	 1107-1119A
Guo, J.T.	2247-2259A 357-364B	 	 	Kim, C.K.	3041-3052A 2475-2489A	 Lee, S.	 1107-1119A
Guo, Z.X.	767-777B 855-866B	 	 	Kim, D.-K.	2475-2489A	 Lee, S.	 1107-1119A
Gupta, M.	1031-1047B 1143B	 	 	 	 	 Lee, S.	 1107-1119A
Gupta, S.R.	1671-1677A 29-34A	 	 	 	 	 Lee, S.	 1107-1119A
Guthrie, R.I.L.	531-540A 327-329B	 	 	 	 	 Lee, S.	 1107-1119A
 	267-276B 1121-1128A	 	 	 	 	 Lee, S.	 1107-1119A
 	2647-2657A 1819-1832A	 	 	 	 	 Lee, S.	 1107-1119A
 	763-771A 381-390B	 	 	 	 	 Lee, S.	 1107-1119A
 	391-402B 2931-2941A	 	 	 	 	 Lee, S.	 1107-1119A
 	173-178A 1741-1752A	 	 	 	 	 Lee, S.	 1107-1119A
 	747-753A	 	 	 	 	 Lee, S.	 1107-1119A

	2849-2855A	Ma, C.Y.	1365-1373A	Morris, J.W., Jr.	798-800A	Pagounis, E.	309-318A
	3041-3052A	Mabuchi, M.	715-721A		2697-2711A	Pal, U.B.	733-753B
Lee, S.B.	985-994A	MacEwen, S.	1543-1555A	Morsi, K.	1663-1670A	Palaflox-Ramos, J.	1505-1515B
Lee, S.M.	297-305B	MacLachlan, D.W.	1401-1411A	Mortensen, A.	397-400A	Palmer, T.A.	1371-1385B
Lee, S.P.	2075-2081A	Maeda, M.	795-799B	Moshe, E.	1085-1093A	Pan, C.	2537-2543A
Lee, T.-H.	1713-1723A	Magnin, T.	2025-2036A	Mosher, D.A.	1725-1731A	Pan, Y.-M.	1163-1173A
Lee, Y.-K.	355-360A	Mahajan, Y.R.	629-639A	Moskovic, R.	445-459A	Pandey, A.B.	921-936A
	2735-2738A	Mahata, T.	551-553B	Motta, A.T.	1883-1886A		937-950A
Lee, Y.C.	2895-2906A	Maier, H.J.	139-151A	Moynihan, C.T.	587-596B	Papatheodorou, G.N.	631-639B
Lee, Z.H.	723-733A		431-444A	Mueller, B.A.	1419-1427B	Paramguru, R.K.	55-61B
Leonard, K.J.	1305-1321B	Maijer, D.	1201-1211A	Mughrabi, H.	585-597A	Paraventi, D.J.	2383-2388A
Lesuer, D.R.	63-69A		2059-2068A	Mukerji, S.	3087-3090A	Pasewicz, H.U.	891-898B
Leverant, G.R.	3029-3040A	Maire, E.	249-260A	Mukherjee, P.	2405-2410A	Pasquevich, D.M.	1439-1446B
Levey, F.C.	1917-1923A	Majima, H.	5-13B	Mukherjee, S.	2559-2568A	Patankar, S.N.	2394-2396A
Levi, M.R.	409-420A	Majumdar, B.	1833-1842A	Mukhopadhyay, A.K.	2093-2097A	Patisson, F.	381-390B
Li, B.	387-396A	Majumdar, B.S.	921-936A		25-33B		391-402B
	1491-1503B		937-950A	Murty, B.S.	319-325A	Pauty, E.	207-214B
	1843-1855A	Makhoul, M.M.	565-573A	Mustoe, G.G.W.	433-438B	Pech-Canul, M.I.	565-573A
	2681-2686A	Male, A.T.	2537-2543A	Nabeshima, Y.	1013-1021B	Pehlke, R.	57-62A
Li, B.-Y.	1867-1871A	Mannan, S.	2569-2574A	Nagai, K.	2793-2805A	Pelleg, J.	1525-1530A
Li, D.	1959-1964A	Mannan, S.L.	1175-1185A	Nagamori, M.	543-546B	Pelton, A.D.	621-630B
	2205-2217A		3109-3122A	Nagasaka, T.	927-935B		651-659B
Li, D.Y.	2773-2783A	Manthiram, A.	2396-2398A		945-955B	Perepezko, J.H.	497-501A
Li, G.	2491-2502A	Marder, C.S.	397-400A	Nagata, K.	25-33B	Perez, R.	1551-1553B
Li, J.D.	581-584A	Marder, A.R.	1805-1817A		1273-1281B	Pericleous, K.	179-189B
Li, L.	546-551B	Martorano, M.A.	3137-3148A	Nahme, H.	831-844A		515-527B
Li, L.-F.	469-475B	Masuda, C.	2637-2645A	Nair, S.F.	551-553B	Perocchi, L.	3029-3040A
Li, M.	357-364B	Masuda, Y.	2463-2473A	Naito, K.	2765-2771A	Peters, J.O.	1571-1583A
	767-777B	Matan, N.	2219-2228A	Najjar, D.	153-161A	Philippe, M.-J.	1095-1106A
	855-866B	Mathew, M.D.	1175-1185A	Nakajima, K.	1013-1021B	Pieczonka, T.	1497-1506A
	1143B	Matsumoto, T.	299-308A	Nakamura, N.	715-721A	Pilkey, A.K.	831-844A
	1385-1399A		327-329B	Nakano, T.	1585-1589A	Ping, D.H.	607-614A
Li, S.	99-107A		1585-1589A	Nam, J.	93-98A	Pinol-Juez, A.	1671-1677A
	2449-2456A	Matsushita, K.	5-13B	Nam, J.G.	503-510A	Pistorius, P.C.	1091-1097B
Li, T.-X.	1527-1533B	Matsuura, K.	747-753A	Nam, S.W.	1761-1775A	Pitman, S.G.	2755-2763A
	1535-1540B	Matsuzaki, K.	1261-1266B	Nam, W.J.	2665-2669A	Poirier, D.R.	1283-1292B
Li, Y.	1049-1057B	Mayr, P.	1453-1459A	Namjoshi, S.A.	307-316B		3129-3135A
	1059-1068B	Maziasz, P.	2739-2745A	Nemat-Nasser, S.	815-823A	Poole, W.J.	2327-2338A
	1067-1073A		2747-2754A	Nemoto, M.	691-701A	Prakash, D.	551-553B
Li, Y.-Y.	2155-2162A	Mazumdar, P.	1233-1246A	Newman, D.S.	597-602B	Prasad, K.S.	2093-2097A
Li, Z.	1867-1871A	McElhaney, K.W.	1333-1342A	Nexhip, C.	1105-1115B	Prasad, V.	735-746A
Liang, J.	2943-2948A	McHargue, C.J.	911-920A	Ngan, A.H.W.	3179-3186A	Prasad, Y.V.R.K.	629-639A
Liaw, P.K.	1163-1168B	McKay, J.	1133-1135B	Nicolaou, P.D.	1425-1434A		2317-2325A
	911-920A	McKeivay, A.L.	1413-1423A	Nie, J.F.	2377-2379A	Pritzker, M.	683-691B
	1307-1310A	McLean, A.	239-248A	Nielsen, O.	3149-3153A		693-703B
	213-224A	McLean, M.	1663-1670A	Nightingale, R.J.	993-1003B	Priya, S.	2674-2678A
Lillamand, I.	2394-2396A		2877-2886A	Niinomi, M.	1937-1948A	Procopio, A.T.	333-337A
Lim, C.T.	2659-2661A		2887-2893A	Niinomi, M.	1949-1958A		373-378A
Lim, L.C.	1679-1682A	McShane, H.B.	1663-1670A	Nilsson, J.-O.	35-45A	Pryds, N.H.	3155-3166A
Lin, C.-H.	475-485A	Meadowcroft, T.R.	1005-1012B	Nishiaki, M.	5-13B	Purdy, G.R.	1187-1192A
Lin, C.S.	1692-1695A		1247-1259A	Nisitani, H.	2005-2013A	Puscas, T.M.	3091-3099A
Lin, D.L.	291-298A		1907-1916A	Niu, H.J.	2615-2625A	Qian, M.	2659-2661A
Lin, S.-J.	2193-2203A	Medeiros, S.C.	2317-2325A	Noble, B.	339-348A		3195-3197A
Lin, S.C.	2917-2929A	Mediaas, H.	631-639B	Nogi, K.	327-329B	Qiang, J.	1193-1199A
Lin, Y.J.	309-318A	Meikap, A.K.	2405-2410A		1585-1589A	Qin, J.	2163-2168A
Lindroos, V.K.	1873-1881A	Meisenkothen, F.	2963-2971A	Noh, J.-W.	2475-2489A	Qing, X.	139-151A
Ling, P.S.	1883-1886A	Meyer, B.C.	1453-1459A	Norlund, C.A.	1261-1269A	Qiu, H.	2785-2791A
Link, T.M.	2449-2456A	Meyrick, G.	2963-2971A	Nykiel, T.	2661-2665A	Quaresma, J.M.V.	3167-3178A
Liu, C.M.	837-844B	Miao, W.F.	361-371A	O'Keefe, T.J.	1203-1211B	Queheillat, D.T.	261-273A
Liu, G.	1163-1168B	Michaud, V.	225-234B	O, J.M.	2527-2536A	Ra, H.Y.	1479-1488A
Liu, J.	2607-2614A	Miettinen, J.	365-379B	Oden, M.	1557-1570A	Rabiei, A.	1129-1136A
	3187-3193A	Militzer, M.	1247-1259A	Ogi, H.	1121-1128A	Racz, L.M.	171-178B
Liu, K.-S.	2587-2596A	Miller, M.K.	975-984A	Oh, H.	793-798A	Radhakrishna Bhat, B.V.	629-639A
Liu, P.L.	2857-2866A	Mills, K.C.	111-119B	Oh, K.H.	225-237A	Radjai, A.	755-762A
	2867-2875A	Minor, A.M.	798-800A		779-794B	Radmilovic, V.	2697-2711A
Liu, R.	2773-2783A	Miracle, D.B.	921-936A		1479-1488A	Rae, C.M.F.	2219-2228A
Liu, X.	309-318A	Mishin, O.V.	1653-1662A	Oh, S.J.	793-798A	Rainforth, W.M.	2155-2162A
Liu, Y.	837-844B	Mishurda, J.C.	1305-1321B		1107-1119A	Raj, B.	1053-1065A
	3187-3193A	Misra, P.	1135-1139B	Oh, Y.J.	1761-1775A	Raj, S.V.	873-887A
Liu, Y.-F.	2637-2645A	Mitchell, A.	801-811B	Ohmi, T.	747-753A	Rama Rao, V.V.	2093-2097A
Liu, Y.Y.	1959-1964A	Mittlin, D.	2697-2711A	Ojha, S.N.	2275-2285A	Randhawa, H.S.	2247-2259A
Liu, Z.	2739-2745A	Mitra, M.K.	2405-2410A	Okabe, T.H.	713-721B	Rangaswamy, P.	889-898A
Looee, R.	1785-1794A	Mittmeijer, E.J.	2049-2057A	Okada, H.	2627-2636A	Rankin, W.J.	411-414B
Loomans, M.E.	1075-1084A	Miwa, K.	755-762A	Okafor, I.C.I.	3023-3028A		414-418B
Lopez-Ramirez, S.	1155-1162A	Miyazaki, S.	2423-2430A	Okane, T.	1491-1503B		419-424B
Lossius, L.P.	1505-1515B	Mizoguchi, S.	1013-1021B	Okido, M.	235-241B	Rao, K.B.S.	1175-1185A
Lowe, T.C.	1213-1224B	Mo, A.	1461-1472A	Okuda, K.	599-605A	Rao, K.P.	763-771A
Lu, B.	675-682B	Modaressi, A.	225-234B	Oliver, H.E.	2755-2763A	Rao, S.B.	55-61B
Lu, S.	2205-2217A	Mohamed, F.A.	163-172A	Olsen, S.E.	477-490B	Rapp, R.A.	2105-2118A
Lu, S.Z.	5-13A		2807-2821A	Olson, G.B.	1321-1331A	Rappaz, M.	487-495A
Lu, W.-K.	2907-2916A	Molinari, A.	1497-1506A	Ong, M.S.	2155-2162A		1293-1304B
Lu, Y.C.	993-1003B		3091-3099A	Ongstott, J.	71-80A		1627-1634A
Lucas, J.A.	1645-1652A	Moore, J.J.	433-438B	Oo, M.K.K.	1873-1881A	Ratchey, I.P.	1049-1057B
	1049-1057B	Moorthy, V.	1053-1065A	Orring, C.	403-406B	Rath, P.C.	55-61B
	1059-1068B	Morales, R.D.	63-74B	Ostrovski, O.	129-139B	Ravichandran, G.	1147-1154A
	1117-1123B		1505-1515B		1139-1142B	Ravichandran, K.S.	703-714A
	1125-1131B	Moran, B.	1321-1331A	Ostfold, T.	631-639B	Ray, R.K.	2127-2134A
Luck, R.	1067-1073A	Moran, G.	515-527B	Overfelt, R.A.	546-551B		2339-2350A
Lui, T.S.	275-281A	Morere, B.	2503-2515A	Oya-Seimiya, Y.	1435-1441A		3001-3010A
	2193-2203A	Mori, H.	2785-2791A	Oye, H.A.	641-650B		3011-3021A
Luo, Z.	5-13A	Morita, K.	899-904B		1213-1224B	Reddy, R.G.	3023-3028A
Lynch, N.	853-860A	Morrall, J.E.	1187-1192A	Ozguven, N.	1345-1352B	Reed, R.A.S.	109-123A

- Reed, R.C. 2219-2226A
2261-2273A
Reid, A.C.E. 1321-1331A
Reimanis, I.E. 433-438B
Rettenmayr, M. 2713-2720A
Reye, J. 2275-2285A
Rhodes, C.G. 2931-2941A
Rhouma, A.B. 2015-2024A
Riboud, P.V. 905-912B
Rielly, C.D. 1117-1123B
Rigby, G.D. 1117-1123B
Ringer, S.P. 2721-2733A
Rist, M.A. 2219-2228A
Ritchie, R.O. 1413-1423A
1571-1583A
Rivas, J.M. 845-851A
Ro, Y. 173-178A
Robelin, C. 651-659B
Roberts, S.M. 2261-2273A
Robinson, S. 1843-1855A
2681-2686A
1571-1583A
Roder, O. 1543-1555A
Rogge, R. 705-712B
Roghani, G. 1283-1293A
Rohatgi, P.K. 1295-1304A
1867-1871A
Rong, L.-J. 1551-1553B
Rosas, G. 669-678A
Roven, H.J. 755-766B
Roy, A. 1405-1417B
Rudiger, F. 1067-1073A
Ruhle, M. 2181-2192A
Rutter, J.W. 239-248A
Ryoo, H.S. 1925-1935A
Ryu, H.J. 2475-2489A
Sachdev, A. 57-62A
Saeter, J.A. 2327-2338A
Sahajwalla, V. 215-216B
243-251B
1099-1104B
1133-1135B
1517-1525B
Sahoo, K.L. 1599-1610A
Sahu, K.K. 1169-1174B
Saiz, E. 299-308A
Sakai, Y. 327-329B
Sakata, K. 1213-1223A
Salishchev, G.A. 2119-2125A
Samarasekera, I.V. 1005-1012B
Sampath, S. 735-746A
Sandstrom, R. 2423-2430A
Sankaran, K.K. 2181-2192A
Sano, N. 899-904B
Santos, C.A. 3167-3178A
Sanuki, S. 5-13B
Sarma, B. 891-898B
Sasaki, Y. 216-218B
Sasikala, G. 1175-1185A
Satyanarayana, D.V.V. 1777-1784A
Schlichting, K. 2388-2391A
Schlogl, S.M. 125-137A
Schmauder, S. 2943-2948A
Schuh, C. 2411-2421A
2647-2657A
Schulze, V. 825-830A
Schuster, J.C. 1795-1803A
Schwezo, C.E. 1611-1625A
Schwartz, D.S. 261-273A
Schwerdtfeger, K. 461-468B
813-826B
Sciffer, S.D. 1117-1123B
Scully, J.R. 81-92A
179-193A
Seetharaman, S. 105-109B
111-119B
267-276B
540-542B
973-980B
139-151A
827-836B
Sellars, C.M. 1483-1490B
Semiati, S.L. 1425-1434A
Semoroz, A. 487-495A
Sen, P. 2405-2410A
Sen, S. 1700-1704A
Sengupta, S. 239-248A
Seok, H.-K. 1479-1488A
Seol, D.J. 779-794B
Sha, H. 813-826B
Shang, B. 5-13A
Shang, J.K. 2857-2866A
Shankar, V. 2867-2875A
3109-3122A
Sharma, B.P. 551-553B
Sharma, S.C. 773-780A
Shek, C.H. 15-19A
Shen, H.F. 297-305B
Shen, Y.-L. 531-540A
Sheng, D.Y. 867-875B
Shengjie, Y. 2597-2606A
Shepard, M.J. 2931-2941A
Shi, C.X. 1692-1695A
Shi, Z. 2361-2368A
Shibata, H. 981-991B
Shibue, K. 3053-3061A
Shimojo, M. 1435-1441A
Shiohara, Y. 141-149B
Shiozawa, K. 1137-1145A
Shiue, R.K. 2527-2536A
Shollock, B.A. 2877-2886A
2887-2893A
Shook, A.A. 1005-1012B
Shu, D. 1527-1533B
1535-1540B
1959-1964A
Shu, Q. 105-109B
Sichen, D. 111-119B
540-542B
973-980B
Siciliano, F., Jr. 511-530A
Sidhom, H. 2015-2024A
Sietsma, J. 379-385A
Sinclair, C.W. 1187-1192A
Sinclair, I. 109-123A
2503-2515A
Sinder, M. 1525-1530A
Singh Raman, R.K. 3101-3108A
Singh, A.K. 1687-1692A
Singh, V. 2037-2047A
Sista, S. 529-536B
Sivaramakrishnan, C.S. 1599-1610A
Skjervold, S. 2327-2338A
Skupien, D. 921-925B
Smith, A.F.M. 445-459A
Smith, M.T. 2755-2763A
Smith, P.R. 2931-2941A
Smith, S.W. 179-193A
Smith, T. 139-151A
Soboyejo, W.O. 1385-1399A
Soda, H. 239-248A
Sohn, H.Y. 543-546B
Sohn, Y.H. 2388-2391A
Soltanleh, M. 121-128B
Somers, M.A.J. 195-211A
801A
Sommer, F. 277-284B
Sonawane, R.S. 35-41B
Song, B. 21-27A
Song, J.M. 275-281A
Spanos, G. 2145-2153A
Sponser, S. 2739-2745A
Sprauel, J.M. 213-224A
Sridhar, N. 1163-1173A
Sridhar, R. 121-128B
Sridhar, S. 111-119B
406-410B
1135-1139B
959-974A
Srivatsan, T.S. 2895-2906A
St. John, D.H. 1965-1976A
Starke, E.A., Jr. 1700-1704A
Stefanescu, D.M. 2559-2568A
Stephens, D.A. 445-459A
Stolk, J. 2396-2398A
Stone, H.J. 2261-2273A
Story, S.R. 43-54B
891-898B
Straffolini, G. 1443-1451A
1497-1506A
3091-3099A
1023-1030B
1069-1079B
1081-1089B
1117-1123B
1125-1131B
1125-1131B
2491-2502A
2169-2180A
837-844B
153-161A
Sugimoto, S. 1785-1794A
Suito, H. 1213-1223A
Sumida, M. 141-149B
Sun, B.-D. 1527-1533B
1535-1540B
Sun, M. 1017-1024A
Sun, S. 97-104B
937-943B
1105-1115B
1137-1145A
1017-1024A
Sun, Y.K. 2379-2383A
Sundaresan, S. 3109-3122A
Sung, P.K. 1283-1292B
Suresh, S. 1977-1983A
Susa, M. 25-33B
1273-1281B
2339-2350A
1139-1142B
981-991B
Suzuki, T. 2793-2805A
Sylilusarenko, S.I. 2163-2168A
Syn, C.K. 63-69A
Tafto, J. 339-348A
Takano, C. 1267-1272B
Takasu, T. 121-128B
Takeda, Y. 15-24B
705-712B
927-935B
Takida, T. 715-721A
Tam, K.C. 2597-2606A
Tan, M.J. 2394-2396A
Tanaka, Y. 2637-2645A
Tang, W. 2423-2430A
Taniguchi, S. 253-266B
Tavarez, R.P. 1031-1047B
Tavera, F.J. 1551-1553B
Tempus, G. 1453-1459A
Terrance, A.L.E. 3109-3122A
Tetenbaum, M. 661-666B
Teter, D.F. 667-673B
Teteruk, R.G. 431-444A
Tewari, S.N. 2275-2285A
Thadhani, N.N. 307-316B
Thakur, S.K. 319-325A
Thess, A. 1541-1550B
Thissell, W.R. 845-851A
Thoma, D.J. 667-673B
Thomas, B.G. 2491-2502A
Thompson, A.W. 1571-1583A
Thompson, R.G. 2135-2144A
609-613B
631-639B
299-308A
3053-3061A
121-128B
216-218B
2299-2315A
299-308A
845-851A
433-438B
Trivedi, R. 1233-1246A
1261-1269A
1819-1832A
75-86B
87-96B
2239-2245A
2239-2245A
1785-1794A
327-329B
1261-1266B
597-602B
409-420A
863-872A
877-879B
713-721B
141-149B
1491-1503B
1785-1794A
2793-2805A
1187-1194B
2747-2754A
2739-2745A
2388-2391A
1053-1065A
125-137A
379-385A
125-137A
379-385A
913-919B
Van Veen, A. 1271-1282A
Vancheswaran, R. 1293-1304B
Varahram, N. 1305-1321B
Varadevan, V.K. 2377-2379A
1405-1417B
Venkatesh, T.A. 781-792A
Venkateswara Rao, K.T. 1413-1423A
Venkert, A. 1147-1154A
Venugopalan, D. 2575-2585A
Verheoven, J.D. 2431-2438A
Vermaak, M.K.G. 1091-1097B
Viswanathan, N.N. 540-542B
973-980B
1225-1230B
153-161A
Vohringer, O. 825-830A
Volinsky, A.A. 863-872A
Von Dreele, R. 889-898A
Vooijs, S.I. 379-385A
Voorhees, P.W. 1333-1342A
Vracar, R.Z. 723-731B
Wadley, H.N.G. 261-273A
1271-1282A
1025-1034A
735-746A
Wan, K.-C. 1307-1310A
Wang, H. 1527-1533B
Wang, J. 1535-1540B
2527-2536A
1193-1199A
5-13A
Wang, L. 1310-1313A
Wang, R. 801-811B
Wang, S.C. 2163-2168A
Wang, T. 469-475B
Wang, W.-Z. 2943-2948A
Wanner, A. 2949-2962A
2383-2388A
713-721B
2674-2678A
1273-1281B
2627-2636A
339-348A
2327-2338A
1067-1073A
Wei, B. 235-241B
Wei, D. 1387-1403B
Wei, P.S. 1025-1034A
Wei, R.P. 2423-2430A
Wei, Z.G. 283-289A
Welham, N.J. 3023-3028A
Wen, X. 1310-1313A
Weng, W.P. 723-733A
White, D.R. 2917-2929A
Whitesell, H.S. 546-551B
Whittington, B.I. 1175-1186B
Wiblen, R. 1099-1104B
Wiezorek, J.M.K. 2963-2971A
Wild, R.K. 615-628A
Wilkinson, D.S. 249-260A
Williams, M.E. 1419-1427B
Wilson, A. 35-45A
Wilson, A.L. 995-1005A
Witusiewicz, V.T. 277-284B
Wollants, P. 197-206B
Won, Y.M. 779-794B
Wong, K.W. 15-19A
Worswick, M.J. 831-844A
Wright, S. 97-104B
Wu, C. 215-216B
243-251B
1099-1104B
2239-2245A
Wu, C.S. 497-501A
Wu, R.I. 2527-2536A
Wu, S.K. 2083-2092A
Wu, X. 109-123A
Wu, X.D. 3123-3127A
Wu, X.L. 21-27A
Xia, K. 2135-2144A
Xie, X.S. 2369-2376A
Xiong, H. 2391-2394A
Xu, H. 1241-1245B
Xu, K. 1193-1199A
Xu, X. 21-27A
Xu, Y. 191-196B
Xu, Z. 1163-1168B
2857-2866A
1527-1533B
1535-1540B
Yamabe-Mitarai, Y. 173-178A
Yamaguchi, K. 15-24B
Yamaguchi, M. 2463-2473A
Yamanaka, T. 2463-2473A
Yan, X.Y. 411-414B
414-418B
419-424B

Yang, J.	2069-2074A	Yoon, D.Y.	985-994A	Zacharias, D.	1505-1515B		1195-1201B
Yang, M.C.	1017-1024A		1489-1491A	Zavaliangos, A.	877-879B	Zhao, M.	581-584A
Yang, N.	1843-1855A	Yoon, J.-K.	225-237A	Zeitler, S.	1507-1517A	Zhao, W.	911-920A
	2681-2686A		317-326B	Zeng, F.	5-13A	Zhou, C.	2391-2394A
Yang, R.	2205-2217A	Yoon, U.-S.	225-237A	Zeng, Z.	1163-1168B	Zhou, Y.-H.	1527-1533B
Yang, W.	2569-2574A	Yoshida, M.	2075-2081A	Zengin, R.	349-354A		1535-1540B
Yang, Z.	529-536B	You, J.	1241-1245B	Zhang, G.	129-139B		191-196B
Yeh, J.-W.	2587-2596A	Younes, C.	615-628A	Zhang, J.	1139-1142B	Zhou, Z.	2449-2456A
Yeh, M.S.	1310-1313A	Young, D.	1133-1135B	Zhang, L.	97-104B	Zhou, Z.P.	191-196B
	1591-1597A	Yousefiani, A.	163-172A		253-266B	Zhu, G.	2229-2237A
	2239-2245A		2807-2821A		2369-2376A	Zhu, S.J.	675-682B
Yeo, T.-J.	225-237A	Yu, L.	2275-2285A	Zhang, X.D.	2963-2971A	Zhu, Y.T.	1541-1550B
	779-794B	Yu, S.C.M.	2597-2606A	Zhang, X.M.	2449-2456A	Ziegler, D.P.	1541-1550B
Yokoyama, H.	2793-2805A	Yu, X.H.	173-178A	Zhang, Y.G.	2823-2834A	Zikanov, O.	845-851A
Yonezawa, K.	461-468B	Yu, Z.	1193-1199A	Zhang, Y.M.	2537-2543A	Zurek, A.K.	
Yoo, C.D.	1465-1473B	Yuan, R.	2369-2376A	Zhao, B.	621-630B		



Combined Subject Index

- Absorption (material), Microstructural effects**
The identification of hydrogen trapping states in an Al-Li-Cu-Zr alloy using thermal desorption spectroscopy. 179-193A
- Accuracy**
Stress-strain response of a cast 319-T6 aluminum under thermomechanical loading. 139-151A
Dissolution rates of coals and graphite in Fe-C-S melts in direct ironmaking: dependence of carbon dissolution rate on carbon structure. 215-216B
Modeling of interdendritic strain and macrosegregation for dendritic solidification processes. I. Theory and experiments. 331-343B
Modeling of interdendritic strain and macrosegregation for dendritic solidification processes. II. Computation of interdendritic strain and segregation fields in steel ingots. 345-355B
Damage leading to ductile fracture under high strain-rate conditions. 831-844A
Evaporation behavior of aluminum during the cold crucible induction skull melting of titanium aluminum alloys. 837-844B
Deformation and fracture of a particle-reinforced aluminum alloy composite. II. Modeling. 937-950A
Equilibria involving the reciprocal spinel solid solution ($Mg_2Fe_{1-x}Al_xCr_{1-x}O_4$): modeling and experiment. 1247-1259B
Unsteady Marangoni flow in a molten pool when welding dissimilar metals. 1387-1403B
Residual strains in HY100 polycrystals: comparisons of experiments and simulations. 1543-1555A
Strain-localization in sheet metal containing a geometric defect. 1883-1886A
Modeling of dissolution, growth, and coarsening of aluminum nitride in low-carbon steels. 1907-1916A
Effects of processing variables on the microsegregation of directionally cast samples. 3137-3148A
- Acid leaching**
Characterization of scales obtained during continuous nickel laterite pilot-plant leaching. 1175-1186B
- Activated sintering**
Synthesis of $MoSi_2$ - $TiSi_2$ pseudobinary alloys by reactive sintering. 747-753A
- Adhesion, Coating effects**
Effects of sulfur on the fatigue and fracture resistance of interfaces between γ -Ni(Cr) and α - Al_2O_3 . 1977-1983A
- Adhesion, Composition effects**
Microstructure and formability of ZnNi alloy electrodeposited sheet steel. 475-485A
- Aerospace engines, Mechanical properties**
Role of foreign-object damage on thresholds for high-cycle fatigue in Ti-6Al-4V. 1571-1583A
- Agglomeration, Processing effects**
Sintering behavior of nanocrystalline γ -Ni-Fe powders. 503-510A
- Aging (artificial)**
Part II. Metallurgical factors governing the H-assisted intergranular cracking of peak-aged Ti-3Al-8V-6Cr-4Mo-4Zr (Beta-C). 81-92A
Differential scanning calorimetry and electron diffraction investigation on low-temperature aging in Al-Zn-Mg alloys. 339-348A
Influence of aging on transformation characteristics in shape memory CuZnAl alloys. 349-354A
Effect of mean stress (stress ratio) and aging on fatigue-crack growth in a metastable beta titanium alloy, Ti-10V-2Fe-3Al. 703-714A
Displacive transformations in Au-18 wt.% Cu-6 wt.% Al. 1917-1923A
Influence of thermal aging on the reactivity of duplex stainless steel surfaces. 2015-2024A
Microstructure and mechanical behavior of spray-deposited Al-Cu-Mg-(Ag-Mn) alloys. 2287-2298A
Discussion of "Surface relief and the displacive transformation to the lamellar microstructure in TiAl" and "Nanometer-scale, fully lamellar microstructure in an aged TiAl-based alloy". 2377-2379A
Author's reply to: Discussion of "Surface relief and the displacive transformation to the lamellar microstructure in TiAl" and "Nanometer-scale, fully lamellar microstructure in an aged TiAl-based alloy". 2379-2383A
Catalyzed precipitation in Al-Cu-Si. 2697-2711A
Spontaneous deformation during aging under stress in a copper-beryllium alloy. 2765-2771A
- Aging (artificial), Alloying effects**
Crystallographic details of precipitates in Fe-22Cr-21Ni-6Mo-(N) superaustenitic stainless steels aged at 900°C. 1713-1723A
Precipitation processes in Al-Cu-Mg alloys microalloyed with Si. 2721-2733A
- Aging (artificial), Composition effects**
Effects of Cu content and preaging on precipitation characteristics in aluminum alloy 6022. 361-371A
- Aging (artificial), Deformation effects**
A model for predicting the effect of deformation after solution treatment on the subsequent artificial aging behavior of AA7030 and AA7108 alloys. 2327-2338A
- Aircraft components, Mechanical properties**
The effect of processing and microstructure development on the slip and fracture behavior of the 2.1 wt.% Li AF/C-489 and 1.8 wt.% Li AF/C-458 Al-Li-C-X alloys. 1965-1976A
- Alkali metals, Reactions (chemical)**
Phase diagram study for the alkali metal-oxychloride system. 795-799B
- Allotropic transformation, Deformation effects**
Computer simulation of the initial rafting process of a nickel-base single-crystal superalloy. 585-597A
- Alloy plating**
Microstructure and formability of ZnNi alloy electrodeposited sheet steel. 475-485A
- Aluminates, Reduction (chemical)**
Investigation on reduction of $CoAl_2O_4$ by hydrogen gas using TGA. 540-542B
- Aluminides, Coating**
The influence of additions of Nb and Cr on the aluminizing behavior of TiAl alloy. 2391-2394A
- Aluminides, Coatings**
Effect of prealuminizing diffusion treatment on microstructural evolution of high-activity Pt-aluminide coatings. 2037-2047A
- Aluminides, Composite materials**
Chemically induced reduction: a viable process for synthesizing γ -TiAl based intermetallic matrix composite powders containing nanocrystalline TiC. 151-159B
Reaction steps in the combustion synthesis of NiAl/TiB₂ composites. 433-438B
Phase transitions in reactive formation of Ti_3Si_2 /TiAl in situ composites. 763-771A
Reactive infiltration processing and secondary compressive creep of NiAl and NiAl-W composites. 781-792A
An investigation of the effects of ductile-layer thickness on the fracture behavior of nickel aluminide microlaminates. 1385-1399A
High-temperature fracture and fatigue-crack growth behavior of an XD gamma-based titanium aluminide intermetallic alloy. 1413-1423A
Effect of particle size and volume fraction in hot extrusion reaction synthesis of SiC particle reinforced NiAl. 1663-1670A
Reaction synthesis, microstructure, and mechanical properties of in situ composite NiAl-Al₂O₃-TiC. 1692-1695A
Design and fabrication of W-Mo-Ti-TiAl-Al system functionally graded material. 2369-2376A
Near-net-shape forming of Al-Al₂Ni functionally graded material over eutectic melting temperature. 2627-2636A
- Aluminides, Crystal growth**
Effects of boron doping on the grain-growth kinetics and mechanical properties of γ/γ' nickel-aluminum alloys. 3179-3186A
- Aluminides, Diffusion**
An interdiffusion study of a NiAl alloy using single-phase diffusion couples. 1519-1524A
- Aluminides, Electrochemistry**
Prediction of properties of intermetallics using a chemical bonding model. 603-607B
- Aluminides, Mechanical properties**
The fracture resistance of a binary TiAl alloy. 71-80A
Mechanical behavior of a fine-grained duplex γ -TiAl alloy. 1007-1016A
Creep properties of $Ni_3(AlTiTa)$ γ phase single crystals. 1733-1740A
The effect of impact damage on the room-temperature fatigue behavior of γ -TiAl. 1741-1752A
A comparison study of microstructure and mechanical properties of Ti-24Al-14Nb-3V-0.5Mo with and without Si. 2205-2217A
Creep deformation of TiAl-Si alloys with aligned γ/α_2 lamellar microstructures. 2463-2473A
Dynamic fracture toughness of a Ti-45Al-1.6Mn alloy at high temperature. 3053-3061A
- Aluminides, Microstructure**
Recovery and ordering in cold-rolled boron-doped $Ni_{72}Al_{28}$. 2127-2134A
Evolution of texture in the $\beta(B2)$ phase of a two phase titanium aluminide intermetallic alloy Ti-24Al-11Nb. 2339-2350A
Discussion of "Surface relief and the displacive transformation to the lamellar microstructure in TiAl" and "Nanometer-scale, fully lamellar microstructure in an aged TiAl-based alloy". 2377-2379A
Author's reply to: Discussion of "Surface relief and the displacive transformation to the lamellar microstructure in TiAl" and "Nanometer-scale, fully lamellar microstructure in an aged TiAl-based alloy". 2379-2383A
Interaction of deformation twin and 120°-rotational order fault domain boundary in the lamellar structure of two-phase TiAl-based alloys. 2823-2834A
- Aluminides, Oxidation**
Formation of pegs during high-temperature oxidation of Fe_3Al containing yttrium. 1685-1687A
Diffusion of oxygen in the Al_2O_3 oxidation product of TiAl₃. 3023-3028A
- Aluminides, Powder technology**
Microstructural evolution in wire-drawn Ti-22Al-26Nb powder. 2931-2941A
- Aluminides, Rolling**
Deformation behavior of a $Ni_3Al(B,Zr)$ alloy during cold rolling. I. Changes in order and structure. 3001-3010A
Deformation behavior of a $Ni_3Al(B,Zr)$ alloy during cold rolling. II. Microstructural and textural changes. 3011-3021A
- Aluminizing**
Effect of prealuminizing diffusion treatment on microstructural evolution of high-activity Pt-aluminide coatings. 2037-2047A
- Aluminizing, Alloying effects**
The influence of additions of Nb and Cr on the aluminizing behavior of TiAl alloy. 2391-2394A
- Aluminothermic reactions**
Contactless electrochemical reduction of titanium (II) chloride by aluminum. 713-721B

- Aluminum, Alloying additive**
Effects of aluminum, silicon, and boron on the dissolution rate of nitrogen into molten iron. 899-904B
- Aluminum, Alloying elements**
Design of quaternary Ir-Nb-Ni-Al refractory superalloys. 173-178A
The effect of aluminum content on the corrosion behavior of Fe-Al alloys in reducing environments at 700°C. 1805-1817A
The role of solute in grain refinement of magnesium. 2895-2906A
- Aluminum, Binary systems**
Evaporation behavior of aluminum during the cold crucible induction skull melting of titanium aluminum alloys. 837-844B
- Aluminum, Casting**
Finding boundary conditions: a coupling strategy for the modeling of metal casting processes. I. Experimental study and correlation development. 75-86B
Finding boundary conditions: a coupling strategy for the modeling of metal casting processes. II. Numerical study and analysis. 87-96B
Numerical studies of the motion of spheroidal particles flowing with liquid metals through an electric sensing zone. 855-866B
Erratum: "Numerical studies of the motion of spheroidal particles flowing with liquid metals through an electric sensing zone". 1143B
- Aluminum, Composite materials**
Simulation of metal-matrix composite isothermal infiltration processing. 225-234B
Particulate penetration into solid droplets. 387-396A
Further discussion of "Particle engulfment and pushing by solidifying interfaces. II. Microgravity experiments and theoretical analysis". 1695-1700A
Authors' reply to: Further discussion of "Particle engulfment and pushing by solidifying interfaces. II. Microgravity experiments and theoretical analysis". 1700-1704A
A dynamic model for the interaction between a solid particle and an advancing solid/liquid interface. 2559-2568A
Near-net-shape forming of Al-Al₃Ni functionally graded material over eutectic melting temperature. 2627-2636A
- Aluminum, Crystal growth**
Measurements, simulations, and analyses of instantaneous heat fluxes from solidifying steels to the surfaces of twin roll casters and of aluminum to plasma-coated metal substrates. 1031-1047B
- Aluminum, Extraction**
Formation of aluminum titanate-mullite composite from bauxite red mud. 551-553B
Solutions of iron oxides in molten cryolite. 609-613B
Melt penetration and chemical reactions in 16 industrial aluminum carbon cathodes. 1213-1224B
On the mechanism of the anode effect in aluminum electrolysis. 1225-1230B
A new approach to numerical simulation of melt flows and interface instability in Hall-Héroult cells. 1541-1550B
Some generalities in the analyses of equilibria in ionic solutions. 2105-2118A
- Aluminum, Extrusion**
Flow behavior of the billet surface layer in porthole die extrusion of aluminum. 1635-1643A
- Aluminum, Microstructure**
Through-thickness texture gradients in cold-rolled aluminum. 1653-1662A
- Aluminum, Physical properties**
Numerical simulation of the flow and the solid transport when tilting a holding furnace. 207-214B
- Aluminum, Powder technology**
Preparation and mechanical properties of highly densified nanocrystalline Al. 1017-1024A
- Aluminum, Refining**
A mathematical model of aluminum depth filtration with ceramic foam filters. I. Validation for short-term filtration. 491-502B
A mathematical model of aluminum depth filtration with ceramic foam filters. II. Application to long-term filtration. 503-513B
- Aluminum, Ternary systems**
Examination of solidification pathways and the liquidus surface in the Nb-Ti-Al system. 1305-1321B
- Aluminum, Welding**
Unsteady Marangoni flow in a molten pool when welding dissimilar metals. 1387-1403B
- Aluminum base alloys, Atomic properties**
The atomic-structure changes in Al-16% Si alloy above the liquidus. 2163-2168A
- Aluminum base alloys, Brazing**
Development of a low-melting-point filler metal for brazing aluminum alloys. 2239-2245A
- Aluminum base alloys, Casting**
Finding boundary conditions: a coupling strategy for the modeling of metal casting processes. I. Experimental study and correlation development. 75-86B
Finding boundary conditions: a coupling strategy for the modeling of metal casting processes. II. Numerical study and analysis. 87-96B
Prevention of macrodefects in squeeze casting of an Al-7 wt.% Si alloy. 297-305B
Two-phase modeling of mushy zone parameters associated with hot tearing. 1461-1472A
Determination of thermophysical properties and boundary conditions of direct chill-cast aluminum alloys using inverse methods. 1627-1634A
Correlation between unsteady-state solidification conditions, dendrite spacings, and mechanical properties of Al-Cu alloys. 3167-3178A
- Aluminum base alloys, Coatings**
Dynamic reactive wetting and its role in hot dip coating of steel sheet with an Al-Zn-Si alloy. 1069-1079B
- Aluminum base alloys, Composite materials**
Thermal activation of fatigue damage. 63-69A
On the infiltration behavior of Al, Al-Li, and Mg melts through SiC₂ bed. 319-325A
The effect of matrix microstructure on the tensile and fatigue behavior of SiC particle-reinforced 2080 Al matrix composites. 531-540A
Optimum parameters for wetting silicon carbide by aluminum alloys. 565-573A
Effect of volume fraction of SiC₂ reinforcement on the processing maps for 2124 Al matrix composites. 629-639A
Effect of albite particles on the coefficient of thermal expansion behavior of the Al6061 alloy composites. 773-780A
Deformation and fracture of a particle-reinforced aluminum alloy composite. I. Experiments. 921-936A
Deformation and fracture of a particle-reinforced aluminum alloy composite. II. Modeling. 937-950A
The interactive role of inclusions and SiC reinforcement on the high-cycle fatigue resistance of particle reinforced metal matrix composites. 951-957A
The quasi-static and cyclic fatigue fracture behavior of 2014 aluminum alloy metal-matrix composites. 959-974A
Nucleation on ceramic particles in cast metal-matrix composites. 1295-1304A
Plastic flow behavior during the forging of a 6061 Al/10 vol% Al₂O₃(p) composite. 1310-1313A
Microstructure and properties of in situ Al/TiB₂ composite fabricated by in-melt reaction method. 1959-1964A
Porosity nucleation in metal-matrix composites. 2069-2074A
Effect of particle-size distribution on the properties of high-volume-fraction SiC₂-Al-based composites. 2351-2359A
Modification of the interface in SiC/Al composites. 2361-2368A
Study of 6061-Al₂O₃ composites produced by reciprocating extrusion. 2587-2596A
- Aluminum base alloys, Crystal growth**
Solidification characteristics of the Al-8.3Fe-0.8V-0.9Si alloy. 1599-1610A
- Aluminum base alloys, Directional solidification**
A model of the interfacial heat-transfer coefficient during unidirectional solidification of an aluminum alloy. 285-295B
Effect of increased growth velocity on the growth temperature of the Al-Al₂Cu eutectic. 327-328A
- Aluminum base alloys, Electrochemistry**
Contactless electrochemical reduction of titanium (II) chloride by aluminum. 713-721B
- Aluminum base alloys, Heat treatment**
A model for predicting the effect of deformation after solution treatment on the subsequent artificial aging behavior of AA7030 and AA7108 alloys. 2327-2338A
- Aluminum base alloys, Mechanical properties**
Effect of intermediate annealing on texture evolution and plastic anisotropy in an Al-Mg autobody alloy. 99-107A
Stress-strain response of a cast 319-T6 aluminum under thermomechanical loading. 139-151A
Effects of strain rate and anisotropy on the tensile deformation properties of extruded AlZnMg alloys. 669-678A
Simulation of shear plugging through thin plates using the GRIM Eulerian hydrocode. 853-860A
Interactions between mechanical and environmental variables for short fatigue cracks in a 2024-T3 aluminum alloy in 0.5M NaCl solutions. 1025-1034A
Ultrasonic attenuation peak in steel and aluminum alloy during rotating bending fatigue. 1121-1128A
Heat generation during the fatigue of a cellular Al alloy. 1129-1136A
Effect of testing frequency on the corrosion fatigue of a squeeze-cast aluminum alloy. 1137-1145A
Near-threshold fatigue crack growth behavior of 2195 aluminum-lithium alloy—prediction of crack propagation direction and influence of stress ratio. 1531-1541A
Effect of strain rate on damage evolution in a cast Al-Si-Mg base alloy. 1725-1731A
The effect of processing and microstructure development on the slip and fracture behavior of the 2.1 wt.% Li AF/C-489 and 1.8 wt.% Li AF/C-458 Al-Li-C-X alloys. 1965-1976A
Effect of long-term room-temperature storage on the structure and properties of glassy melt-spun Mg-Al-Ca alloys. 2155-2162A
High-temperature creep of an Al-8.5Fe-1.3V-1.7Si alloy processed by rapid solidification. 2229-2237A
Microstructure and mechanical behavior of spray-deposited Al-Cu-Mg(-Ag-Mn) alloys. 2287-2298A
Microstructural effects on fracture toughness in AA7010 plate. 2503-2515A
Enhanced densification of cavitated dispersion-strengthened aluminum by thermal cycling. 2647-2657A
Creep rupture mechanisms in annealed and overheated 7075 Al under multiaxial stress states. 2807-2821A
- Aluminum base alloys, Metal working**
Equal-channel angular pressing of commercial aluminum alloys: grain refinement, thermal stability and tensile properties. 691-701A
- Aluminum base alloys, Microstructure**
Microstructural characterization of a rapidly solidified ultrahigh strength Al_{0.5}Cr_{0.5}Co_{1.5}Ce₁ alloy. 607-614A
Effects of the intensity and frequency of electromagnet vibrations on the microstructural refinement of hypoeutectic Al-Si alloys. 755-762A
Evolution of texture and grain misorientation in an Al-Mg alloy exhibiting low-temperature superplasticity. 2169-2180A

- Aluminum base alloys, Oxidation**
Diffusion of oxygen in the Al_2O_3 oxidation product of $TiAl_3$. 3023-3028A
- Aluminum base alloys, Phase transformations**
Differential scanning calorimetry and electron diffraction investigation on low-temperature aging in Al-Zn-Mg alloys. 339-348A
Effects of Cu content and preaging on precipitation characteristics in aluminum alloy 6022. 361-371A
Nature of precipitates and constituent particles present in a ternary Al-Ge-Si alloy. 2093-2097A
Catalyzed precipitation in Al-Cu-Si. 2697-2711A
An experimental investigation on the kinetics of solute driven remelting. 2713-2720A
Precipitation processes in Al-Cu-Mg alloys microalloyed with Si. 2721-2733A
- Aluminum base alloys, Physical properties**
Experimental difficulties associated with permeability measurements in aluminum alloys. 3149-3153A
- Aluminum base alloys, Powder technology**
Processing and microstructural characterization of Al-Cu alloys produced from rapidly solidified powders. 249-260A
An integrated model for dendritic and planar interface growth and morphological transition in rapid solidification. 735-746A
- Aluminum base alloys, Quality control**
Numerical calculation of the electromagnetic expulsive force upon nonmetallic inclusions in an aluminum melt. I. Spherical particles. 1527-1533B
Numerical calculation of the electromagnetic expulsive force upon nonmetallic inclusions in an aluminum melt. II. Cylindrical particles. 1535-1540B
- Aluminum base alloys, Sorption**
The identification of hydrogen trapping states in an Al-Li-Cu-Zr alloy using thermal desorption spectroscopy. 179-193A
- Aluminum base alloys, Welding**
Dispersoid-free zones in the heat-affected zone of aluminum alloy welds. 1453-1459A
Friction-stir welding effects on microstructure and fatigue of aluminum alloy 7050-T7451. 2181-2192A
Improved microstructure and properties of 6061 aluminum alloy weldments using a double-sided arc welding process. 2537-2543A
Weld metal ductility in aluminum tail welded blanks. 2755-2763A
- Aluminum compounds, Crystal growth**
Effect of increased growth velocity on the growth temperature of the Al- Al_2Cu eutectic. 327-328A
- Aluminum compounds, Phase transformations**
Influence of aging on transformation characteristics in shape memory $CuZnAl$ alloys. 349-354A
- Aluminum killed steels, Heat treatment**
Modeling of dissolution, growth, and coarsening of aluminum nitride in low-carbon steels. 1907-1916A
- Aluminum killed steels, Steel making**
Behavior of nonmetallic inclusions in front of the solid-liquid interface in low-carbon steels. 1013-1021B
- Aluminum oxide, Coatings**
Effects of sulfur on the fatigue and fracture resistance of interfaces between $\gamma-Ni(Cr)$ and $\alpha-Al_2O_3$. 1977-1983A
- Aluminum oxide, Composite materials**
Thermal activation of fatigue damage. 63-69A
Simulation of metal-matrix composite isothermal infiltration processing. 225-234B
Particulate penetration into solid droplets. 387-396A
The quasi-static and cyclic fatigue fracture behavior of 2014 aluminum alloy metal-matrix composites. 959-974A
Plastic flow behavior during the forging of a 6061 Al/10 vol% $Al_2O_3(p)$ composite. 1310-1313A
Reaction synthesis, microstructure, and mechanical properties of in situ composite $NiAl-Al_2O_3-TiC$. 1692-1695A
Microstructure and properties of in situ Al/ TiB_2 composite fabricated by in-melt reaction method. 1959-1964A
Porosity nucleation in metal-matrix composites. 2069-2074A
Study of 6061- Al_2O_3 composites produced by reciprocating extrusion. 2587-2596A
- Aluminum oxide, Powder technology**
Improved densification of carbonyl iron compacts by the addition of fine alumina powders. 1645-1652A
- Aluminum oxide, Reactions (chemical)**
Phase diagram for the system $CaO-Al_2O_3-ZrO_2$. 25-33B
Kinetics of Al_2O_3 dissolution in $CaO-MgO-SiO_2-Al_2O_3$ slags: in situ observations and analysis. 406-410B
On the mechanism of the anode effect in aluminum electrolysis. 1225-1230B
- Aluminum oxide, Solubility**
Solutions of iron oxides in molten cryolite. 609-613B
- Amorphization**
Ideal and cooperative bond-lattice representations of excitations in glass-forming liquids: excitation profiles, fragilities, and phase transitions. 587-596B
- Amorphous structure, Processing effects**
Microstructural characterization of a rapidly solidified ultrahigh strength $Al_{94.5}Cr_{3.5}Co_{1.5}Ce_1$ alloy. 607-614A
- Annealing**
Effect of intermediate annealing on texture evolution and plastic anisotropy in an Al-Mg autobody alloy. 99-107A
Grain boundary faceting and abnormal grain growth in nickel. 985-994A
Influence of annealing conditions on the galvanizability and galvannealing properties of TiNb interstitial-free steels, strengthened with phosphorus and manganese. 1225-1232A
The role of the divorced eutectoid transformation in the spheroidization of 52100 steel. 2431-2438A
Creep rupture mechanisms in annealed and overheated 7075 Al under multiaxial stress states. 2807-2821A
- Arc spraying**
Effect of fiber volume fraction on the fracture behavior of Nb-1 wt.% Zr/218W composites at elevated temperatures. 873-887A
- Arc welding**
Thermal analysis of the arc welding process. I. General solutions. 1353-1370B
Improved microstructure and properties of 6061 aluminum alloy weldments using a double-sided arc welding process. 2537-2543A
- Argon, Solubility**
Argon solubility in molten iron. 216-218B
Argon solubility in liquid steel. 913-919B
- Armor, Mechanical properties**
Simulation of shear plugging through thin plates using the GRIM Eulerian hydrocode. 853-860A
- Ashes, Reactions (chemical)**
Phase diagram study for the alkali metal-oxychloride system. 795-799B
Influence of ash on mass transfer and interfacial reaction between natural graphite and liquid iron. 1099-1104B
- Atomic structure, Temperature effects**
The atomic-structure changes in Al-16% Si alloy above the liquidus. 2163-2168A
- Atomizing**
Processing and microstructural characterization of Al-Cu alloys produced from rapidly solidified powders. 249-260A
Monosize droplet deposition as a means to investigate droplet behavior during spray deposition. 1333-1344B
Solute segregation behavior in spray-atomized Pd-Rh-V(Co) powders. 1843-1855A
Factors influencing solute segregation of spray-atomized palladium alloy powders. 2681-2686A
Modeling of spray-formed materials: geometrical considerations. 2917-2929A
- Austempering**
Microstructural development and austempering kinetics of ductile iron during thermomechanical processing. 2575-2585A
- Austenite**
Influence of microstructure on the flow behavior of duplex stainless steels at high temperatures. 1353-1364A
- Austenite, Mechanical properties**
Load sharing between austenite and ferrite in a duplex stainless steel during cyclic loading. 1557-1570A
- Austenitic stainless steels, Casting**
Mechanisms of initial melt/substrate heat transfer pertinent to strip casting. 1023-1030B
- Austenitic stainless steels, Coating**
Surface amorphous and crystalline microstructure by alloying zirconium using Nd:YAG pulsed laser. 3123-3127A
- Austenitic stainless steels, Composite materials**
The influence of reinforcement particle size distribution on the mechanical behavior of a stainless steel/TiN composite. 309-318A
- Austenitic stainless steels, Corrosion**
Role of Mo and W during sensitization of superaustenitic stainless steel—crystallography and composition of precipitates. 1893-1905A
- Austenitic stainless steels, Crystal growth**
Thermodynamic-kinetic simulation of constrained dendrite growth in steels. 365-379B
- Austenitic stainless steels, Heat treatment**
Study of microstructure of low-temperature plasma-nitrided AISI 304 stainless steel. 1193-1199A
- Austenitic stainless steels, Mechanical properties**
Mechanical properties of austenitic stainless steel single crystals: influence of nitrogen and hydrogen content. 153-161A
A model for creep-fatigue interaction in terms of crack-tip stress relaxation. 1761-1775A
Experimental studies on tribological properties of pseudoelastic TiNi alloy with comparison to stainless steel 304. 2773-2783A
- Austenitic stainless steels, Microstructure**
The effect of cooling rate on the microstructures formed during solidification of ferritic steel. 3155-3166A
- Austenitic stainless steels, Welding**
Creep deformation and fracture behavior of types 316 and 316L(N) stainless steels and their weld metals. 1175-1185A
Relation between microstructure, composition, and hot cracking in Ti-stabilized austenitic stainless steel weldments. 3109-3122A
- Austenitizing, Diffusion effects**
On the mobility of the austenite-ferrite interface in Fe-Co and Fe-Cu. 379-385A
- Automotive bodies, Mechanical properties**
Effect of intermediate annealing on texture evolution and plastic anisotropy in an Al-Mg autobody alloy. 99-107A
Dynamic materials testing, texture, and yield-surface calculation of an automotive sheet steel. 2439-2448A
- Automotive components, Heat treatment**
Dynamic bake hardening of interstitial-free steels. 1375-1384A
- Backward extrusion**
Thin-wall back extrusion of partially remelted semi-solid Sn-Pb. 57-62A
Near-net-shape forming of Al- Al_2Ni functionally graded material over eutectic melting temperature. 2627-2636A
- Bake hardenable steels, Heat treatment**
Dynamic bake hardening of interstitial-free steels. 1375-1384A
- Baking**
Dynamic bake hardening of interstitial-free steels. 1375-1384A

Ball milling

- Synthesis of nanostructured WC-12%Co coating using mechanical milling and high velocity oxygen fuel thermal spraying. 541-553A
- Synthesis of nanostructured Cr_3C_2 -25(Ni20Cr) coatings. Neutron diffraction and phase evolution of the mechanically alloyed intermetallic compound $\xi\text{-FeZn}_{13}$. 555-564A
- Thermal transformations in mechanically alloyed Fe-Zn-Si materials. 2739-2745A
- 2747-2754A

Ballistics

- Simulation of shear plugging through thin plates using the GRIM Eulerian hydrocode. 853-860A

Barium compounds, Electrochemistry

- Thermodynamic and nonstoichiometric behavior of promising Hi-Tc cuprate systems via electromotive force measurements: a short review. 661-666B

Barkhausen effect, Microstructural effects

- Insight into the microstructural characterization of ferritic steel using micromagnetic parameters. 1053-1065A

Basic converters

- Equilibria involving the reciprocal spinel solid solution $(\text{Mg}_x\text{Fe}_{1-x})(\text{Al}_y\text{Cr}_{1-y})_2\text{O}_4$: modeling and experiment. 1247-1259B
- Spinel-cordierite equilibria and activities in the system $\text{MgO-Al}_2\text{O}_3\text{-Cr}_2\text{O}_3$ at 1473K. 1323-1332B

Bauschinger effect

- Analysis and prevention of yield strength drop during spiral piping of two high-strength API-X70 steels. 2669-2674A

Bauschinger effect, Composition effects

- Influence of elastic inclusion morphology and matrix hardening behavior on Bauschinger effect in metal matrix composites. 2943-2948A

Bauxite, Reduction (chemical)

- Formation of aluminum titanate-mullite composite from bauxite red mud. 551-553B

Bayer process

- Formation of aluminum titanate-mullite composite from bauxite red mud. 551-553B

BCC metals, Microstructure

- Yield vertices for $\{123\}<111>$ multiple slip. 2449-2456A

Bearing steels, Phase transformations

- The role of the divorced eutectoid transformation in the spheroidization of 52100 steel. 2431-2438A

Bearing strength, Deformation effects

- Synchrotron x-ray study of bulk lattice strains in externally loaded Cu-Mo composites. 2949-2962A

Bend strength, Composition effects

- Effect of particle-size distribution on the properties of high-volume-fraction $\text{SiC}_p\text{-Al}$ -based composites. 2351-2359A

Bending fatigue

- Ultrasonic attenuation peak in steel and aluminum alloy during rotating bending fatigue. 1121-1128A

Beryllium base alloys, Microstructure

- Microstructural characterization of novel in-situ Al-Be composites. 2963-2971A

Billet casting

- Melt flow control in a multistrand tundish using a turbulence inhibitor. 1505-1515B

Billets, Extrusion

- Flow behavior of the billet surface layer in porthole die extrusion of aluminum. 1635-1643A

Binary systems, Phase transformations

- A numerical and experimental study of the rate of transformation in three directionally grown peritectic systems. 29-34A
- Enthalpy of mixing of liquid Ni-Zr and Cu-Ni-Zr alloys. 277-284B
- Driving force for $\gamma \rightarrow \epsilon$ martensitic transformation and stacking fault energy of γ in Fe-Mn binary system. 355-360A
- On the mobility of the austenite-ferrite interface in Fe-Co and Fe-Cu. 379-385A
- Evaporation behavior of aluminum during the cold crucible induction skull melting of titanium aluminum alloys. 837-844B
- A model of convection-induced oscillatory structure formation in peritectic alloys. 1233-1246A
- A model for nonclassical nucleation of solid-solid structural phase transformations. 1321-1331A
- Coarsening of intermetallic or compound precipitates in binary systems. 3195-3197A

Binary systems, Phases (state of matter)

- Eutectic interface configurations during melting. 1261-1269A
- On the Gibbs-Thomson effect in concentrated binary systems. Measurement of the activity of boron in liquid copper using a four-phase equilibrium technique. 2659-2661A
- 2674-2678A

Binder removal

- Length change and deformation of powder injection-molded compacts during solvent debinding. 1473-1478A
- Simulation of polymer removal from a powder injection molding compact by thermal debinding. 2597-2606A

Bismuth, Binary systems

- A model of convection-induced oscillatory structure formation in peritectic alloys. 1233-1246A

Bismuth, Reactions (chemical)

- Dissolution of lead and bismuth in white metal ($\text{CuS}_{0.5}$) at matte-smelting temperatures. 543-546B

Bismuth base alloys, Casting

- A comparative study of the microstructures observed in statically cast and continuously cast Bi-In-Sn ternary eutectic alloy. 239-248A

Bismuth compounds, Electrochemistry

- Thermodynamic and nonstoichiometric behavior of promising Hi-Tc cuprate systems via electromotive force measurements: a short review. 661-666B

Blast furnace practice

- Developments in blast furnace process control at Port Kembla based on process fundamentals. 993-1003B

Bonding

- Transient liquid-phase bonding in two-phase ternary systems. 1187-1192A

Bonding strength

- The role of plasticity in bimaterial fracture with ductile interlayers. 863-872A

Boron, Alloying additive

- Effects of aluminum, silicon, and boron on the dissolution rate of nitrogen into molten iron. 899-904B
- Atom probe field ion microscopy investigation of boron containing martensitic 9% chromium steel. 975-984A

Boron, Binary systems

- Measurement of the activity of boron in liquid copper using a four-phase equilibrium technique. 2674-2678A

Boron, Dopants

- Dilatometry study of the sintering behavior of boron-alloyed Fe-1.5% Mo powder. 1497-1506A
- Recovery and ordering in cold-rolled boron-doped $\text{Ni}_{70}\text{Al}_{24}$. Effects of boron doping on the grain-growth kinetics and mechanical properties of γ/γ' nickel-aluminum alloys. 2127-2134A
- 3179-3186A

Boron, Impurities

- Microstructural characterization and analysis of inclusions in C-Mn steel and weld metals. 615-628A

Boundary element method

- Equilibrium shape of a molten silicon drop in an electromagnetic levitator in microgravity environment. 327-329B

Brazing alloys, Materials selection

- Development of a low-melting-point filler metal for brazing aluminum alloys. 2239-2245A

Brittle fracture, Coating effects

- Growth of a Au-Ni-Sn intermetallic compound on the solder-substrate interface after aging. 798-800A

Brittle fracture, Microstructural effects

- The mechanism of brittle fracture in a microalloyed steel. I. Inclusion-induced cleavage. 641-652A
- The mechanism of brittle fracture in a microalloyed steel. II. Mechanistic modeling. 653-667A

Brittle fracture, Processing effects

- A new criterion for internal crack formation in continuously cast steels. 779-794B

Bronzes, Casting

- Effects of processing variables on the microsegregation of directionally cast samples. 3137-3148A

Bronzes, Composite materials

- Tribological properties of centrifugally cast copper alloy-graphite particle composite. 1283-1293A

Bronzes, Heat treatment

- Spontaneous deformation during aging under stress in a copper-beryllium alloy. 2765-2771A

Bubbles

- Argon solubility in molten iron. 216-218B
- X-ray fluoroscopy observations of bubble formation and separation at a metal-slag interface. 537-540B

Cadmium, Binary systems

- A numerical and experimental study of the rate of transformation in three directionally grown peritectic systems. 29-34A
- A model of convection-induced oscillatory structure formation in peritectic alloys. 1233-1246A

Calcium, Alloying additive

- The role of solute in grain refinement of magnesium. 2895-2906A

Calcium, Reactions (chemical)

- Activity measurement of the constituents in liquid Cu-Mg and Cu-Ca alloys with mass spectrometry. 927-935B
- Activity of calcium in dilute liquid Si-Ca alloy. 1267-1272B

Calcium compounds, Transport properties

- The ionic properties of CaSiO_3 melt. 1241-1245B

Calendering

- Modeling of microstructure and residual stress in cast iron calender rolls. 1201-1211A

Carbides, Alloying effects

- Crystallographic details of precipitates in Fe-22Cr-21Ni-6Mo-(N) superaustenitic stainless steels aged at 900°C. 1713-1723A

Carbides, Crystal growth

- Modeling of dissolution, growth, and coarsening of aluminum nitride in low-carbon steels. 1907-1916A
- Quantitative approach to coagulation, coalescence, and polygonization of carbides in the NCWV/D3 tool steel. 2661-2665A

Carbon, Alloying elements

- Strength and formability of ultra-low-carbon Ti-IF steels. 1305-1307A

Carbon, Diffusion

- A Scheil-Gulliver model with back-diffusion applied to the microsegregation of chromium in Fe-Cr-C alloys. 1682-1684A

Carbon, Oxidation

- Kinetics of oxidation of carbonaceous materials by CO_2 and H_2O between 1300° and 1500°C. 43-54B

Carbon, Reactions (chemical)

- Thermodynamics of surfaces and adsorption in the Fe-C-S-O system. 267-276B

- Melt penetration and chemical reactions in 16 industrial aluminum carbon cathodes. 1213-1224B
 A model for the role of carbon on carbochlorination of TiO_2 . 1439-1446B
 A Monte Carlo simulation study of dissolution of graphite in iron-carbon melts. 1517-1525B
- Carbon, Solubility**
 Dissolution rates of coals and graphite in Fe-C-S melts in direct ironmaking: dependence of carbon dissolution rate on carbon structure. 215-216B
- Carbon manganese steels, Mechanical properties**
 Influence of alloying elements on the strain rate and temperature dependence of the flow stress of steels. 825-830A
- Carbon manganese steels, Rolling**
 Mathematical modeling of the hot strip rolling of microalloyed Nb, multiply alloyed Cr-Mo, and plain C-Mn steels. 511-530A
- Carbon manganese steels, Welding**
 Microstructural characterization and analysis of inclusions in C-Mn steel and weld metals. 615-628A
- Carbon monoxide, Reactions (chemical)**
 Kinetics of manganese ore reduction by carbon monoxide. 477-490B
- Carbon steels, Cladding**
 Microstructural evolution during laser cladding of M2 high-speed steel. 2615-2625A
- Carbon steels, Heat treatment**
 Microstructural analysis of vanadium carbide/steel surface-alloyed materials fabricated by high-energy electron-beam irradiation. 2849-2855A
- Carbon steels, Mechanical properties**
 Dynamic materials testing, texture, and yield-surface calculation of an automotive sheet steel. 2439-2448A
- Carbon steels, Phase transformations**
 Kinetics of peritectic reaction and transformation in Fe-C alloys. 981-991B
- Carbon steels, Steel making**
 Nitrogen alloying of carbon and stainless steels by gas injection. 905-912B
- Carbonitrides, Composite materials**
 Development of a thermodynamic database for cemented carbides for design and processing simulations. 615-619B
- Carbonitriding**
 Microstructural and compositional evolution of compound layers during gaseous nitrocarburizing. 195-211A
 Erratum: Microstructural and compositional evolution of compound layers during gaseous nitrocarburizing. 801A
- Carbonyls, Powder technology**
 Preparation of high porosity metal foams. 1345-1352B
- Cast iron, Casting**
 Modeling of microstructure and residual stress in cast iron calender rolls. 1201-1211A
- Cast iron, Mechanical properties**
 Effect of nodularity on resonant vibration fracture behavior in upper bainitic and ferritic cast irons. 2193-2203A
- Cast iron, Phases (state of matter)**
 Phase analysis of two steel work rolls using Mössbauer spectroscopy. 793-798A
- Cast iron, Reactions (chemical)**
 A Monte Carlo simulation study of dissolution of graphite in iron-carbon melts. 1517-1525B
- Casting**
 Microstructural characterization of novel in-situ Al-Be composites. 2963-2971A
- Casting alloys, Crystal growth**
 Solidification characteristics of the Al-8.3Fe-0.8V-0.9Si alloy. 1599-1610A
- Casting alloys, Mechanical properties**
 Stress-strain response of a cast 319-T6 aluminum under thermomechanical loading. 139-151A
- Casting defects**
 Prevention of macrodefects in squeeze casting of an Al-7 wt.% Si alloy. 297-305B
 A computational model for defect prediction in shape castings based on the interaction of free surface flow, heat transfer, and solidification phenomena. 515-527B
 Freckle formation and freckle criterion in superalloy castings. 801-811B
 Depth of oscillation marks forming in continuous casting of steel. 813-826B
 Development of a freckle predictor via Rayleigh number method for single-crystal nickel-base superalloy castings. 2545-2557A
- Casting defects, Processing effects**
 Aluminum volatilization and inclusion removal in the electron beam cold hearth melting of Ti alloys. 845-854B
- Casting machines, Thermal properties**
 Mechanisms of initial melt/substrate heat transfer pertinent to strip casting. 1023-1030B
- Castings, Crystal growth**
 Measurements, simulations, and analyses of instantaneous heat fluxes from solidifying steels to the surfaces of twin roll casters and of aluminum to plasma-coated metal substrates. 1031-1047B
- Castings, Microstructure**
 Monte Carlo sampling for microsegregation measurements in cast structures. 2569-2574A
 Effects of processing variables on the microsegregation of directionally cast samples. 3137-3148A
- Castings, Quality control**
 A computational model for defect prediction in shape castings based on the interaction of free surface flow, heat transfer, and solidification phenomena. 515-527B
- Catalysis**
 Effect of a catalyst on the kinetics of reduction of celestite (SrSO_4) by active charcoal. 35-41B
 Catalyzed precipitation in Al-Cu-Si. 2697-2711A
- Catalysts, Materials selection**
 Effect of a catalyst on the kinetics of reduction of celestite (SrSO_4) by active charcoal. 35-41B
- Cathodes, Reactions (chemical)**
 Melt penetration and chemical reactions in 16 industrial aluminum carbon cathodes. 1213-1224B
- Cavitation**
 On methane generation and decarburization in low-alloy Cr-Mo steels during hydrogen attack. 125-137A
 An analysis of the effect of cavity nucleation rate and cavity coalescence on the tensile behavior of superplastic materials. 1425-1434A
- Cellular structure**
 Heat generation during the fatigue of a cellular Al alloy. 1129-1136A
- Cellular structure, Coating effects**
 Microstructural evolution during laser cladding of M2 high-speed steel. 2615-2625A
- Cemented carbides, Coatings**
 Synthesis of nanostructured WC-12%Co coating using mechanical milling and high velocity oxygen fuel thermal spraying. 541-553A
 Synthesis of nanostructured Cr_3C_2 -25(Ni20Cr) coatings. 555-564A
- Cemented carbides, Crystal growth**
 Anisotropic grain growth based on the atomic adsorption model in WC-25% Co alloy. 1925-1935A
- Cemented carbides, Phases (state of matter)**
 Development of a thermodynamic database for cemented carbides for design and processing simulations. 615-619B
- Cementite, Crystal growth**
 Quantitative approach to coagulation, coalescence, and polygonization of carbides in the NCWV/D3 tool steel. 2661-2665A
- Cementite, Reactions (chemical)**
 Effect of temperature on cementite formation by reaction of iron ore with H_2 - CH_4 -Ar gas. 1139-1142B
- Centrifugal casting**
 Tribological properties of centrifugally cast copper alloy-graphite particle composite. 1283-1293A
 The atomic-structure changes in Al-16% Si alloy above the liquidus. 2163-2168A
- Centrifugal castings, Mechanical properties**
 Tribological properties of centrifugally cast copper alloy-graphite particle composite. 1283-1293A
- Chalcocopyrite, Solubility**
 Galvanic interaction between chalcocopyrite and manganese dioxide in sulfuric acid medium. 55-61B
- Chill castings, Crystal growth**
 Two-phase modeling of mushy zone parameters associated with hot tearing. 1461-1472A
- Chills, Physical properties**
 A model of the interfacial heat-transfer coefficient during unidirectional solidification of an aluminum alloy. 285-295B
- Chills, Thermal properties**
 Modeling of interdendritic strain and macrosegregation for dendritic solidification processes. I. Theory and experiments. 331-343B
 Modeling of interdendritic strain and macrosegregation for dendritic solidification processes. II. Computation of interdendritic strain and segregation fields in steel ingots. 345-355B
- Chlorination**
 The study of chlorination kinetics of copper (I) sulfide by calcium chloride in the presence of oxygen. 723-731B
 A model for the role of carbon on carbochlorination of TiO_2 . 1439-1446B
- Chromium, Alloying additive**
 Theoretical and experimental investigations of electron beam surface remelting and alloying. 1405-1417B
 The influence of additions of Nb and Cr on the aluminumizing behavior of TiAl alloy. 2391-2394A
- Chromium, Alloying elements**
 Alloy design of FeMnSiCrNi shape-memory alloys related to stacking-fault energy. 581-584A
- Chromium, Diffusion**
 A Scheil-Gulliver model with back-diffusion applied to the microsegregation of chromium in Fe-Cr-C alloys. 1682-1684A
- Chromium, Reactions (chemical)**
 The effects of alkaline earth metal ions and halogen ions on the chromium oxide activities in alkaline earth metal oxide-halide- Cr_2O_3 system fluxes. 469-475B
- Chromium, Ternary systems**
 Experimental investigation and thermodynamic modeling of the Cr-Ni-Si system. 1795-1803A
- Chromium molybdenum steels, Magnetic properties**
 Insight into the microstructural characterization of ferritic steel using micromagnetic parameters. 1053-1065A
- Chromium molybdenum steels, Mechanical properties**
 On methane generation and decarburization in low-alloy Cr-Mo steels during hydrogen attack. 125-137A
 Influence of alloying elements on the strain rate and temperature dependence of the flow stress of steels. 825-830A
- Chromium molybdenum steels, Rolling**

- Mathematical modeling of the hot strip rolling of microalloyed Nb, multiply alloyed Cr-Mo, and plain C-Mn steels. 511-530A
- Chromium molybdenum steels, Surface finishing**
Macroscopic and microscopic evolutions of a shot-peened layer during isothermal recovery. 213-224A
- Chromium molybdenum steels, Welding**
Three-dimensional Monte Carlo simulation of grain growth in the heat-affected zone of a 2.25Cr-1Mo steel weld. 529-536B
Relevance of high-temperature oxidation in life assessment and microstructural degradation of Cr-Mo steel weldments. 3101-3108A
- Chromium molybdenum vanadium steels, Mechanical properties**
A model for creep-fatigue interaction in terms of crack-tip stress relaxation. 1761-1775A
- Chromium steels, Diffusion**
A Scheil-Gulliver model with back-diffusion applied to the microsegregation of chromium in Fe-Cr-C alloys. 1682-1684A
- Chromium steels, Phase transformations**
The role of the divorced eutectoid transformation in the spheroidization of 52100 steel. 2431-2438A
- Cleavage, Microstructural effects**
The mechanism of brittle fracture in a microalloyed steel. I. Inclusion-induced cleavage. 641-652A
The mechanism of brittle fracture in a microalloyed steel. II. Mechanistic modeling. 653-667A
- Coagulation**
Quantitative approach to coagulation, coalescence, and polygonization of carbides in the NCWV/D3 tool steel. 2661-2665A
- Coal, Reactions (chemical)**
Dissolution rates of coals and graphite in Fe-C-S melts in direct ironmaking: influence of melt carbon and sulfur on carbon dissolution. 243-251B
Coal pyrolysis in a rotary kiln. I. Model of the pyrolysis of a single grain. 381-390B
Coal pyrolysis in a rotary kiln. II. Overall model of the furnace. Quantifying the heats of coal devolatilization. 391-402B
1125-1131B
- Cobalt, Binary systems**
On the mobility of the austenite-ferrite interface in Fe-Co and Fe-Cu. 379-385A
A model for nonclassical nucleation of solid-solid structural phase transformations. 1321-1331A
- Cobalt, Composite materials**
Development of a thermodynamic database for cemented carbides for design and processing simulations. 615-619B
Anisotropic grain growth based on the atomic adsorption model in WC-25% Co alloy. 1925-1935A
- Cobalt, Reactions (chemical)**
Investigation on reduction of CoAl_2O_4 by hydrogen gas using TGA. 540-542B
- Cobalt, Recovering**
The thermodynamics of the Ni-Co-S ternary system. 121-128B
- Cobalt, Ternary systems**
The prediction of the hydriding thermodynamics of Pd-Rh-Co ternary alloys. 667-673B
- Cobalt base alloys, Mechanical properties**
Infrared temperature mapping of ULTIMET alloy during high-cycle fatigue tests. 1307-1310A
- Cobalt base alloys, Microstructure**
Investigation on the cold deformation strengthening mechanism in MP 159 alloy. 5-13A
- Cobalt base alloys, Phases (state of matter)**
Liquidus temperature determination in multicomponent alloys by thermal analysis. 497-501A
- Cobalt compounds, Reduction (chemical)**
Investigation on reduction of CoAl_2O_4 by hydrogen gas using TGA. 540-542B
- Coercive force, Microstructural effects**
Insight into the microstructural characterization of ferritic steel using micromagnetic parameters. 1053-1065A
- Coiling**
Microstructural model for hot strip rolling of high-strength low-alloy steels. 1247-1259A
- Coke, Oxidation**
Kinetics of oxidation of carbonaceous materials by CO_2 and H_2O between 1300° and 1500°C. 43-54B
- Coke, Reactions (chemical)**
Coal pyrolysis in a rotary kiln. I. Model of the pyrolysis of a single grain. 381-390B
Coal pyrolysis in a rotary kiln. II. Overall model of the furnace. 391-402B
- Cold rolling**
Preparation and mechanical properties of highly densified nanocrystalline Al. 1017-1024A
Through-thickness texture gradients in cold-rolled aluminum. Deformation behavior of a $\text{Ni}_3\text{Al}(\text{B}, \text{Zr})$ alloy during cold rolling. I. Changes in order and structure. 1653-1662A
Deformation behavior of a $\text{Ni}_3\text{Al}(\text{B}, \text{Zr})$ alloy during cold rolling. II. Microstructural and textural changes. 3001-3010A
3011-3021A
- Cold rolling, Alloying effects**
Recovery and ordering in cold-rolled boron-doped $\text{Ni}_{75}\text{Al}_{25}$. 2127-2134A
- Cold working**
Investigation on the cold deformation strengthening mechanism in MP 159 alloy. 5-13A
- Columnar structure**
Solidification parameters during the columnar-to-equiaxed transition in lead-tin alloys. 1611-1625A
On convection in mushy phase and its effect on macrosegregation. 1687-1692A
A two-dimensional model for the description of the columnar-to-equiaxed transition in competing gray and white iron eutectics and its application to calender rolls. 2059-2068A
- Columnar structure, Composition effects**
Microstructure and formability of ZnNi alloy electrodeposited sheet steel. 475-485A
- Columnar structure, Processing effects**
Effects of processing variables on the microsegregation of directionally cast samples. 3137-3148A
- Columnar structure, Vibration effects**
Effects of the intensity and frequency of electromagnetic vibrations on the microstructural refinement of hypoeutectic Al-Si alloys. 755-762A
- Combustion**
Comparison between sulfide flash smelting and coal combustion—with implications for the flash smelting of high-grade concentrate. 1005-1012B
- Compacting**
Preparation and mechanical properties of highly densified nanocrystalline Al. 1017-1024A
- Compressive strength, Composition effects**
Design of quaternary Ir-Nb-Ni-Al refractory superalloys. 173-178A
- Compressive strength, Processing effects**
Reactive infiltration processing and secondary compressive creep of NiAl and NiAl-W composites. 781-792A
An investigation of the synthesis of Ti-50 at.% Ni alloys through combustion synthesis and conventional powder sintering. 1867-1871A
- Computer programs**
A Scheil-Gulliver model with back-diffusion applied to the microsegregation of chromium in Fe-Cr-C alloys. 1682-1684A
- Computer simulation**
The use of the finite-element method to design an optimized tool for the plain-strain punch stretching test. 93-98A
Simulation of metal-matrix composite isothermal infiltration processing. 225-234B
Thermodynamic-kinetic simulation of constrained dendrite growth in steels. 365-379B
Three-dimensional Monte Carlo simulation of grain growth in the heat-affected zone of a 2.25Cr-1Mo steel weld. 529-536B
Fundamental theories and concepts for predicting thermodynamic properties of high temperature ionic and metallic liquid solutions and vapor molecules. 579-586B
Computer simulation of the initial rafting process of a nickel-base single-crystal superalloy. 585-597A
Development of a thermodynamic database for cemented carbides for design and processing simulations. 615-619B
Simulation of shear plugging through thin plates using the GRIM Eulerian hydrocode. 853-860A
A process model for the heat-affected zone microstructure evolution in duplex stainless steel weldments. II. Application to electron beam welding. 1035-1048A
The ionic properties of CaSiO_3 melt. 1241-1245B
Alpha case thickness modeling in investment castings. 1419-1427B
Modeling of gas-liquid reactions in ladle metallurgy. II. Numerical simulation. 1457-1464B
Mathematical modeling of the dynamic behavior of gas tungsten arc weld pools. 1465-1473B
A Monte Carlo simulation study of dissolution of graphite in iron-carbon melts. 1517-1525B
Residual strains in HY 100 polycrystals: comparisons of experiments and simulations. 1543-1555A
Anisotropic grain growth based on the atomic adsorption model in WC-25% Co alloy. 1925-1935A
Modeling creep and fatigue of copper alloys. 2491-2502A
Monte Carlo sampling for microsegregation measurements in cast structures. 2569-2574A
Transient liquid-phase bonding in the Ni-Al-B system. 2835-2847A
Effect of computational domain size on the mathematical modeling of transport processes and segregation during directional solidification. 3129-3135A
Simulation of percolation structure of grain bonding in liquid-phase sintering by three-dimensional grain structure reconstruction. 3187-3193A
- Concentration (composition)**
Measurement of the activity of boron in liquid copper using a four-phase equilibrium technique. 2674-2678A
- Consolidation**
Processing and microstructural characterization of Al-Cu alloys produced from rapidly solidified powders. 249-260A
Modeling the reaction synthesis of shock-densified titanium-silicon powder mixture compacts. 307-316B
Mechanisms, models and simulations of metal-coated fiber consolidation. 1271-1282A
Study of 6061- Al_2O_3 composites produced by reciprocating extrusion. 2587-2596A
- Containers, Materials selection**
Grain-boundary chemistry and intergranular corrosion in alloy 825. 1163-1173A
- Continuous cast shapes, Mechanical properties**
A new criterion for internal crack formation in continuously cast steels. 779-794B
- Continuous cast shapes, Quality control**
Fluid flow and inclusion removal in continuous casting tundish. 253-266B
- Continuous casting**
Phase diagram for the system $\text{CaO-Al}_2\text{O}_3\text{-ZrO}_2$. 25-33B

- Argon solubility in molten iron. 216-218B
- Prediction of cracks in continuously cast steel beam blank through fully coupled analysis of fluid flow, heat transfer, and deformation behavior of a solidifying shell. 225-237A
- A comparative study of the microstructures observed in statically cast and continuously cast Bi-In-Sn ternary eutectic alloy. 239-248A
- Water model study of horizontal molten steel—Ar two-phase jet in a continuous casting mold. 453-460B
- Dynamics of the spout of gas plumes discharging from a melt: experimental investigation with a large-scale water model. 461-468B
- A new criterion for internal crack formation in continuously cast steels. 779-794B
- Two-fluid simulation on the mixed convection flow pattern in a nonisothermal water model of continuous casting tundish. 867-875B
- Phase diagram cuspidine ($3\text{CaO} \cdot 2\text{SiO}_2 \cdot \text{CaF}_2$)- CaF_2 . 1273-1281B
- Modeling of molten metal flow in a continuous casting process considering the effects of argon gas injection and static magnetic-field application. 1491-1503B
- Continuous casting, Field effects**
- The effect of a uniform direct current magnetic field on the stability of a stratified liquid flux/molten steel system. 317-326B
- Continuous casting, Quality control**
- Fluid flow and inclusion removal in continuous casting tundish. 253-266B
- Depth of oscillation marks forming in continuous casting of steel. 813-826B
- Convection**
- Mushy zone morphology during directional solidification of Pb-5.8 wt.% Sb alloy. 2275-2285A
- Convection, Field effects**
- Numerical calculation of the electromagnetic expulsive force upon nonmetallic inclusions in an aluminum melt. I. Spherical particles. 1527-1533B
- Numerical calculation of the electromagnetic expulsive force upon nonmetallic inclusions in an aluminum melt. II. Cylindrical particles. 1535-1540B
- Convection, Welding effects**
- Unsteady Marangoni flow in a molten pool when welding dissimilar metals. 1387-1403B
- Cooling rate**
- Microstructural evolution in ultra-low-carbon steel weldments. I. Controlled thermal cycling and continuous cooling transformation diagram of the weld metal. 2145-2153A
- The effect of cooling rate on the microstructures formed during solidification of ferritic steel. 3155-3166A
- Copper, Alloying additive**
- Experimental investigation and thermodynamic calculation of the Ti-Ni-Cu shape memory alloys. 2423-2430A
- Copper, Alloying elements**
- Effects of Cu content and preaging on precipitation characteristics in aluminum alloy 6022. 361-371A
- Copper, Binary systems**
- A numerical and experimental study of the rate of transformation in three directionally grown peritectic systems. 29-34A
- On the mobility of the austenite-ferrite interface in Fe-Co and Fe-Cu. 379-385A
- Measurement of the activity of boron in liquid copper using a four-phase equilibrium technique. 2674-2678A
- Copper, Bonding**
- The role of plasticity in bimaterial fracture with ductile interlayers. 863-872A
- Copper, Coating**
- On the evolution of porosity in spray-deposited tool steels. 723-733A
- Growth of a Au-Ni-Sn intermetallic compound on the solder-substrate interface after aging. 798-800A
- Copper, Extraction**
- Galvanic interaction between chalcopyrite and manganese dioxide in sulfuric acid medium. 55-61B
- The electrochemical property of acetylene black suspension solution with ozone bubbling and its effects on copper dissolution. 235-241B
- Microscale simulation of settler processes in copper matte smelting. 439-451B
- Dissolution of lead and bismuth in white metal ($\text{CuS}_{0.5}$) at matte-smelting temperatures. 543-546B
- Phase equilibrium and minor element distribution between FeO_x - SiO_2 -MgO-based slag and Cu_2S -FeS matte at 1573K under high partial pressures of SO_2 . 705-712B
- The study of chlorination kinetics of copper (I) sulfide by calcium chloride in the presence of oxygen. 723-731B
- Comparison between sulfide flash smelting and coal combustion—with implications for the flash smelting of high-grade concentrate. 1005-1012B
- Copper and minor elements distribution between metal, matte, and fluorine slags. 1551-1553B
- Copper, Microstructure**
- Island grains of low misorientation angles formed during abnormal grain growth in Cu. 1489-1491A
- Copper, Physical properties**
- A model of the interfacial heat-transfer coefficient during unidirectional solidification of an aluminum alloy. 285-295B
- Copper, Reactions (chemical)**
- Distribution equilibria of Pb and Cu between CaO - SiO_2 - Al_2NO_3 melts and liquid copper. 1261-1266B
- Copper, Soldering**
- Thermal stability of electroless-nickel/solder interface: A. Interfacial chemistry and microstructure. 2857-2866A
- Thermal stability of electroless-nickel/solder interface: B. Interfacial fatigue resistance. 2867-2875A
- Copper, Ternary systems**
- Enthalpy of mixing of liquid Ni-Zr and Cu-Ni-Zr alloys. 277-284B
- Tin-silver-copper eutectic temperature and composition. 1155-1162A
- Copper, Thermal properties**
- Modeling of interdendritic strain and macrosegregation for dendritic solidification processes. I. Theory and experiments. 331-343B
- Modeling of interdendritic strain and macrosegregation for dendritic solidification processes. II. Computation of interdendritic strain and segregation fields in steel ingots. 345-355B
- Mechanisms of initial melt/substrate heat transfer pertinent to strip casting. 1023-1030B
- Copper, Welding**
- Unsteady Marangoni flow in a molten pool when welding dissimilar metals. 1387-1403B
- Copper base alloys, Electrical properties**
- Chemical synthesis and characterization of low thermal expansion-high conductivity Cu-Mo and Ag-Mo composites. 2396-2398A
- Copper base alloys, Mechanical properties**
- Strength and ductility of heavily drawn bundled Cu-Nb filamentary microcomposite wires with various Nb contents. 2457-2462A
- Modeling creep and fatigue of copper alloys. 2491-2502A
- Synchrotron x-ray study of bulk lattice strains in externally loaded Cu-Mo composites. 2949-2962A
- Copper base alloys, Phases (state of matter)**
- Measurement of the activity of boron in liquid copper using a four-phase equilibrium technique. 2674-2678A
- Copper base alloys, Reactions (chemical)**
- The effects of alkaline earth metal ions and halogen ions on the chromium oxide activities in alkaline earth metal oxide-halide- Cr_2O_3 system fluxes. 469-475B
- Activity measurement of the constituents in liquid Cu-Mg and Cu-Ca alloys with mass spectrometry. 927-935B
- Copper compounds, Crystal growth**
- Effect of increased growth velocity on the growth temperature of the Al- Al_2Cu eutectic. 327-328A
- Copper compounds, Electrochemistry**
- Thermodynamic and nonstoichiometric behavior of promising Hi-Ti cuprate systems via electromotive force measurements: a short review. 661-666B
- Copper compounds, Phase transformations**
- Influence of aging on transformation characteristics in shape memory CuZnAl alloys. 349-354A
- Copper mattes, Reactions (chemical)**
- Microscale simulation of settler processes in copper matte smelting. 439-451B
- Dissolution of lead and bismuth in white metal ($\text{CuS}_{0.5}$) at matte-smelting temperatures. 543-546B
- Phase equilibrium and minor element distribution between FeO_x - SiO_2 -MgO-based slag and Cu_2S -FeS matte at 1573K under high partial pressures of SO_2 . 705-712B
- Copper and minor elements distribution between metal, matte, and fluorine slags. 1551-1553B
- Corrosion fatigue**
- Effect of testing frequency on the corrosion fatigue of a squeeze-cast aluminum alloy. 1137-1145A
- Corrosion mechanisms**
- Reoxidation of hot briquetted iron in salt water. 1133-1135B
- Stress corrosion cracking mechanisms of Alloy 600 polycrystals and single crystals in primary water—influence of hydrogen. 2025-2036A
- Environmentally enhanced deformation of ultra-high-purity Ni-16Cr-9Fe alloys. 2383-2388A
- Corrosion products**
- Reoxidation of hot briquetted iron in salt water. 1133-1135B
- Corrosion resistance, Alloying effects**
- Role of Mo and W during sensitization of superaustenitic stainless steel—crystallography and composition of precipitates. 1893-1905A
- Corrosion resistance, Coating effects**
- Surface amorphous and crystalline microstructure by alloying zirconium using Nd:YAG pulsed laser. 3123-3127A
- Corrosion resistance, Composition effects**
- The effect of aluminum content on the corrosion behavior of Fe-Al alloys in reducing environments at 700°C. 1805-1817A
- Corrosion resistance, Heating effects**
- Influence of thermal aging on the reactivity of duplex stainless steel surfaces. 2015-2024A
- Corundum, Reactions (chemical)**
- Spinel-corundum equilibria and activities in the system MgO - Al_2O_3 - Cr_2O_3 at 1473K. 1323-1332B
- Crack closure**
- Effect of mean stress (stress ratio) and aging on fatigue-crack growth in a metastable beta titanium alloy, Ti-10V-2Fe-3Al. 703-714A
- Crack closure, Corrosion effects**
- Effect of testing frequency on the corrosion fatigue of a squeeze-cast aluminum alloy. 1137-1145A
- Crack closure, Temperature effects**
- Fatigue and fracture toughness of a Nb-Ti-Cr-Al-X single-phase alloy at ambient temperature. 1075-1084A
- Crack initiation**
- An investigation of dynamic failure in 2.3Ni-1.3Cr-0.17C steel. 1147-1154A
- Infrared temperature mapping of ULTIMET alloy during high-cycle fatigue tests. 1307-1310A
- Crack initiation, Alloying effects**

- The influence of Mg on creep properties and fracture behaviors of Mar-M247 superalloy under 1255 K/200 MPa. 1365-1373A
- Crack initiation, Composition effects**
The interactive role of inclusions and SiC reinforcement on the high-cycle fatigue resistance of particle reinforced metal matrix composites. 951-957A
An investigation of the effects of ductile-layer thickness on the fracture behavior of nickel aluminide microlaminates. 1385-1399A
High-temperature fracture and fatigue-crack growth behavior of an XD gamma-based titanium aluminide intermetallic alloy. 1413-1423A
Effect of interfacial debonding and sliding on matrix crack initiation during isothermal fatigue of SCS-6/Ti-15-3 composites. 2637-2645A
- Crack initiation, Heating effects**
Part II. Metallurgical factors governing the H-assisted intergranular cracking of peak-aged Ti-3Al-8V-6Cr-4Mo-4Zr (Beta-C). 81-92A
- Crack initiation, Microstructural effects**
The fracture resistance of a binary TiAl alloy. 71-80A
The mechanism of brittle fracture in a microalloyed steel. I. Inclusion-induced cleavage. 641-652A
The mechanism of brittle fracture in a microalloyed steel. II. Mechanistic modeling. 653-667A
The effect of microstructural banding on failure initiation of HY-100 steel. 995-1005A
An investigation of the effect of fatigue deformation on the residual mechanical properties of Ti-6Al-4V ELI. 1937-1948A
Effects of microstructure on the short fatigue crack initiation and propagation characteristics of biomedical α/β titanium alloys. 1949-1958A
Cyclic deformation, dislocation structure, and internal fatigue crack generation in a Ti-Fe-O alloy at liquid nitrogen temperature. 2793-2805A
- Crack initiation, Welding effects**
Fracture mechanism and toughness of the welding heat-affected zone in structural steel under static and dynamic loading. 2785-2791A
- Crack propagation**
Fatigue crack path prediction in Udimet 720 nickel-based alloy single crystals. 109-123A
Modeling thermomechanical fatigue life of high-temperature titanium alloy IMI 834. 431-444A
Effect of mean stress (stress ratio) and aging on fatigue-crack growth in a metastable beta titanium alloy, Ti-10V-2Fe-3Al. 703-714A
Simulation of shear plugging through thin plates using the GRIM Eulerian hydrocode. 853-860A
Interactions between mechanical and environmental variables for short fatigue cracks in a 2024-T3 aluminum alloy in 0.5M NaCl solutions. 1025-1034A
Ultrasonic attenuation peak in steel and aluminum alloy during rotating bending fatigue. 1121-1128A
Infrared temperature mapping of ULTIMET alloy during high-cycle fatigue tests. 1307-1310A
Effect of strain rate on damage evolution in a cast Al-Si-Mg base alloy. 1725-1731A
Significance of the small crack growth law and its practical application. 2005-2013A
Mechanical behavior and damage kinetics in nodular cast iron. I. Damage mechanisms. 3063-3074A
- Crack propagation, Alloying effects**
The influence of Mg on creep properties and fracture behaviors of Mar-M247 superalloy under 1255 K/200 MPa. 1365-1373A
A comparison study of microstructure and mechanical properties of Ti-24Al-14Nb-3V-0.5Mo with and without Si. 2205-2217A
Relation between microstructure, composition, and hot cracking in Ti-stabilized austenitic stainless steel weldments. 3109-3122A
- Crack propagation, Coating effects**
Effects of sulfur on the fatigue and fracture resistance of interfaces between γ -Ni(Cr) and α -Al₂O₃. 1977-1983A
Thermal stability of electrodeless-nickel/solder interface: B. Interfacial fatigue resistance. 2867-2875A
- Crack propagation, Composition effects**
The interactive role of inclusions and SiC reinforcement on the high-cycle fatigue resistance of particle reinforced metal matrix composites. 951-957A
The quasi-static and cyclic fatigue fracture behavior of 2014 aluminum alloy metal-matrix composites. 959-974A
An investigation of the effects of ductile-layer thickness on the fracture behavior of nickel aluminide microlaminates. 1385-1399A
Fatigue crack growth resistance of unidirectional fiber-reinforced titanium metal-matrix composites under transverse loading. 2083-2092A
- Crack propagation, Corrosion effects**
Effect of testing frequency on the corrosion fatigue of a squeeze-cast aluminum alloy. 1137-1145A
- Crack propagation, Environmental effects**
Effects of inert gases on fatigue crack growth and their transportation into subsurface regions in titanium. 1435-1441A
- Crack propagation, Heating effects**
Part II. Metallurgical factors governing the H-assisted intergranular cracking of peak-aged Ti-3Al-8V-6Cr-4Mo-4Zr (Beta-C). 81-92A
- Crack propagation, High temperature effects**
Dynamic fracture toughness of a Ti-45Al-1.6Mn alloy at high temperature. 3053-3061A
- Crack propagation, Microstructural effects**
The fracture resistance of a binary TiAl alloy. 71-80A
The mechanism of brittle fracture in a microalloyed steel. I. Inclusion-induced cleavage. 641-652A
The mechanism of brittle fracture in a microalloyed steel. II. Mechanistic modeling. 653-667A
- Near-threshold fatigue crack growth behavior of 2195 aluminum-lithium alloy—prediction of crack propagation direction and influence of stress ratio. 1531-1541A
Effects of microstructure on the short fatigue crack initiation and propagation characteristics of biomedical α/β titanium alloys. 1949-1958A
Cyclic deformation, dislocation structure, and internal fatigue crack generation in a Ti-Fe-O alloy at liquid nitrogen temperature. 2793-2805A
- Crack propagation, Processing effects**
A new criterion for internal crack formation in continuously cast steels. 779-794B
- Crack propagation, Temperature effects**
Fatigue and fracture toughness of a Nb-Ti-Cr-Al-X single-phase alloy at ambient temperature. 1075-1084A
- Crack propagation, Vibration effects**
Effect of nodularity on resonant vibration fracture behavior in upper bainitic and ferritic cast irons. 2193-2203A
- Crack propagation, Welding effects**
Friction-stir welding effects on microstructure and fatigue of aluminum alloy 7050-T7451. 2181-2192A
Fracture mechanism and toughness of the welding heat-affected zone in structural steel under static and dynamic loading. 2785-2791A
- Cracking (fracturing)**
Prediction of cracks in continuously cast steel beam blank through fully coupled analysis of fluid flow, heat transfer, and deformation behavior of a solidifying shell. 225-237A
- Creep (materials)**
Mechanisms, models and simulations of metal-coated fiber consolidation. 1271-1282A
- Creep (materials), Alloying effects**
Atom probe field ion microscopy investigation of boron containing martensitic 9% chromium steel. 975-984A
A comparison study of microstructure and mechanical properties of Ti-24Al-14Nb-3V-0.5Mo with and without Si. 2205-2217A
- Creep (materials), Anisotropy**
Creep properties of Ni₃(AlTiTa) γ' phase single crystals. 1733-1740A
- Creep (materials), High temperature effects**
The effect of high-temperature oxidation on the creep behavior of a superalloy (Nimonic-105). 1777-1784A
- Creep (materials), Microstructural effects**
Creep expansion of porous Ti-6Al-4V sandwich structures. 261-273A
On the primary creep of CMSX-4 superalloy single crystals. 2219-2228A
- Creep (materials), Processing effects**
High-temperature creep of an Al-8.5Fe-1.3V-1.7Si alloy processed by rapid solidification. 2229-2237A
- Creep life, Impurity effects**
The influence of sulfur on stress-rupture fracture in Inconel 718 superalloys. 2135-2144A
- Creep life, Processing effects**
Enhanced densification of cavitated dispersion-strengthened aluminum by thermal cycling. 2647-2657A
- Creep rate, Processing effects**
Reactive infiltration processing and secondary compressive creep of NiAl and NiAl-W composites. 781-792A
- Creep rupture strength**
Creep-behavior modeling of the single-crystal superalloy CMSX-4. 1401-1411A
- Creep rupture strength, Heating effects**
Creep rupture mechanisms in annealed and overheated 7075 Al under multiaxial stress states. 2807-2821A
- Creep rupture strength, Impurity effects**
The influence of sulfur on stress-rupture fracture in Inconel 718 superalloys. 2135-2144A
- Creep rupture strength, Microstructural effects**
Anisotropic behavior and rupture of hydrided Zircaloy-4 sheets. 679-690A
- Creep rupture strength, Welding effects**
Creep deformation and fracture behavior of types 316 and 316L(N) stainless steels and their weld metals. 1175-1185A
- Creep strength**
Effect of plastic anisotropy on the creep strength of single crystals of a nickel-based superalloy. 421-430A
Modeling creep and fatigue of copper alloys. 2491-2502A
- Creep strength, Alloying effects**
The influence of Mg on creep properties and fracture behaviors of Mar-M247 superalloy under 1255 K/200 MPa. 1365-1373A
- Creep strength, Microstructural effects**
Creep deformation of TiAl-Si alloys with aligned γ/α_2 lamellar microstructures. 2463-2473A
- Creep strength, Processing effects**
Enhanced densification of cavitated dispersion-strengthened aluminum by thermal cycling. 2647-2657A
- Crevice corrosion, Alloying effects**
Role of Mo and W during sensitization of superaustenitic stainless steel—crystallography and composition of precipitates. 1893-1905A
- Criteria**
A new criterion for internal crack formation in continuously cast steels. 779-794B
- Critical temperature**
Liquidus temperature determination in multicomponent alloys by thermal analysis. 497-501A
Tin-silver-copper eutectic temperature and composition. 1155-1162A
Displacive transformations in Au-18 wt.% Cu-6 wt.% Al. 1917-1923A

Critical temperature, Composition effects

- Alloy design of FeMnSiCrNi shape-memory alloys related to stacking-fault energy. 581-584A

Cryolite, Physical properties

- A new approach to numerical simulation of melt flows and interface instability in Hall-Héroult cells. 1541-1550B

Cryolite, Reactions (chemical)

- Some generalities in the analyses of equilibria in ionic solutions. 2105-2118A

Cryolite, Solubility

- Solutions of iron oxides in molten cryolite. 609-613B

Crystal defects

- Microstructural studies on lattice imperfections in deformed zirconium-base alloys by x-ray diffraction. 2405-2410A

Crystal structure

- The identification of hydrogen trapping states in an Al-Li-Cu-Zr alloy using thermal desorption spectroscopy. 179-193A

Crystal structure, Processing effects

- Microstructural characterization of a rapidly solidified ultrahigh strength $Al_{94.5}Cr_3Co_{1.5}Ce_1$ alloy. 607-614A

Crystallization

- Crystallization of amorphous $Fe_{82}P_{18}$. 1067-1073A
Effect of long-term room-temperature storage on the structure and properties of glassy melt-spun Mg-Al-Ca alloys. 2155-2162A

Crystallization, Environmental effects

- The effect of water vapor on mold slag crystallization. 403-406B

Current density

- On the mechanism of the anode effect in aluminum electrolysis. 1225-1230B

Cyclic loads

- Load sharing between austenite and ferrite in a duplex stainless steel during cyclic loading. 1557-1570A

Damage

- Damage leading to ductile fracture under high strain-rate conditions. 831-844A

- Quantitative description of damage evolution in ductile fracture of tantalum. 845-851A

- Role of foreign-object damage on thresholds for high-cycle fatigue in Ti-6Al-4V. 1571-1583A

- Effect of strain rate on damage evolution in a cast Al-Si-Mg base alloy. 1725-1731A

- Mechanical behavior and damage kinetics in nodular cast iron. I. Damage mechanisms. 3063-3074A

- Mechanical behavior and damage kinetics in nodular cast iron. II. Hardening and damage. 3075-3085A

- Identification of rolling-sliding damage mechanisms in porous alloys. 3091-3099A

Damage, Deformation effects

- Synchrotron x-ray study of bulk lattice strains in externally loaded Cu-Mo composites. 2949-2962A

Damage, High temperature effects

- The effect of high-temperature oxidation on the creep behavior of a superalloy (Nimonic-105). 1777-1784A

Damage tolerance

- The effect of impact damage on the room-temperature fatigue behavior of γ -TiAl. 1741-1752A

Debonding, Composition effects

- Effect of interfacial debonding and sliding on matrix crack initiation during isothermal fatigue of SCS-6/Ti-15-3 composites. 2637-2645A

Decarburizing

- On methane generation and decarburization in low-alloy Cr-Mo steels during hydrogen attack. 125-137A

Defects

- Microstructure-ultrasonic inspectability relationships in Ti6242: signal-to-noise in fine-grain-processed Ti6242. 2119-2125A

Deformation

- The use of the finite-element method to design an optimized tool for the plain-strain punch stretching test. 93-98A

- Comparison between high and low strain-rate deformation of tantalum. 815-823A

Deformation, Heating effects

- Deformation and fracture of a particle-reinforced aluminum alloy composite. I. Experiments. 921-936A

- Deformation and fracture of a particle-reinforced aluminum alloy composite. II. Modeling. 937-950A

Deformation, High temperature effects

- Stress-strain response of a cast 319-T6 aluminum under thermomechanical loading. 139-151A

Deformation, Microstructural effects

- Effects of martensite morphology and volume fraction on quasi-static and dynamic deformation behavior of dual-phase steels. 1753-1760A

Deformation mechanisms

- Effect of microstructure variations on the formation of deformation-induced martensite and associated tensile properties in a β metastable Ti alloy. 1095-1106A

- δ/γ interface boundary sliding as a mechanism of strain accommodation during hot deformation in a duplex stainless steel. 1671-1677A

- The influence of crystallographic texture and interstitial impurities on the mechanical behavior of zirconium. 1997-2003A

- Evolution of texture and grain misorientation in an Al-Mg alloy exhibiting low-temperature superplasticity. 2169-2180A

- Hot deformation mechanisms in a powder metallurgy nickel-base superalloy IN 625. 2317-2325A

- Yield vertices for {123}<111> multiple slip. 2449-2456A

Deformation mechanisms, Microstructural effects

- Anisotropic behavior and rupture of hydrided Zircaloy-4 sheets. 679-690A

Degassing

- Modeling of gas-liquid reactions in ladle metallurgy. I. Physical modeling. 1447-1455B

- Modeling of gas-liquid reactions in ladle metallurgy. II. Numerical simulation. 1457-1464B

Dehydration

- Quantifying the heats of coal devolatilization. 1125-1131B

Dendritic structure

- A comparative study of the microstructures observed in statically cast and continuously cast Bi-In-Sn ternary eutectic alloy. 239-248A

- Modeling of interdendritic strain and macrosegregation for dendritic solidification processes. I. Theory and experiments. 331-343B

- Modeling of interdendritic strain and macrosegregation for dendritic solidification processes. II. Computation of interdendritic strain and segregation fields in steel ingots. 345-355B

- Thermodynamic-kinetic simulation of constrained dendrite growth in steels. 365-379B

- Influence of solidification variables on the dendrite arm spacings of Ni-based superalloys. 546-551B

- Mushy zone morphology during directional solidification of Pb-5.8 wt.% Sb alloy. 2275-2285A

- Correlation between unsteady-state solidification conditions, dendrite spacings, and mechanical properties of Al-Cu alloys. 3167-3178A

Dendritic structure, Coating effects

- Application of the phase-field method to the solidification of hot-dipped galvanized coatings. 487-495A

- Microstructural evolution during laser cladding of M2 high-speed steel. 2615-2625A

Dendritic structure, Cooling effects

- An integrated model for dendritic and planar interface growth and morphological transition in rapid solidification. 735-746A

Dendritic structure, Processing effects

- Effects of processing variables on the microsegregation of directionally cast samples. 3137-3148A

Dendritic structure, Vibration effects

- Effects of the intensity and frequency of electromagnetic vibrations on the microstructural refinement of hypoeutectic Al-Si alloys. 755-762A

Densification

- Preparation and mechanical properties of highly densified nanocrystalline Al. 1017-1024A

- Mechanisms, models and simulations of metal-coated fiber consolidation. 1271-1282A

- Improved densification of carbonyl iron compacts by the addition of fine alumina powders. 1645-1652A

- Study of 6061- Al_2O_3 composites produced by reciprocating extrusion. 2587-2596A

- Enhanced densification of cavitated dispersion-strengthened aluminum by thermal cycling. 2647-2657A

Densification, Alloying effects

- Dilatometry study of the sintering behavior of boron-alloyed Fe-1.5% Mo powder. 1497-1506A

Density, Composition effects

- Synthesis of $MoSi_2$ -TiSi₂ pseudobinary alloys by reactive sintering. 747-753A

Density, Microstructural effects

- Creep expansion of porous Ti-6Al-4V sandwich structures. 261-273A

Deoxidizing

- Measurement of the activity of boron in liquid copper using a four-phase equilibrium technique. 2674-2678A

Diamond pyramid hardness

- Microhardness study of the nonlinear optical crystal L-arginine hydrochloride monohydrate. 3087-3090A

Diamond pyramid hardness, Heating effects

- Discussion of "Surface relief and the displacive transformation to the lamellar microstructure in TiAl" and "Nanometer-scale, fully lamellar microstructure in an aged TiAl-based alloy". 2377-2379A

- Author's reply to: Discussion of "Surface relief and the displacive transformation to the lamellar microstructure in TiAl" and "Nanometer-scale, fully lamellar microstructure in an aged TiAl-based alloy". 2379-2383A

Diamond pyramid hardness, Microstructural effects

- An investigation of the effect of fatigue deformation on the residual mechanical properties of Ti-6Al-4V ELI. 1937-1948A

Diamond pyramid hardness, Processing effects

- On the infiltration behavior of Al, Al-Li, and Mg melts through SiC_p bed. 319-325A

Diffusivity

- The chemical diffusivity of oxygen in liquid iron oxide and a calcium ferrite. 1059-1068B

- Interdiffusion of Sn and Pb in liquid Pb-Sn alloys. 1343-1352A

- On homogenization of a binary alloy after dissolution of planar and spherical precipitates. 1525-1530A

- A Scheil-Gulliver model with back-diffusion applied to the microsegregation of chromium in Fe-Cr-C alloys. 1682-1684A

- Modeling gas diffusion into metals with a moving-boundary phase transformation. 2411-2421A

- Pseudobinary diffusion coefficients in the Ti-Mo-Ta system. 3198-3199A

Diffusivity, Composition effects

- Hydrogen diffusion coefficients in the titanium alloys IMI 834, Ti 10-2-3, Ti 21 S, and Alloy C. 1507-1517A

- An interdiffusion study of a NiAl alloy using single-phase diffusion. 1507-1517A

- sion couples. 1519-1524A
- Diffusivity, Corrosion effects**
- Selective oxidation and internal nitridation during high-temperature exposure of single-crystalline nickel-base superalloys. 47-56A
- Diffusivity, Temperature effects**
- Diffusion of oxygen in the Al_2O_3 oxidation product of $TiAl_3$. 3023-3028A
- Direct chill casting**
- Two-phase modeling of mushy zone parameters associated with hot tearing. 1461-1472A
- Determination of thermophysical properties and boundary conditions of direct chill-cast aluminum alloys using inverse methods. 1627-1634A
- Direct reduced iron, Corrosion**
- Reoxidation of hot briquetted iron in salt water. 1133-1135B
- Direct reduction**
- Influence of ash on mass transfer and interfacial reaction between natural graphite and liquid iron. 1099-1104B
- Reoxidation of hot briquetted iron in salt water. 1133-1135B
- Directional solidification**
- An oscillatory behavior of planar interface motion in the naphthalene-camphor system. 2678-2681A
- Directional solidification, Field effects**
- Further discussion of "Particle engulfment and pushing by solidifying interfaces. II. Microgravity experiments and theoretical analysis". 1695-1700A
- Authors' reply to: Further discussion of "Particle engulfment and pushing by solidifying interfaces. II. Microgravity experiments and theoretical analysis". 1700-1704A
- Directionally solidified eutectics, Crystal growth**
- Effect of increased growth velocity on the growth temperature of the Al-Al₂Cu eutectic. 327-328A
- Directionally solidified eutectics, Mechanical properties**
- Creep deformation of TiAl-Si alloys with aligned γ/α_2 lamellar microstructures. 2463-2473A
- Directionally solidified eutectics, Microstructure**
- Effect of computational domain size on the mathematical modeling of transport processes and segregation during directional solidification. 3129-3135A
- Dislocation density**
- Microstructural studies on lattice imperfections in deformed zirconium-base alloys by x-ray diffraction. 2405-2410A
- Dislocation density, Deformation effects**
- Investigation on the cold deformation strengthening mechanism in MP 159 alloy. 5-13A
- Dislocation mobility**
- The limiting speeds of dislocations. 811-814A
- Creep-behavior modeling of the single-crystal superalloy CMSX-4. 1401-1411A
- Dislocations**
- Cyclic deformation, dislocation structure, and internal fatigue crack generation in a Ti-Fe-O alloy at liquid nitrogen temperature. 2793-2805A
- Dispersion hardening alloys, Mechanical properties**
- The role of dispersed particles in strengthening and fracture mechanisms in a Mo-ZrC alloy processed by mechanical alloying. 715-721A
- Enhanced densification of cavitated dispersion-strengthened aluminum by thermal cycling. 2647-2657A
- Dispersions, Welding effects**
- Dispersoid-free zones in the heat-affected zone of aluminum alloy welds. 1453-1459A
- Dissimilar metals, Welding**
- Unsteady Marangoni flow in a molten pool when welding dissimilar metals. 1387-1403B
- Dissolution**
- Dissolution rates of coals and graphite in Fe-C-S melts in direct ironmaking: dependence of carbon dissolution rate on carbon structure. 215-216B
- Dissolution rates of coals and graphite in Fe-C-S melts in direct ironmaking: influence of melt carbon and sulfur on carbon dissolution. 243-251B
- Kinetics of Al_2O_3 dissolution in CaO-MgO-SiO₂- Al_2O_3 slags: in situ observations and analysis. 406-410B
- Dissolution of lead and bismuth in white metal ($Cu_{50}S_{50}$) at matte-smelting temperatures. 543-546B
- A Monte Carlo simulation study of dissolution of graphite in iron-carbon melts. 1517-1525B
- On homogenization of a binary alloy after dissolution of planar and spherical precipitates. 1525-1530A
- Modeling of dissolution, growth, and coarsening of aluminum nitride in low-carbon steels. 1907-1916A
- Dissolution, Alloying effects**
- Effects of aluminum, silicon, and boron on the dissolution rate of nitrogen into molten iron. 899-904B
- Dissolution, Welding effects**
- Numerical modeling of enhanced nitrogen dissolution during gas tungsten arc welding. 1371-1385B
- Distortion, Welding effects**
- A process model for the distortion induced by the electron-beam welding of a nickel-based superalloy. 2261-2273A
- Dual phase steels, Mechanical properties**
- Effects of martensite morphology and volume fraction on quasi-static and dynamic deformation behavior of dual-phase steels. 1753-1760A
- Ductile fracture**
- Damage leading to ductile fracture under high strain-rate conditions. 831-844A
- Quantitative description of damage evolution in ductile fracture of tantalum. 845-851A
- Ductile fracture, Impurity effects**
- The influence of sulfur on stress-rupture fracture in Inconel 718 superalloys. 2135-2144A
- Ductility**
- An analysis of the effect of cavity nucleation rate and cavity coalescence on the tensile behavior of superplastic materials. 1425-1434A
- Ductility, Composition effects**
- The influence of reinforcement particle size distribution on the mechanical behavior of a stainless steel/TiN composite. 309-318A
- Strength and ductility of heavily drawn bundled Cu-Nb filamentary microcomposite wires with various Nb contents. 2457-2462A
- Ductility, High temperature effects**
- The effect of high-temperature oxidation on the creep behavior of a superalloy (Nimonic-105). 1777-1784A
- Ductility, Impurity effects**
- The influence of sulfur on stress-rupture fracture in Inconel 718 superalloys. 2135-2144A
- Ductility, Microstructural effects**
- The effect of processing and microstructure development on the slip and fracture behavior of the 2.1 wt.% Li AF/C-489 and 1.8 wt.% Li AF/C-458 Al-Li-C-X alloys. 1965-1976A
- Ductility, Processing effects**
- Effects of strain rate and anisotropy on the tensile deformation properties of extruded AlZnMg alloys. 669-678A
- Characteristics of Mg-based composites synthesized using a novel mechanical disintegration and deposition technique. 1873-1881A
- Ductility, Welding effects**
- Friction-stir welding effects on microstructure and fatigue of aluminum alloy 7050-T7451. 2181-2192A
- Weld metal ductility in aluminum tailor welded blanks. 2755-2763A
- Duplex stainless steels, Corrosion**
- Influence of thermal aging on the reactivity of duplex stainless steel surfaces. 2015-2024A
- Duplex stainless steels, Mechanical properties**
- Influence of microstructure on the flow behavior of duplex stainless steels at high temperatures. 1353-1364A
- Load sharing between austenite and ferrite in a duplex stainless steel during cyclic loading. 1557-1570A
- δ/γ interface boundary sliding as a mechanism of strain accommodation during hot deformation in a duplex stainless steel. 1671-1677A
- Duplex stainless steels, Metal working**
- Superplastic forming of duplex stainless steel. 2394-2396A
- Duplex stainless steels, Microstructure**
- Early-stage Widmanstätten growth of the γ phase in a duplex steel. 15-19A
- Duplex stainless steels, Phase transformations**
- Mechanical properties, microstructural stability and kinetics of α -phase formation in 29Cr-6Ni-2Mo-0.38N superduplex stainless steel. 35-45A
- Duplex stainless steels, Welding**
- A process model for the heat-affected zone microstructure evolution in duplex stainless steel weldments. II. Application to electron beam welding. 1035-1048A
- Dynamic mechanical properties, Processing effects**
- Correlation of microstructure with dynamic deformation behavior and penetration performance of tungsten heavy alloys fabricated by mechanical alloying. 2475-2489A
- Economics**
- Steel at the millennium. 561-575B
- Efficiency**
- A mathematical model of aluminum depth filtration with ceramic foam filters. I. Validation for short-term filtration. 491-502B
- A mathematical model of aluminum depth filtration with ceramic foam filters. II. Application to long-term filtration. 503-513B
- Elastic anisotropy**
- Anisotropy of yielding in a Zr-2.5Nb pressure tube material. 409-420A
- Effect of plastic anisotropy on the creep strength of single crystals of a nickel-based superalloy. 421-430A
- Elastic anisotropy, Heating effects**
- Effect of intermediate annealing on texture evolution and plastic anisotropy in an Al-Mg autobody alloy. 99-107A
- Elastic anisotropy, Microstructural effects**
- Anisotropic behavior and rupture of hydrided Zircaloy-4 sheets. 679-690A
- Elastic anisotropy, Processing effects**
- Effects of strain rate and anisotropy on the tensile deformation properties of extruded AlZnMg alloys. 669-678A
- Electric arc furnaces**
- Kinetics of manganese ore reduction by carbon monoxide. 477-490B
- Equilibrium slag losses in ferrovanadium production. 1091-1097B
- Electroless nickel plating**
- Thermal stability of electroless-nickel/solder interface: A. Interfacial chemistry and microstructure. 2857-2866A
- Thermal stability of electroless-nickel/solder interface: B. Interfacial fatigue resistance. 2867-2875A
- Electrolysis**
- Melt penetration and chemical reactions in 16 industrial aluminum carbon cathodes. 1213-1224B
- On the mechanism of the anode effect in aluminum electrolysis. 1225-1230B

- Electrolytic cells, Electrochemistry**
Solutions of iron oxides in molten cryolite. Melt penetration and chemical reactions in 16 industrial aluminum carbon cathodes. On the mechanism of the anode effect in aluminum electrolysis. 609-613B
- Electromagnetic fields**
Equilibrium shape of a molten silicon drop in an electromagnetic levitator in microgravity environment. Numerical calculation of the electromagnetic repulsive force upon nonmetallic inclusions in an aluminum melt. I. Spherical particles. 1213-1224B
Numerical calculation of the electromagnetic repulsive force upon nonmetallic inclusions in an aluminum melt. II. Cylindrical particles. 1225-1230B
- Electromagnetic induction**
Effects of the intensity and frequency of electromagnetic vibrations on the microstructural refinement of hypoeutectic Al-Si alloys. 327-329B
- Electromagnetic stirring**
The effect of a uniform direct current magnetic field on the stability of a stratified liquid flux/molten steel system. 1527-1533B
- Electrometallurgy**
Galvanic interaction between chalcocopyrite and manganese dioxide in sulfuric acid medium. Electrodeposition of zinc from sodium zincate/hydroxide electrolytes in a spouted bed electrode. 1535-1540B
- Electrometallurgy, Materials selection**
Coal pyrolysis in a rotary kiln. I. Model of the pyrolysis of a single grain. 755-762A
Coal pyrolysis in a rotary kiln. II. Overall model of the furnace. 317-326B
- Electron beam melting**
Aluminum volatilization and inclusion removal in the electron beam cold hearth melting of Ti alloys. Theoretical and experimental investigations of electron beam surface remelting and alloying. 55-61B
- Electron beam processing**
Microstructural analysis of vanadium carbide/steel surface-alloyed materials fabricated by high-energy electron-beam irradiation. 755-766B
- Electron beam welding**
A process model for the distortion induced by the electron-beam welding of a nickel-based superalloy. 381-390B
- Electron beam welding, Quality control**
A process model for the heat-affected zone microstructure evolution in duplex stainless steel weldments. II. Application to electron beam welding. 391-402B
- Electronic devices, Coating**
Growth of a Au-Ni-Sn intermetallic compound on the solder-substrate interface after aging. 845-854B
- Electroplating**
Microstructure and formability of ZnNi alloy electrodeposited sheet steel. Theoretical and experimental investigations of electron beam surface remelting and alloying. 1405-1417B
- Electrowinning**
Solubilities and Raman spectra of NdOCl in some chloride melts of interest for the electrowinning of magnesium from its oxide. The anomalous behavior of Al^{3+} in nickel electrowinning from sulfate electrolytes. 2849-2855A
- Elongated structure**
Correlation between former alpha boundary growth kinetics and superplastic flow in Zn-22% Al. 2261-2273A
- Elongation**
Effect of microstructure variations on the formation of deformation-induced martensite and associated tensile properties in a β metastable Ti alloy. 1035-1048A
- Elongation, Alloying effects**
A comparison study of microstructure and mechanical properties of Ti-24Al-14Nb-3V-0.5Mo with and without Si. Effects of boron doping on the grain-growth kinetics and mechanical properties of γ/γ' nickel-aluminum alloys. 798-800A
- Elongation, Composition effects**
Microstructure and properties of in situ Al/TiB₂ composite fabricated by in-melt reaction method. 475-485A
- Elongation, Microstructural effects**
The effect of processing and microstructure development on the slip and fracture behavior of the 2.1 wt.% Li AF/C-489 and 1.8 wt.% Li AF/C-458 Al-Li-C-X alloys. 755-766B
- Elongation, Processing effects**
The role of dispersed particles in strengthening and fracture mechanisms in a Mo-ZrC alloy processed by mechanical alloying. Preparation and mechanical properties of highly densified nanocrystalline Al. 631-639B
- Elongation, Welding effects**
Friction-stir welding effects on microstructure and fatigue of aluminum alloy 7050-T7451. 1203-1211B
- Embrittlement, Radiation effects**
A Bayesian analysis of the influence of neutron irradiation on embrittlement in ferritic submerged arc weld metal. 163-172A
- Engine components, Mechanical properties**
Role of foreign-object damage on thresholds for high-cycle fatigue in Ti-6Al-4V. 1095-1106A
- Enthalpy**
Enthalpy of mixing of liquid Ni-Zr and Cu-Ni-Zr alloys. 2205-2217A
- Equal channel angular pressing**
Equal-channel angular pressing of commercial aluminum alloys: grain refinement, thermal stability and tensile properties. 3179-3186A
- Equiaxed structure**
Solidification parameters during the columnar-to-equiaxed transition in lead-tin alloys. An investigation of the effect of fatigue deformation on the residual mechanical properties of Ti-6Al-4V ELI. Effects of microstructure on the short fatigue crack initiation and propagation characteristics of biomedical α/β titanium alloys. A two-dimensional model for the description of the columnar-to-equiaxed transition in competing gray and white iron eutectics and its application to calendar rolls. 1611-1625A
- Equiaxed structure, Deformation effects**
Substructural changes during hot deformation of a Fe-26Cr ferritic stainless steel. 1937-1948A
- Equiaxed structure, Processing effects**
Effects of processing variables on the microsegregation of directionally cast samples. 1949-1958A
- Equiaxed structure, Vibration effects**
Effects of the intensity and frequency of electromagnetic vibrations on the microstructural refinement of hypoeutectic Al-Si alloys. 2059-2068A
- Eutectic composition**
Tin-silver-copper eutectic temperature and composition. Eutectic interface configurations during melting. 21-27A
- Eutectic reactions**
Tin-silver-copper eutectic temperature and composition. Eutectic interface configurations during melting. 3137-3148A
- Eutectoid reactions, Heating effects**
The role of the divorced eutectoid transformation in the spheroidization of 52100 steel. 755-762A
- Evaporation**
Evaporation behavior of aluminum during the cold crucible induction skull melting of titanium aluminum alloys. 1155-1162A
- Extractive metallurgy**
Aspects of technology transfer. 1261-1269A
- Extrusion**
Effect of particle size and volume fraction in hot extrusion reaction synthesis of SiC particle reinforced NiAl. Microstructural characterization of novel in-situ Al-Be composites. 1155-1162A
- Extrusions, Mechanical properties**
Effects of strain rate and anisotropy on the tensile deformation properties of extruded AlZnMg alloys. 1261-1269A
- Failure**
Strain-localization in sheet metal containing a geometric defect. 2431-2438A
- Failure, Microstructural effects**
The effect of microstructural banding on failure initiation of HY-100 steel. 837-844B
- Failure analysis**
Analysis of secondary oxide-scale failure at entry into the roll gap. 1153-1162B
- Fatigue failure**
Fatigue crack path prediction in Udimet 720 nickel-based alloy single crystals. Modeling thermomechanical fatigue life of high-temperature titanium alloy IMI 834. Effect of mean stress (stress ratio) and aging on fatigue-crack growth in a metastable beta titanium alloy, Ti-10V-2Fe-3Al. Interactions between mechanical and environmental variables for short fatigue cracks in a 2024-T3 aluminum alloy in 0.5M NaCl solutions. Ultrasonic attenuation peak in steel and aluminum alloy during rotating bending fatigue. Heat generation during the fatigue of a cellular Al alloy. Infrared temperature mapping of ULTIMET alloy during high-cycle fatigue tests. The effect of impact damage on the room-temperature fatigue behavior of γ -TiAl. Significance of the small crack growth law and its practical application. 1663-1670A
- Fatigue failure, Alloying effects**
A comparison study of microstructure and mechanical properties of Ti-24Al-14Nb-3V-0.5Mo with and without Si. 2963-2971A
- Fatigue failure, Composition effects**
The interactive role of inclusions and SiC reinforcement on the high-cycle fatigue resistance of particle reinforced metal matrix composites. The quasi-static and cyclic fatigue fracture behavior of 2014 aluminum alloy metal-matrix composites. High-temperature fracture and fatigue-crack growth behavior of an XD gamma-based titanium aluminide intermetallic alloy. Fatigue crack growth resistance of unidirectional fiber-reinforced titanium metal-matrix composites under transverse loading. Effect of interfacial debonding and sliding on matrix crack initiation during isothermal fatigue of SCS-6/Ti-15-3 composites. 669-678A
- Fatigue failure, Corrosion effects**
Effect of testing frequency on the corrosion fatigue of a squeeze-cast aluminum alloy. 1883-1886A

- Fatigue failure, Environmental effects**
Effects of inert gases on fatigue crack growth and their transportation into subsurface regions in titanium. 1435-1441A
- Fatigue failure, Microstructural effects**
Near-threshold fatigue crack growth behavior of 2195 aluminum-lithium alloy—prediction of crack propagation direction and influence of stress ratio. 1531-1541A
An investigation of the effect of fatigue deformation on the residual mechanical properties of Ti-6Al-4V ELI. 1937-1948A
Cyclic deformation, dislocation structure, and internal fatigue crack generation in a Ti-Fe-O alloy at liquid nitrogen temperature. 2793-2805A
- Fatigue failure, Temperature effects**
Thermal activation of fatigue damage. 63-69A
- Fatigue failure, Vibration effects**
Effect of nodularity on resonant vibration fracture behavior in upper bainitic and ferritic cast irons. 2193-2203A
- Fatigue failure, Welding effects**
Friction-stir welding effects on microstructure and fatigue of aluminum alloy 7050-T7451. 2181-2192A
- Fatigue life**
Modeling thermomechanical fatigue life of high-temperature titanium alloy IMI 834. 431-444A
Ultrasonic attenuation peak in steel and aluminum alloy during rotating bending fatigue. 1121-1128A
A model for creep-fatigue interaction in terms of crack-tip stress relaxation. 1761-1775A
- Fatigue life, Composition effects**
The quasi-static and cyclic fatigue fracture behavior of 2014 aluminum alloy metal-matrix composites. 959-974A
- Fatigue limit, Microstructural effects**
Effects of microstructure on the short fatigue crack initiation and propagation characteristics of biomedical α/β titanium alloys. 1949-1958A
- Fatigue strength**
The effect of impact damage on the room-temperature fatigue behavior of γ -TiAl. 1741-1752A
Modeling creep and fatigue of copper alloys. 2491-2502A
- Fatigue strength, Coating effects**
Effects of sulfur on the fatigue and fracture resistance of interfaces between γ -Ni(Cr) and α -Al₂O₃. 1977-1983A
Thermal stability of electroless-nickel/solder interface: B. Interfacial fatigue resistance. 2867-2875A
- Fatigue strength, Deformation effects**
The effect of matrix microstructure on the tensile and fatigue behavior of SiC particle-reinforced 2080 Al matrix composites. 531-540A
- Fatigue strength, Microstructural effects**
Effects of microstructure on the short fatigue crack initiation and propagation characteristics of biomedical α/β titanium alloys. 1949-1958A
- Fatigue strength, Temperature effects**
Fatigue and fracture toughness of a Nb-Ti-Cr-Al-X single-phase alloy at ambient temperature. 1075-1084A
- Fatigue strength, Welding effects**
Characteristics of a pulsed-current, vertical-up gas metal arc weld in steel. 2247-2259A
- Fatigue tests**
Infrared temperature mapping of ULTIMET alloy during high-cycle fatigue tests. 1307-1310A
- Ferrite**
Influence of microstructure on the flow behavior of duplex stainless steels at high temperatures. 1353-1364A
- Ferrite, Alloying effects**
Atom probe field ion microscopy investigation of boron containing martensitic 9% chromium steel. 975-984A
- Ferrite, Diffusion**
The chemical diffusivity of oxygen in liquid iron oxide and a calcium ferrite. 1059-1068B
- Ferrite, Mechanical properties**
Load sharing between austenite and ferrite in a duplex stainless steel during cyclic loading. 1557-1570A
- Ferritic stainless steels, Microstructure**
Substructural changes during hot deformation of a Fe-26Cr ferritic stainless steel. 21-27A
The effect of cooling rate on the microstructures formed during solidification of ferritic steel. 3155-3166A
- Ferritic stainless steels, Welding**
A Bayesian analysis of the influence of neutron irradiation on embrittlement in ferritic submerged arc weld metal. 445-459A
Microstructural characterization and analysis of inclusions in C-Mn steel and weld metals. 615-628A
- Ferritic transformations, Cooling effects**
Microstructural evolution in ultra-low-carbon steel weldments. I. Controlled thermal cycling and continuous cooling transformation diagram of the weld metal. 2145-2153A
- Ferritic transformations, Diffusion effects**
On the mobility of the austenite-ferrite interface in Fe-Co and Fe-Cu. 379-385A
- Ferrous alloys, Corrosion**
The effect of aluminum content on the corrosion behavior of Fe-Al alloys in reducing environments at 700°C. 1805-1817A
- Ferrous alloys, Crystal growth**
Grain-growth-inhibiting effects of primary inclusion particles of ZrO₂ and MgO in Fe-10 mass% Ni alloy. 1213-1223A
- Ferrous alloys, Mechanical properties**
Hydrogen effects on the spall strength and fracture characteristics of amorphous Fe-Si-B alloy at very high strain rates. 1085-1093A
Hydrogen effects on an amorphous Fe-Si-B alloy. 2517-2528A
- Ferrous alloys, Microstructure**
Substructural changes during hot deformation of a Fe-26Cr ferritic stainless steel. 21-27A
- Ferrous alloys, Oxidation**
Formation of pegs during high-temperature oxidation of Fe₃Al containing yttrium. 1685-1687A
- Ferrous alloys, Phase transformations**
Driving force for $\gamma \rightarrow \epsilon$ martensitic transformation and stacking fault energy of γ in Fe-Mn binary system. 355-360A
Alloy design of FeMnSiCrNi shape-memory alloys related to stacking-fault energy. 581-584A
Crystallization of amorphous Fe₈₂P₁₈. 1067-1073A
A model for nonclassical nucleation of solid-solid structural phase transformations. 1321-1331A
Effects of thermal cycling on the kinetics of the $\gamma \rightarrow \epsilon$ martensitic transformation in an Fe-17 wt.% Mn alloy. 2735-2738A
- Ferrous alloys, Powder technology**
Sintering behavior of nanocrystalline γ -Ni-Fe powders. 503-510A
Dilatometry study of the sintering behavior of boron-alloyed Fe-1.5% Mo powder. 1497-1506A
Thermal transformations in mechanically alloyed Fe-Zn-Si materials. 2747-2754A
- Ferrovanadium, Reactions (chemical)**
Equilibrium slag losses in ferrovanadium production. 1091-1097B
- Fiber composites, Casting**
Simulation of metal-matrix composite isothermal infiltration processing. 225-234B
- Fiber composites, Mechanical properties**
Thermal activation of fatigue damage. 63-69A
Reactive infiltration processing and secondary compressive creep of NiAl and NiAl-W composites. 781-792A
Effect of fiber volume fraction on the fracture behavior of Nb-1 wt.% Zr/218W composites at elevated temperatures. 873-887A
Fatigue crack growth resistance of unidirectional fiber-reinforced titanium metal-matrix composites under transverse loading. 2083-2092A
Effect of interfacial debonding and sliding on matrix crack initiation during isothermal fatigue of SCS-6/Ti-15-3 composites. 2637-2645A
- Fiber composites, Microstructure**
Texture and residual strain in two SiC/Ti-6-2-4-2 titanium composites. 889-898A
- Fiber composites, Powder technology**
Mechanisms, models and simulations of metal-coated fiber consolidation. 1271-1282A
- Fiber composites, Thermal properties**
Thermal expansion behavior of silver matrix composites. 291-298A
- Field ion microscopy**
Atom probe field ion microscopy investigation of boron containing martensitic 9% chromium steel. 975-984A
- Filler metal, Materials selection**
Development of a low-melting-point filler metal for brazing aluminum alloys. 2239-2245A
- Filtration**
A mathematical model of aluminum depth filtration with ceramic foam filters. I. Validation for short-term filtration. 491-502B
A mathematical model of aluminum depth filtration with ceramic foam filters. II. Application to long-term filtration. 503-513B
- Finite element method**
The use of the finite-element method to design an optimized tool for the plain-strain punch stretching test. 93-98A
Prediction of cracks in continuously cast steel beam blank through fully coupled analysis of fluid flow, heat transfer, and deformation behavior of a solidifying shell. 225-237A
Equilibrium shape of a molten silicon drop in an electromagnetic levitator in microgravity environment. 327-329B
The effect of matrix microstructure on the tensile and fatigue behavior of SiC particle-reinforced 2080 Al matrix composites. 531-540A
A process model for the heat-affected zone microstructure evolution in duplex stainless steel weldments. II. Application to electron beam welding. 1035-1048A
Modeling of microstructure and residual stress in cast iron calendar rolls. 1201-1211A
A model for prediction of pressure and redistribution of gas-forming elements in multicomponent casting alloys. 1283-1292B
Thermal and grain-structure simulation in a land-based turbine blade directionally solidified with the liquid metal cooling process. 1293-1304B
Thermal analysis of the arc welding process. I. General solutions. 1353-1370B
Analysis of secondary oxide-scale failure at entry into the roll gap. 1483-1490B
Numerical calculation of the electromagnetic expulsive force upon nonmetallic inclusions in an aluminum melt. I. Spherical particles. 1527-1533B
Numerical calculation of the electromagnetic expulsive force upon nonmetallic inclusions in an aluminum melt. II. Cylindrical particles. 1535-1540B
Transient liquid-phase bonding in the Ni-Al-B system. 2835-2847A
Influence of elastic inclusion morphology and matrix hardening behavior on Bauschinger effect in metal matrix composites. 2943-2948A
Effect of computational domain size on the mathematical modeling of transport processes and segregation during direc-

- tional solidification. 3129-3135A
- Flaw detection**
Microstructure-ultrasonic inspectability relationships in Ti6242: signal-to-noise in fine-grain-processed Ti6242. 2119-2125A
Development of a freckle predictor via Rayleigh number method for single-crystal nickel-base superalloy castings. 2545-2557A
- Fluid dynamics**
Modeling the dynamics of magnetic semilevitation melting. 179-189B
- Fluid flow**
Numerical simulation of the flow and the solid transport when tilting a holding furnace. 207-214B
Prediction of cracks in continuously cast steel beam blank through fully coupled analysis of fluid flow, heat transfer, and deformation behavior of a solidifying shell. 225-237A
Two-fluid simulation on the mixed convection flow pattern in a nonisothermal water model of continuous casting tundish. 867-875B
- Fluxes, Reactions (chemical)**
The effects of alkaline earth metal ions and halogen ions on the chromium oxide activities in alkaline earth metal oxide-halide-Cr₂O₃ system fluxes. 469-475B
Phase diagram cuspidine (3CaO·2SiO₂·CaF₂)-CaF₂. 1273-1281B
- Foamed metals, Powder technology**
Preparation of high porosity metal foams. 1345-1352B
- Foaming**
The surface tensions and foaming behavior of melts in the system CaO-FeO-SiO₂. 921-925B
Some observations on the draining of CaO-SiO₂-Al₂O₃ slag bubble films. 1105-1115B
- Forgeability**
Plastic flow behavior during the forging of a 6061 Al/10 vol% Al₂O₃(p) composite. 1310-1313A
- Formability, Composition effects**
Microstructure and formability of ZnNi alloy electrodeposited sheet steel. 475-485A
Strength and formability of ultra-low-carbon Ti-IF steels. 1305-1307A
- Formability, Processing effects**
Effects of strain rate and anisotropy on the tensile deformation properties of extruded AlZnMg alloys. 669-678A
- Forming**
Dynamic materials testing, texture, and yield-surface calculation of an automotive sheet steel. 2439-2448A
- Forming, Composition effects**
Strength and formability of ultra-low-carbon Ti-IF steels. 1305-1307A
- Foundry practice**
Fluid flow and inclusion removal in continuous casting tundish. 253-266B
Prevention of macrodefects in squeeze casting of an Al-7 wt.% Si alloy. 297-305B
The effect of a uniform direct current magnetic field on the stability of a stratified liquid flux/molten steel system. 317-326B
A computational model for defect prediction in shape castings based on the interaction of free surface flow, heat transfer, and solidification phenomena. 515-527B
A new criterion for internal crack formation in continuously cast steels. 779-794B
Freckle formation and freckle criterion in superalloy castings. 801-811B
Depth of oscillation marks forming in continuous casting of steel. 813-826B
Aluminum volatilization and inclusion removal in the electron beam cold hearth melting of Ti alloys. 845-854B
Numerical studies of the motion of spheroidal particles flowing with liquid metals through an electric sensing zone. 855-866B
Erratum: "Numerical studies of the motion of spheroidal particles flowing with liquid metals through an electric sensing zone". 1143B
Alpha case thickness modeling in investment castings. 1419-1427B
Two-phase modeling of mushy zone parameters associated with hot tearing. 1461-1472A
Correlation between unsteady-state solidification conditions, dendrite spacings, and mechanical properties of Al-Cu alloys. 3167-3178A
- Fractography**
Damage leading to ductile fracture under high strain-rate conditions. 831-844A
- Fracture mechanics**
Fatigue crack path prediction in Udimet 720 nickel-based alloy single crystals. 109-123A
- Fracture strength**
Hydrogen effects on the spall strength and fracture characteristics of amorphous Fe-Si-B alloy at very high strain rates. 1085-1093A
- Fracture strength, Composition effects**
Constitutive properties of hard-alpha titanium. 3029-3040A
- Fracture strength, Microstructural effects**
The fracture resistance of a binary TiAl alloy. 71-80A
The mechanism of brittle fracture in a microalloyed steel. I. Inclusion-induced cleavage. 641-652A
The mechanism of brittle fracture in a microalloyed steel. II. Mechanistic modeling. 653-667A
The effect of processing and microstructure development on the slip and fracture behavior of the 2.1 wt.% Li AF/C-489 and 1.8 wt.% Li AF/C-458 Al-Li-C-X alloys. 1965-1976A
- Fracture toughness**
An investigation of dynamic failure in 2.3Ni-1.3Cr-0.17C steel. 1147-1154A
- Fracture toughness, Alloying effects**
The influence of Mg on creep properties and fracture behaviors of Mar-M247 superalloy under 1255 K/200 MPa. 1365-1373A
A comparison study of microstructure and mechanical properties of Ti-24Al-14Nb-3V-0.5Mo with and without Si. 2205-2217A
- Fracture toughness, Coating effects**
Growth of a Au-Ni-Sn intermetallic compound on the solder-substrate interface after aging. 798-800A
Correlation of microstructure with the wear resistance and fracture toughness of hardfacing alloys reinforced with complex carbides. 3041-3052A
- Fracture toughness, Composition effects**
An investigation of the effects of ductile-layer thickness on the fracture behavior of nickel aluminide microlaminates. 1385-1399A
High-temperature fracture and fatigue-crack growth behavior of an XD gamma-based titanium aluminide intermetallic alloy. 1413-1423A
Effect of particle-size distribution on the properties of high-volume-fraction SiC_p-Al-based composites. 2351-2359A
- Fracture toughness, Heating effects**
Deformation and fracture of a particle-reinforced aluminum alloy composite. I. Experiments. 921-936A
Deformation and fracture of a particle-reinforced aluminum alloy composite. II. Modeling. 937-950A
- Fracture toughness, High temperature effects**
Dynamic fracture toughness of a Ti-45Al-1.6Mn alloy at high temperature. 3053-3061A
- Fracture toughness, Microstructural effects**
The fracture resistance of a binary TiAl alloy. 71-80A
Correlation of the microstructure and fracture toughness of the heat-affected zones of an SA 508 steel. 1107-1119A
Impact fracture toughness of porous iron and high-strength steels. 1443-1451A
Microstructural effects on fracture toughness in AA7010 plate. 2503-2515A
- Fracture toughness, Temperature effects**
Fatigue and fracture toughness of a Nb-Ti-Cr-Al-X single-phase alloy at ambient temperature. 1075-1084A
- Fracture toughness, Welding effects**
Fracture mechanism and toughness of the welding heat-affected zone in structural steel under static and dynamic loading. 2785-2791A
- Fracturing**
The role of plasticity in bimaterial fracture with ductile interlayers. 863-872A
- Fracturing, Composition effects**
Effect of fiber volume fraction on the fracture behavior of Nb-1 wt.% Zr/218W composites at elevated temperatures. 873-887A
Constitutive properties of hard-alpha titanium. 3029-3040A
- Fracturing, Heating effects**
Deformation and fracture of a particle-reinforced aluminum alloy composite. I. Experiments. 921-936A
Deformation and fracture of a particle-reinforced aluminum alloy composite. II. Modeling. 937-950A
- Fracturing, Microstructural effects**
Anisotropic behavior and rupture of hydrided Zircaloy-4 sheets. 679-690A
- Fracturing, Welding effects**
Creep deformation and fracture behavior of types 316 and 316L(N) stainless steels and their weld metals. 1175-1185A
- Friction welding**
Friction-stir welding effects on microstructure and fatigue of aluminum alloy 7050-T7451. 2181-2192A
- Frictional wear**
Identification of rolling-sliding damage mechanisms in porous alloys. 3091-3099A
- Frictional wear, Processing effects**
Tribological properties of centrifugally cast copper alloy-graphite particle composite. 1283-1293A
- Functionally gradient materials, Electrical properties**
Characterization of Mo-SiO₂ functionally graded materials. 299-308A
- Functionally gradient materials, Extrusion**
Near-net-shape forming of Al-Al₃Ni functionally graded material over eutectic melting temperature. 2627-2636A
- Functionally gradient materials, Powder technology**
Design and fabrication of W-Mo-Ti-TiAl-Al system functionally graded material. 2369-2376A
- Fused salts, Electrochemistry**
Fundamental theories and concepts for predicting thermodynamic properties of high temperature ionic and metallic liquid solutions and vapor molecules. 579-586B
CoCl₂: unique in all of molten salt? 597-602B
The power of thermodynamic modeling: examples from molten halide mixtures. 641-650B
The modified quasicchemical model I—binary solutions. 651-659B
- Gadolinium compounds, Electrochemistry**
Thermodynamic and nonstoichiometric behavior of promising Hi-Tc cuprate systems via electromotive force measurements: a short review. 661-666B
- Galvanized steels, Coating**
Application of the phase-field method to the solidification of hot-dipped galvanized coatings. 487-495A
- Gas metal arc welding**
Characteristics of a pulsed-current, vertical-up gas metal arc weld in steel. 2247-2259A
- Gas tungsten arc welding**
Numerical modeling of enhanced nitrogen dissolution during gas tungsten arc welding. 1371-1385B
Mathematical modeling of the dynamic behavior of gas tungsten arc weld pools. 1465-1473B
Weld metal ductility in aluminum tailor welded blanks. 2755-2763A
- Germanium base alloys, Phase transformations**

- Ideal and cooperative bond-lattice representations of excitations in glass-forming liquids: excitation profiles, fragilities, and phase transitions. 587-596B
- Gold, Coatings**
Growth of a Au-Ni-Sn intermetallic compound on the solder-substrate interface after aging. 798-800A
- Gold, Extraction**
Selective arsenic-fixing roast of refractory gold concentrate. 1163-1168B
- Gold, Phases (state of matter)**
Liquidus temperature determination in multicomponent alloys by thermal analysis. 497-501A
- Gold base alloys, Phase transformations**
Displacive transformations in Au-18 wt.% Cu-6 wt.% Al. 1917-1923A
- Grain boundaries**
Correlation between former alpha boundary growth kinetics and superplastic flow in Zn-22% Al. 163-172A
- Grain boundaries, Heating effects**
Grain boundary faceting and abnormal grain growth in nickel. 985-994A
- Grain boundaries, Processing effects**
Directional and single-crystal solidification of Ni-base superalloys. II. Coincidence site lattice character of grain boundaries. 2887-2893A
- Grain boundary migration**
Island grains of low misorientation angles formed during abnormal grain growth in Cu. 1489-1491A
- Grain boundary sliding**
 δ/γ interface boundary sliding as a mechanism of strain accommodation during hot deformation in a duplex stainless steel. Evolution of texture and grain misorientation in an Al-Mg alloy exhibiting low-temperature superplasticity. 2169-2180A
- Grain growth**
Island grains of low misorientation angles formed during abnormal grain growth in Cu. Correlation between unsteady-state solidification conditions, dendrite spacings, and mechanical properties of Al-Cu alloys. 3167-3178A
- Grain growth, Alloying effects**
Effects of boron doping on the grain-growth kinetics and mechanical properties of γ/γ' nickel-aluminum alloys. 3179-3186A
- Grain growth, Anisotropy**
Anisotropic grain growth based on the atomic adsorption model in WC-25% Co alloy. 1925-1935A
- Grain growth, Heating effects**
Grain boundary faceting and abnormal grain growth in nickel. 985-994A
- Grain growth, Impurity effects**
Grain-growth-inhibiting effects of primary inclusion particles of ZrO_2 and MgO in Fe-10 mass% Ni alloy. 1213-1223A
- Grain growth, Welding effects**
Three-dimensional Monte Carlo simulation of grain growth in the heat-affected zone of a 2.25Cr-1Mo steel weld. 529-536B
- Grain orientation**
Surface relief of α' martensite in a Ti-Mo alloy. Evolution of texture and grain misorientation in an Al-Mg alloy exhibiting low-temperature superplasticity. 2169-2180A
- Grain refinement, Alloying effects**
The role of solute in grain refinement of magnesium. 2895-2906A
- Grain refinement, Deformation effects**
Equal-channel angular pressing of commercial aluminum alloys: grain refinement, thermal stability and tensile properties. 691-701A
- Grain refinement, Deformation effects**
Microstructural development and austempering kinetics of ductile iron during thermomechanical processing. 2575-2585A
- Grain refinement, Vibration effects**
Effects of the intensity and frequency of electromagnetic vibrations on the microstructural refinement of hypoeutectic Al-Si alloys. 755-762A
- Grain size**
Solidification parameters during the columnar-to-equiaxed transition in lead-tin alloys. 1611-1625A
- Grain size, Deformation effects**
The effect of processing and microstructure development on the slip and fracture behavior of the 2.1 wt.% Li AF/C-489 and 1.8 wt.% Li AF/C-458 Al-Li-C-X alloys. 1965-1976A
- Grain size, Deformation effects**
Mathematical modeling of the hot strip rolling of microalloyed Nb, multiply alloyed Cr-Mo, and plain C-Mn steels. 511-530A
- Grain size, Deformation effects**
Equal-channel angular pressing of commercial aluminum alloys: grain refinement, thermal stability and tensile properties. 691-701A
- Grain size, Heating effects**
Insight into the microstructural characterization of ferritic steel using micromagnetic parameters. 1053-1065A
- Grain size, Processing effects**
The role of dispersed particles in strengthening and fracture mechanisms in a Mo-ZrC alloy processed by mechanical alloying. 715-721A
- Grain size, Welding effects**
Three-dimensional Monte Carlo simulation of grain growth in the heat-affected zone of a 2.25Cr-1Mo steel weld. 529-536B
- Grain structure**
Thermal and grain-structure simulation in a land-based turbine blade directionally solidified with the liquid metal cooling process. 1293-1304B
- Grain structure**
Island grains of low misorientation angles formed during abnormal grain growth in Cu. 1489-1491A
- Grain structure, Composition effects**
Microstructure and formability of ZnNi alloy electrodeposited sheet steel. 475-485A
- Grain structure, Heating effects**
Grain boundary faceting and abnormal grain growth in nickel. 985-994A
- Grain structure, Processing effects**
Simulation of percolation structure of grain bonding in liquid-phase sintering by three-dimensional grain structure reconstruction. 3187-3193A
- Grain structure, Vibration effects**
Effects of the intensity and frequency of electromagnetic vibrations on the microstructural refinement of hypoeutectic Al-Si alloys. 755-762A
- Graphite, Composite materials**
Particulate penetration into solid droplets. Tribological properties of centrifugally cast copper alloy-graphite particle composite. Nucleation on ceramic particles in cast metal-matrix composites. 387-396A
1283-1293A
1295-1304A
- Graphite, Oxidation**
Kinetics of oxidation of carbonaceous materials by CO_2 and H_2O between 1300° and 1500°C. 43-54B
- Graphite, Reactions (chemical)**
Dissolution rates of coals and graphite in Fe-C-S melts in direct ironmaking: influence of melt carbon and sulfur on carbon dissolution. 243-251B
- Graphitization, Deformation effects**
The effect of rolling on graphitization characteristics of strip cast Fe-C-Si white cast iron. 275-281A
- Gray iron, Crystal growth**
A two-dimensional model for the description of the columnar-to-equiaxed transition in competing gray and white iron eutectics and its application to calendar rolls. 2059-2068A
- Guinier Preston zone, Alloying effects**
Precipitation processes in Al-Cu-Mg alloys microalloyed with Si. 2721-2733A
- Guinier Preston zone, Composition effects**
Effects of Cu content and preaging on precipitation characteristics in aluminum alloy 6022. 361-371A
- Guinier Preston zone, Heating effects**
Differential scanning calorimetry and electron diffraction investigation on low-temperature aging in Al-Zn-Mg alloys. Spontaneous deformation during aging under stress in a copper-beryllium alloy. 339-348A
2765-2771A
- Hall Heroult process**
Solutions of iron oxides in molten cryolite. A new approach to numerical simulation of melt flows and interface instability in Hall-Heroult cells. Some generalities in the analyses of equilibria in ionic solutions. 609-613B
1541-1550B
2105-2118A
- Hardening**
Mechanical behavior and damage kinetics in nodular cast iron. II. Hardening and damage. 3075-3085A
- Hardening, High temperature effects**
Stress-strain response of a cast 319-T6 aluminum under thermomechanical loading. 139-151A
- Hardness, Alloying effects**
Precipitation processes in Al-Cu-Mg alloys microalloyed with Si. Effects of boron doping on the grain-growth kinetics and mechanical properties of γ/γ' nickel-aluminum alloys. 2721-2733A
3179-3186A
- Hardness, Coating effects**
Surface amorphous and crystalline microstructure by alloying zirconium using Nd:YAG pulsed laser. 3123-3127A
- Hardness, Composition effects**
Characterization of Mo-SiO₂ functionally graded materials. Microstructure and formability of ZnNi alloy electrodeposited sheet steel. Synthesis of MoSi₂-TiSi₂ pseudobinary alloys by reactive sintering. 299-308A
475-485A
747-753A
- Hardness, Deformation effects**
Load sharing between austenite and ferrite in a duplex stainless steel during cyclic loading. 1557-1570A
- Hardness, Microstructural effects**
Correlation of the microstructure and fracture toughness of the heat-affected zones of an SA 508 steel. 1107-1119A
- Hardness, Welding effects**
Dispersoid-free zones in the heat-affected zone of aluminum alloy welds. 1453-1459A
- Heat, Deformation effects**
Heat generation during the fatigue of a cellular Al alloy. 1129-1136A
- Heat affected zone, Mechanical properties**
The mechanism of brittle fracture in a microalloyed steel. I. Inclusion-induced cleavage. Correlation of the microstructure and fracture toughness of the heat-affected zones of an SA 508 steel. Fracture mechanism and toughness of the welding heat-affected zone in structural steel under static and dynamic loading. Relation between microstructure, composition, and hot cracking in Ti-stabilized austenitic stainless steel weldments. 641-652A
1107-1119A
2785-2791A
3109-3122A
- Heat affected zone, Microstructure**
Three-dimensional Monte Carlo simulation of grain growth in the heat-affected zone of a 2.25Cr-1Mo steel weld. Dispersoid-free zones in the heat-affected zone of aluminum 529-536B

- alloy welds. 1453-1459A
- Heat affected zone, Oxidation**
Relevance of high-temperature oxidation in life assessment and microstructural degradation of Cr-Mo steel weldments. 3101-3108A
- Heat of mixing**
Enthalpy of mixing of liquid Ni-Zr and Cu-Ni-Zr alloys. 277-284B
- Heat transfer**
Physical and mathematical models of steel flow and heat transfer in a tundish heated by plasma. 63-74B
Finding boundary conditions: a coupling strategy for the modeling of metal casting processes. I. Experimental study and correlation development. 75-86B
Finding boundary conditions: a coupling strategy for the modeling of metal casting processes. II. Numerical study and analysis. 87-96B
Prediction of cracks in continuously cast steel beam blank through fully coupled analysis of fluid flow, heat transfer, and deformation behavior of a solidifying shell. 225-237A
A model of the interfacial heat-transfer coefficient during unidirectional solidification of an aluminum alloy. 285-295B
A computational model for defect prediction in shape castings based on the interaction of free surface flow, heat transfer, and solidification phenomena. 515-527B
Two-fluid simulation on the mixed convection flow pattern in a nonisothermal water model of continuous casting tundish. 867-875B
Mechanisms of initial melt/substrate heat transfer pertinent to strip casting. 1023-1030B
Measurements, simulations, and analyses of instantaneous heat fluxes from solidifying steels to the surfaces of twin roll casters and of aluminum to plasma-coated metal substrates. 1031-1047B
Interfacial heat transfer and nucleation of steel on metallic substrates. 1081-1089B
- Heat transmission**
Modeling of interdendritic strain and macrosegregation for dendritic solidification processes. I. Theory and experiments. 331-343B
Modeling of interdendritic strain and macrosegregation for dendritic solidification processes. II. Computation of interdendritic strain and segregation fields in steel ingots. 345-355B
- High carbon steels, Casting**
Modeling of interdendritic strain and macrosegregation for dendritic solidification processes. I. Theory and experiments. 331-343B
Modeling of interdendritic strain and macrosegregation for dendritic solidification processes. II. Computation of interdendritic strain and segregation fields in steel ingots. 345-355B
- High carbon steels, Heat treatment**
Microstructural and compositional evolution of compound layers during gaseous nitrocarburizing. 195-211A
Erratum: Microstructural and compositional evolution of compound layers during gaseous nitrocarburizing. 801A
- High carbon steels, Mechanical properties**
Identification of rolling-sliding damage mechanisms in porous alloys. 3091-3099A
- High cycle fatigue**
Infrared temperature mapping of ULTIMET alloy during high-cycle fatigue tests. 1307-1310A
Role of foreign-object damage on thresholds for high-cycle fatigue in Ti-6Al-4V. 1571-1583A
- High cycle fatigue, Temperature effects**
Thermal activation of fatigue damage. 63-69A
- High speed tool steels, Claddings**
Microstructural evolution during laser cladding of M2 high-speed steel. 2615-2625A
- High speed tool steels, Phases (state of matter)**
Phase analysis of two steel work rolls using Mössbauer spectroscopy. 793-798A
- High strength low alloy steels, Coatings**
On the evolution of porosity in spray-deposited tool steels. 723-733A
- High strength low alloy steels, Mechanical properties**
Influence of alloying elements on the strain rate and temperature dependence of the flow stress of steels. 825-830A
The effect of microstructural banding on failure initiation of HY-100 steel. 995-1005A
Residual strains in HY100 polycrystals: comparisons of experiments and simulations. 1543-1555A
The mechanical threshold stress constitutive-strength model description of HY-100 steel. 1985-1996A
Analysis and prevention of yield strength drop during spiral piping of two high-strength API-X70 steels. 2669-2674A
- High strength low alloy steels, Rolling**
Microstructural model for hot strip rolling of high-strength low-alloy steels. 1247-1259A
- High strength steels, Coating**
Influence of annealing conditions on the galvanizability and galvannealing properties of TiNb interstitial-free steels, strengthened with phosphorous and manganese. 1225-1232A
- High strength steels, Heat treatment**
Dynamic bake hardening of interstitial-free steels. 1375-1384A
- High strength steels, Mechanical properties**
Influence of alloying elements on the strain rate and temperature dependence of the flow stress of steels. 825-830A
Simulation of shear plugging through thin plates using the GRIM Eulerian hydrocode. 853-860A
An investigation of dynamic failure in 2.3Ni-1.3Cr-0.17C steel. 1147-1154A
Impact fracture toughness of porous iron and high-strength steels. 1443-1451A
- High temperature**
Selective oxidation and internal nitridation during high-temperature exposure of single-crystalline nickel-base superalloys. 47-56A
Effect of fiber volume fraction on the fracture behavior of Nb-1 wt.% Zr/218W composites at elevated temperatures. 873-887A
Influence of microstructure on the flow behavior of duplex stainless steels at high temperatures. 1353-1364A
- Holding furnaces**
Numerical simulation of the flow and the solid transport when tilting a holding furnace. 207-214B
- Hot dip aluminizing**
Dynamic reactive wetting and its role in hot dip coating of steel sheet with an Al-Zn-Si alloy. 1069-1079B
- Hot dip galvanizing**
Application of the phase-field method to the solidification of hot-dipped galvanized coatings. 487-495A
- Hot dip galvanizing, Heating effects**
Influence of annealing conditions on the galvanizability and galvannealing properties of TiNb interstitial-free steels, strengthened with phosphorous and manganese. 1225-1232A
- Hot extrusion**
Hot deformation mechanisms in a powder metallurgy nickel-base superalloy IN 625. 2317-2325A
- Hot isostatic pressing**
Effect of fiber volume fraction on the fracture behavior of Nb-1 wt.% Zr/218W composites at elevated temperatures. 873-887A
Mechanisms, models and simulations of metal-coated fiber consolidation. 1271-1282A
Microstructural evolution in wire-drawn Ti-22Al-26Nb powder. 2931-2941A
Fundamental aspects of hot isostatic pressing: an overview. 2981-3000A
- Hot pressing**
Processing and microstructural characterization of Al-Cu alloys produced from rapidly solidified powders. 249-260A
- Hot rolling**
The effect of rolling on graphitization characteristics of strip cast Fe-C-Si white cast iron. 275-281A
Mathematical modeling of the hot strip rolling of microalloyed Nb, multiply alloyed Cr-Mo, and plain C-Mn steels. 511-530A
Microstructural model for hot strip rolling of high-strength low-alloy steels. 1247-1259A
Analysis of secondary oxide-scale failure at entry into the roll gap. 1483-1490B
Evolution of texture in the β (B2) phase of a two phase titanium aluminide intermetallic alloy Ti-24Al-11Nb. 2339-2350A
- Hot spraying**
Synthesis of nanostructured WC-12%Co coating using mechanical milling and high velocity oxygen fuel thermal spraying. 541-553A
Synthesis of nanostructured Cr_3C_2 -25(Ni20Cr) coatings. 555-564A
Monosize droplet deposition as a means to investigate droplet behavior during spray deposition. 1333-1344B
- Hot strip mills**
Mathematical modeling of the hot strip rolling of microalloyed Nb, multiply alloyed Cr-Mo, and plain C-Mn steels. 511-530A
- Hot workability**
Interpretation of microstructural evolution using dynamic materials modeling. 2973-2974A
- Hot working**
Substructural changes during hot deformation of a Fe-26Cr ferritic stainless steel. 21-27A
 δ/γ interface boundary sliding as a mechanism of strain accommodation during hot deformation in a duplex stainless steel. 1671-1677A
Interpretation of microstructural evolution using dynamic materials modeling. 2973-2974A
- Hot working, Composition effects**
Effect of volume fraction of SiC_0 reinforcement on the processing maps for 2124 Al matrix composites. 629-639A
- Hydrides**
Anisotropic behavior and rupture of hydrided Zircaloy-4 sheets. 679-690A
- Hydrides, Crystal growth**
The prediction of the hydriding thermodynamics of Pd-Rh-Co ternary alloys. 667-673B
- Hydrogen, Diffusion**
Hydrogen trapping models in steel. 1475-1482B
Hydrogen diffusion coefficients in the titanium alloys IMI 834, Ti 10-2-3, Ti 21 S, and Alloy C. 1507-1517A
- Hydrogen, Reactions (chemical)**
Interfacial kinetics of hydrogen with liquid slag containing iron oxide. 945-955B
- Hydrogen, Sorption**
The identification of hydrogen trapping states in an Al-Li-Cu-Zr alloy using thermal desorption spectroscopy. 179-193A
- Hydrogen embrittlement**
On methane generation and decarburization in low-alloy Cr-Mo steels during hydrogen attack. 125-137A
Hydrogen effects on the spall strength and fracture characteristics of amorphous Fe-Si-B alloy at very high strain rates. 1085-1093A
Environmentally enhanced deformation of ultra-high-purity Ni-16Cr-9Fe alloys. 2383-2388A
Hydrogen effects on an amorphous Fe-Si-B alloy. 2517-2526A
- Hydrogen embrittlement, Composition effects**
Hydrogen diffusion coefficients in the titanium alloys IMI 834, Ti 10-2-3, Ti 21 S, and Alloy C. 1507-1517A
- Hydrogen embrittlement, Heating effects**
Part II. Metallurgical factors governing the H-assisted intergranular cracking of peak-aged Ti-3Al-8V-6Cr-4Mo-4Zr (Beta-C). 81-92A
- Hydrogen embrittlement, Temperature effects**

- Stress corrosion cracking mechanisms of Alloy 600 polycrystals and single crystals in primary water—Influence of hydrogen. 2025-2036A
- Hydrogen storage**
The prediction of the hydriding thermodynamics of Pd-Rh-Co ternary alloys. 667-673B
- Hydrometallurgy**
Preparation of Nd(III) carbonate by precipitation stripping of Nd(III)-loaded VA10. 5-13B
The electrochemical property of acetylene black suspension solution with ozone bubbling and its effects on copper dissolution. 235-241B
Pore transport-controlled shrinking-core systems involving diffusion, migration, and homogeneous reactions. I. Formulation of model and rate equation for PbSO_4 -carbonate system. 683-691B
Pore transport-controlled shrinking-core systems involving diffusion, migration, and homogeneous reactions. II. Application of model for PbSO_4 -carbon system to experimental data. Selective arsenic-fixing roast of refractory gold concentrate. Mixed solvent systems for the extraction and stripping of iron(III) from concentrated acid chloride solutions. Characterization of scales obtained during continuous nickel latent pilot-plant leaching. 1175-1186B
- Hysteresis**
Heat generation during the fatigue of a cellular Al alloy. Displacive transformations in Au-18 wt.% Cu-6 wt.% Al. 1129-1136A
1917-1923A
- Impact**
Simulation of shear plugging through thin plates using the GRIM Eulerian hydrocode. Role of foreign-object damage on thresholds for high-cycle fatigue in Ti-6Al-4V. 853-860A
1571-1583A
- Impact strength**
The effect of impact damage on the room-temperature fatigue behavior of γ -TiAl. 1741-1752A
- Impact strength, Composition effects**
Interfacial modification and impact properties of Nb/MoSi₂ laminate composites by the addition of ZrO₂, NbSi₂, and SiC particles. 2075-2081A
- Impact strength, Microstructural effects**
Impact fracture toughness of porous iron and high-strength steels. An investigation of the effect of fatigue deformation on the residual mechanical properties of Ti-6Al-4V ELI. 1443-1451A
1937-1948A
- Impact strength, Radiation effects**
A Bayesian analysis of the influence of neutron irradiation on embrittlement in ferritic submerged arc weld metal. 445-459A
- Impact strength, Welding effects**
Characteristics of a pulsed-current, vertical-up gas metal arc weld in steel. 2247-2259A
- Inclusions**
On the detection and selective separation of inclusions in liquid metal cleanliness analyzer (LIMCA) systems. The interactive role of inclusions and SiC reinforcement on the high-cycle fatigue resistance of particle reinforced metal matrix composites. 767-777B
951-957A
- Induction melting**
Evaporation behavior of aluminum during the cold crucible induction skull melting of titanium aluminum alloys. 837-844B
- Infiltration**
Simulation of metal-matrix composite isothermal infiltration processing. On the infiltration behavior of Al, Al-Li, and Mg melts through SiC_f bed. Reactive infiltration processing and secondary compressive creep of NiAl and NiAl-W composites. Porosity nucleation in metal-matrix composites. 225-234B
319-325A
781-792A
2069-2074A
- Infrared analysis**
Infrared temperature mapping of ULTIMET alloy during high-cycle fatigue tests. 1307-1310A
- Ingot casting**
Modeling of interdendritic strain and macrosegregation for dendritic solidification processes. I. Theory and experiments. Modeling of interdendritic strain and macrosegregation for dendritic solidification processes. II. Computation of interdendritic strain and segregation fields in steel ingots. Determination of thermophysical properties and boundary conditions of direct chill-cast aluminum alloys using inverse methods. 331-343B
345-355B
1627-1634A
- Ingot, Crystal growth**
Modeling of interdendritic strain and macrosegregation for dendritic solidification processes. I. Theory and experiments. Modeling of interdendritic strain and macrosegregation for dendritic solidification processes. II. Computation of interdendritic strain and segregation fields in steel ingots. 331-343B
345-355B
- Ingot, Melting**
Modeling the dynamics of magnetic semilevitation melting. 179-189B
- Injection**
Nitrogen alloying of carbon and stainless steels by gas injection. 905-912B
- Injection molding**
Length change and deformation of powder injection-molded compacts during solvent debinding. Simulation of polymer removal from a powder injection molding compact by thermal debinding. 1473-1478A
2597-2606A
- Interdendritic structure**
Modeling of interdendritic strain and macrosegregation for dendritic solidification processes. I. Theory and experiments. Modeling of interdendritic strain and macrosegregation for dendritic solidification processes. II. Computation of interdendritic strain and segregation fields in steel ingots. 331-343B
345-355B
- Interface reactions**
Kinetics of manganese ore reduction by carbon monoxide. Interfacial kinetics of hydrogen with liquid slag containing iron oxide. Dynamic and equilibrium interfacial phenomena in liquid steel-slag systems. Interfacial phenomena in some slag-metal reactions. Rate of interfacial reaction between liquid iron oxide and CO-CO₂. Influence of ash on mass transfer and interfacial reaction between natural graphite and liquid iron. In situ observations of inclusions at the (Mn,Si)-killed steel/CaO-Al₂O₃ interface. An experimental investigation on the kinetics of solute driven remelting. 477-490B
945-955B
957-971B
973-980B
1049-1057B
1099-1104B
1135-1139B
2713-2720A
- Interface reactions, Coating effects**
Thermal stability of electroless-nickel/solder interface: A. Interfacial chemistry and microstructure. 2857-2866A
- Interface reactions, Composition effects**
Interfacial modification and impact properties of Nb/MoSi₂ laminate composites by the addition of ZrO₂, NbSi₂, and SiC particles. Modification of the interface in SiC/Al composites. 2075-2081A
2361-2368A
- Intergranular corrosion, High temperature effects**
Grain-boundary chemistry and intergranular corrosion in alloy 825. 1163-1173A
- Intergranular fracture, Alloying effects**
Effects of boron doping on the grain-growth kinetics and mechanical properties of γ/γ' nickel-aluminum alloys. 3179-3186A
- Intergranular fracture, Heating effects**
Part II. Metallurgical factors governing the H-assisted intergranular cracking of peak-aged Ti-3Al-8V-6Cr-4Mo-4Zr (Beta-C). 81-92A
- Interlayers, Bonding**
The role of plasticity in bimaterial fracture with ductile interlayers. 863-872A
- Intermetallic phases**
The interactive role of inclusions and SiC reinforcement on the high-cycle fatigue resistance of particle reinforced metal matrix composites. Examination of solidification pathways and the liquidus surface in the Nb-Ti-Al system. 951-957A
1305-1321B
- Intermetallic phases, Crystal growth**
Effect of increased growth velocity on the growth temperature of the Al-Al₃Cu eutectic. Neutron diffraction and phase evolution of the mechanically alloyed intermetallic compound ξ -FeZn₁₃. Thermal transformations in mechanically alloyed Fe-Zn-Si materials. Transient liquid-phase bonding in the Ni-Al-B system. Coarsening of intermetallic or compound precipitates in binary systems. 327-328A
2739-2745A
2747-2754A
2835-2847A
3195-3197A
- Intermetallics, Mechanical properties**
Experimental studies on tribological properties of pseudoelastic TiNi alloy with comparison to stainless steel 304. 2773-2783A
- Intermetallics, Phase transformations**
Influence of aging on transformation characteristics in shape memory CuZnAl alloys. Crystallization of amorphous Fe₈₂P₁₈. Experimental investigation and thermodynamic calculation of the Ti-Ni-Cu shape memory alloys. 349-354A
1067-1073A
2423-2430A
- Internal oxidation, Welding effects**
Relevance of high-temperature oxidation in life assessment and microstructural degradation of Cr-Mo steel weldments. 3101-3108A
- Interstitial free steels, Coating**
Influence of annealing conditions on the galvanizability and galvannealing properties of TiNb interstitial-free steels, strengthened with phosphorous and manganese. 1225-1232A
- Interstitial free steels, Heat treatment**
Dynamic bake hardening of interstitial-free steels. 1375-1384A
- Interstitial free steels, Metal working**
Strength and formability of ultra-low-carbon Ti-IF steels. 1305-1307A
- Interstitial free steels, Solubility**
Argon solubility in liquid steel. 913-919B
- Interstitial impurities**
The influence of crystallographic texture and interstitial impurities on the mechanical behavior of zirconium. 1997-2003A
- Investment casting**
Alpha case thickness modeling in investment castings. 1419-1427B
- Investment castings, Diffusion**
Alpha case thickness modeling in investment castings. 1419-1427B
- Ion nitriding**
Study of microstructure of low-temperature plasma-nitrided AISI 304 stainless steel. 1193-1199A
- Ionic conductivity**
The ionic properties of CaSiO₃ melt. 1241-1245B
- Iridium base alloys, Mechanical properties**
Design of quaternary Ir-Nb-Ni-Al refractory superalloys. 173-178A
- Iron, Binary systems**
Driving force for $\gamma \rightarrow \epsilon$ martensitic transformation and stacking fault energy of γ in Fe-Mn binary system. 355-360A

- On the mobility of the austenite-ferrite interface in Fe-Co and Fe-Cu. 379-385A
- A model for nonclassical nucleation of solid-solid structural phase transformations. 1321-1331A
- Iron, Diffusion**
- A Scheil-Gulliver model with back-diffusion applied to the microsegregation of chromium in Fe-Cr-C alloys. 1682-1684A
- Iron, Extraction**
- Recent advances in the fundamentals of the kinetics of steel-making reactions. 891-898B
- Mixed solvent systems for the extraction and stripping of iron(III) from concentrated acid chloride solutions. 1169-1174B
- Experimental study of phase equilibria in the systems Fe-Zn-O and Fe-Zn-Si-O at metallic iron saturation. 1195-1201B
- Iron, Mechanical properties**
- Impact fracture toughness of porous iron and high-strength steels. 1443-1451A
- Identification of rolling-sliding damage mechanisms in porous alloys. 3091-3099A
- Iron, Powder technology**
- Sintering behavior of nanocrystalline γ -Ni-Fe powders. 503-510A
- Preparation of high porosity metal foams. 1345-1352B
- Length change and deformation of powder injection-molded compacts during solvent debinding. 1473-1478A
- Improved densification of carbonyl iron compacts by the addition of fine alumina powders. 1645-1652A
- Iron, Reactions (chemical)**
- Dissolution rates of coals and graphite in Fe-C-S melts in direct ironmaking: influence of melt carbon and sulfur on carbon dissolution. 243-251B
- Thermodynamics of surfaces and adsorption in the Fe-C-S-O system. 267-276B
- Iron, Refining**
- X-ray fluoroscopy observations of bubble formation and separation at a metal-slag interface. 537-540B
- Effects of aluminum, silicon, and boron on the dissolution rate of nitrogen into molten iron. 899-904B
- Iron, Solubility**
- Argon solubility in molten iron. 216-218B
- Iron, Welding**
- Numerical modeling of enhanced nitrogen dissolution during gas tungsten arc welding. 1371-1385B
- Unsteady Marangoni flow in a molten pool when welding dissimilar metals. 1387-1403B
- Iron and steel making**
- Kinetics of oxidation of carbonaceous materials by CO_2 and H_2O between 1300° and 1500°C. 43-54B
- Physical and mathematical models of steel flow and heat transfer in a tundish heated by plasma. 63-74B
- Thermodynamics of surfaces and adsorption in the Fe-C-S-O system. 267-276B
- The effect of water vapor on mold slag crystallization. 403-406B
- Kinetics of Al_2O_3 dissolution in $\text{CaO-MgO-SiO}_2\text{-Al}_2\text{O}_3$ slags: in situ observations and analysis. 406-410B
- Steel at the millennium. 561-575B
- Solid-state amperometric sensor for the in-situ monitoring of slag composition and transport properties. 733-753B
- Recent advances in the fundamentals of the kinetics of steel-making reactions. 891-898B
- The surface tensions and foaming behavior of melts in the system CaO-FeO-SiO_2 . 921-925B
- Redox equilibria and kinetics of gas-slag reactions. 937-943B
- Interfacial kinetics of hydrogen with liquid slag containing iron oxide. 945-955B
- Dynamic and equilibrium interfacial phenomena in liquid steel-slag systems. 957-971B
- Interfacial phenomena in some slag-metal reactions. 973-980B
- Rate of interfacial reaction between liquid iron oxide and CO-CO_2 . 1049-1057B
- Hydrodynamics of fluid flow approaching a moving boundary. 1117-1123B
- Iron and steel making, Quality control**
- Developments in blast furnace process control at Port Kembla based on process fundamentals. 993-1003B
- Iron compounds, Crystal growth**
- Neutron diffraction and phase evolution of the mechanically alloyed intermetallic compound $\xi\text{-FeZn}_{13}$. 2739-2745A
- Iron compounds, Oxidation**
- Formation of pegs during high-temperature oxidation of Fe_3Al containing yttrium. 1685-1687A
- Iron compounds, Phase transformations**
- Crystallization of amorphous $\text{Fe}_{82}\text{P}_{18}$. 1067-1073A
- Iron ores, Reactions (chemical)**
- Effect of temperature on cementite formation by reaction of iron ore with $\text{H}_2\text{-CH}_4\text{-Ar}$ gas. 1139-1142B
- Iron oxides, Solubility**
- Solutions of iron oxides in molten cryolite. 609-613B
- Ironmaking**
- Dissolution rates of coals and graphite in Fe-C-S melts in direct ironmaking: dependence of carbon dissolution rate on carbon structure. 215-216B
- Dissolution rates of coals and graphite in Fe-C-S melts in direct ironmaking: influence of melt carbon and sulfur on carbon dissolution. 243-251B
- Influence of ash on mass transfer and interfacial reaction between natural graphite and liquid iron. 1099-1104B
- Some observations on the draining of $\text{CaO-SiO}_2\text{-Al}_2\text{O}_3$ slag bubble films. 1105-1115B
- Reoxidation of hot briquetted iron in salt water. 1133-1135B
- J integral**
- Modeling thermomechanical fatigue life of high-temperature titanium alloy IMI 834. 431-444A
- An investigation of dynamic failure in 2.3Ni-1.3Cr-0.17C steel. 1147-1154A
- Killed steels, Mechanical properties**
- Dynamic materials testing, texture, and yield-surface calculation of an automotive sheet steel. 2439-2448A
- Killed steels, Reactions (chemical)**
- In situ observations of inclusions at the (Mn,Si)-killed steel/ $\text{CaO-Al}_2\text{O}_3$ interface. 1135-1139B
- Kinetics**
- Thermodynamic-kinetic simulation of constrained dendrite growth in steels. 365-379B
- Mechanical behavior and damage kinetics in nodular cast iron. I. Damage mechanisms. 3063-3074A
- Mechanical behavior and damage kinetics in nodular cast iron. II. Hardening and damage. 3075-3085A
- Knoop hardness**
- Effect of long-term room-temperature storage on the structure and properties of glassy melt-spun Mg-Al-Ca alloys. 2155-2162A
- Ladle metallurgy**
- Fluid flow and inclusion removal in continuous casting tundish. 253-266B
- Nitrogen alloying of carbon and stainless steels by gas injection. 905-912B
- Modeling of gas-liquid reactions in ladle metallurgy. I. Physical modeling. 1447-1455B
- Modeling of gas-liquid reactions in ladle metallurgy. II. Numerical simulation. 1457-1464B
- Lamellar structure**
- The fracture resistance of a binary TiAl alloy. 71-80A
- Crystallization of amorphous $\text{Fe}_{82}\text{P}_{18}$. 1067-1073A
- Eutectic interface configurations during melting. 1261-1269A
- Creep deformation of TiAl-Si alloys with aligned γ/α_2 lamellar microstructures. 2463-2473A
- Interaction of deformation twin and 120°-rotational order fault domain boundary in the lamellar structure of two-phase TiAl-based alloys. 2823-2834A
- Lamellar structure, Heating effects**
- Discussion of "Surface relief and the displacive transformation to the lamellar microstructure in TiAl" and "Nanometer-scale, fully lamellar microstructure in an aged TiAl-based alloy". 2377-2379A
- Author's reply to: Discussion of "Surface relief and the displacive transformation to the lamellar microstructure in TiAl" and "Nanometer-scale, fully lamellar microstructure in an aged TiAl-based alloy". 2379-2383A
- Laminates, Mechanical properties**
- An investigation of the effects of ductile-layer thickness on the fracture behavior of nickel aluminide microlaminates. 1385-1399A
- Interfacial modification and impact properties of Nb/MoSi₂ laminate composites by the addition of ZrO_2 , NbSi₂, and SiC particles. 2075-2081A
- Laser beam cladding**
- Microstructural evolution during laser cladding of M2 high-speed steel. 2615-2625A
- Laser beam heating**
- Mechanical properties of laser-deposited composite boride coating using nanoindentation. 401-408A
- Elevated temperature oxidation of laser surface engineered composite boride coating on steel. 461-473A
- Surface amorphous and crystalline microstructure by alloying zirconium using Nd:YAG pulsed laser. 3123-3127A
- Laser beam welding**
- Dispersoid-free zones in the heat-affected zone of aluminum alloy welds. 1453-1459A
- Laterites, Beneficiation**
- Characterization of scales obtained during continuous nickel laterite pilot-plant leaching. 1175-1186B
- Lattice parameters, Coating effects**
- Microstructural evolution during laser cladding of M2 high-speed steel. 2615-2625A
- Lattice parameters, Deformation effects**
- Computer simulation of the initial rafting process of a nickel-base single-crystal superalloy. 585-597A
- Laves phase, Alloying effects**
- Atom probe field ion microscopy investigation of boron containing martensitic 9% chromium steel. 975-984A
- Role of Mo and W during sensitization of superaustenitic stainless steel—crystallography and composition of precipitates. 1893-1905A
- Leaching**
- A novel process for recovering rare earth from weathered black earth. 191-196B
- The electrochemical property of acetylene black suspension solution with ozone bubbling and its effects on copper dissolution. 235-241B
- Pore transport-controlled shrinking-core systems involving diffusion, migration, and homogeneous reactions. I. Formulation of model and rate equation for PbSO_4 -carbonate system. 683-691B
- Pore transport-controlled shrinking-core systems involving diffusion, migration, and homogeneous reactions. II. Application of model for PbSO_4 -carbon system to experimental data. 693-703B
- Lead (metal), Binary systems**
- A model of convection-induced oscillatory structure formation in peritectic alloys. 1233-1246A
- Lead (metal), Diffusion**
- Interdiffusion of Sn and Pb in liquid Pb-Sn alloys. 1343-1352A

- Lead (metal), Extraction**
Lead solubility in $\text{FeO}_x\text{-CaO-SiO}_2$ slags at iron saturation. 15-24B
Coupled experimental and thermodynamic modeling studies for metallurgical smelting and coal combustion slag systems. 621-630B
Pore transport-controlled shrinking-core systems involving diffusion, migration, and homogeneous reactions. I. Formulation of model and rate equation for PbSO_4 -carbonate system. 683-691B
Pore transport-controlled shrinking-core systems involving diffusion, migration, and homogeneous reactions. II. Application of model for PbSO_4 -carbon system to experimental data. 693-703B
- Lead (metal), Reactions (chemical)**
Dissolution of lead and bismuth in white metal ($\text{CuSb}_{0.5}$) at matte-smelting temperatures. 543-546B
- Lead base alloys, Diffusion**
Interdiffusion of Sn and Pb in liquid Pb-Sn alloys. 1343-1352A
- Lead base alloys, Directional solidification**
Mushy zone morphology during directional solidification of Pb-5.8 wt.% Sb alloy. 2275-2285A
- Leaded brasses, Mechanical properties**
Damage leading to ductile fracture under high strain-rate conditions. 831-844A
- Levitation melting**
Modeling of turbulent flow in electromagnetically levitated metal droplets. 171-178B
Modeling the dynamics of magnetic semilevitation melting. 179-189B
Equilibrium shape of a molten silicon drop in an electromagnetic levitator in microgravity environment. 327-329B
- Lime, Reactions (chemical)**
Phase diagram for the system $\text{CaO-Al}_2\text{O}_3\text{-ZrO}_2$. 25-33B
- Liquid flow**
Physical and mathematical models of steel flow and heat transfer in a tundish heated by plasma. 63-74B
Fluid flow and inclusion removal in continuous casting tundish. 253-266B
Numerical studies of the motion of particles in current-carrying liquid metals flowing in a circular pipe. 357-364B
Water model study of horizontal molten steel—Ar two-phase jet in a continuous casting mold. 453-460B
Dynamics of the spout of gas plumes discharging from a melt: experimental investigation with a large-scale water model. 461-468B
A computational model for defect prediction in shape castings based on the interaction of free surface flow, heat transfer, and solidification phenomena. 515-527B
Hydrodynamics of fluid flow approaching a moving boundary. 1117-1123B
Melt flow control in a multistrand tundish using a turbulence inhibitor. 1505-1515B
A new approach to numerical simulation of melt flows and interface instability in Hall-Héroult cells. 1541-1550B
- Liquid flow, Field effects**
The effect of a uniform direct current magnetic field on the stability of a stratified liquid flow/molten steel system. 317-326B
- Liquid flow, Processing effects**
Modeling of molten metal flow in a continuous casting process considering the effects of argon gas injection and static magnetic-field application. 1491-1503B
- Liquid metals, Diffusion**
The chemical diffusivity of oxygen in liquid iron oxide and a calcium ferrite. 1059-1068B
- Liquid metals, Electrochemistry**
Fundamental theories and concepts for predicting thermodynamic properties of high temperature ionic and metallic liquid solutions and vapor molecules. 579-586B
- Liquid metals, Phase transformations**
Enthalpy of mixing of liquid Ni-Zr and Cu-Ni-Zr alloys. 277-284B
Electrode potential studies of liquid-solid equilibrium in Na_3Bi -saturated Na-Bi melts. 411-414B
- Liquid metals, Phases (state of matter)**
Measurement of the activity of boron in liquid copper using a four-phase equilibrium technique. 2674-2678A
- Liquid metals, Physical properties**
Physical and mathematical models of steel flow and heat transfer in a tundish heated by plasma. 63-74B
Modeling of turbulent flow in electromagnetically levitated metal droplets. 171-178B
Numerical simulation of the flow and the solid transport when tilting a holding furnace. 207-214B
Equilibrium shape of a molten silicon drop in an electromagnetic levitator in microgravity environment. 327-329B
Numerical studies of the motion of particles in current-carrying liquid metals flowing in a circular pipe. 357-364B
Optimum parameters for wetting silicon carbide by aluminum alloys. 565-573A
Two-fluid simulation on the mixed convection flow pattern in a nonisothermal water model of continuous casting tundish. 867-875B
Hydrodynamics of fluid flow approaching a moving boundary. 1117-1123B
Modeling of molten metal flow in a continuous casting process considering the effects of argon gas injection and static magnetic-field application. 1491-1503B
Melt flow control in a multistrand tundish using a turbulence inhibitor. 1505-1515B
A new approach to numerical simulation of melt flows and interface instability in Hall-Héroult cells. 1541-1550B
- Liquid metals, Quality control**
On the detection and selective separation of inclusions in liquid metal cleanliness analyzer (LiMCA) systems. 767-777B
Numerical studies of the motion of spheroidal particles flowing with liquid metals through an electric sensing zone. 855-866B
Erratum: "Numerical studies of the motion of spheroidal particles flowing with liquid metals through an electric sensing zone". 1143B
- Liquid metals, Reactions (chemical)**
Dissolution rates of coals and graphite in Fe-C-S melts in direct ironmaking: influence of melt carbon and sulfur on carbon dissolution. 243-251B
Thermodynamic study of zinc-rich zinc-sodium alloys. 419-424B
X-ray fluorescence observations of bubble formation and separation at a metal-slag interface. 537-540B
Distribution equilibria of Pb and Cu between $\text{CaO-SiO}_2\text{-Al}_2\text{O}_3$ melts and liquid copper. 1261-1266B
A Monte Carlo simulation study of dissolution of graphite in iron-carbon melts. 1517-1525B
Copper and minor elements distribution between metal, matte, and fluorine slags. 1551-1553B
- Liquid metals, Solubility**
Dissolution rates of coals and graphite in Fe-C-S melts in direct ironmaking: dependence of carbon dissolution rate on carbon structure. 215-216B
Argon solubility in molten iron. 216-218B
The effect of lead on the activity of sodium in liquid zinc. 414-418B
Argon solubility in liquid steel. 913-919B
- Liquid metals, Surface properties**
Surface tension of molten silicon measured by the electromagnetic levitation method under microgravity. 1585-1589A
- Liquid phase sintering**
The effect of gravity on solution-precipitation during liquid phase sintering. 397-400A
Microstructural parameters related to liquid-phase sintering. 2607-2614A
Macroregression in quiescent melting and liquid-phase sintering. 2907-2916A
Simulation of percolation structure of grain bonding in liquid-phase sintering by three-dimensional grain structure reconstruction. 3187-3193A
- Liquidus**
Estimation of liquidus temperatures for multicomponent silicates from activation energies for viscous flow. 111-119B
Liquidus temperature determination in multicomponent alloys by thermal analysis. 497-501A
Examination of solidification pathways and the liquidus surface in the Nb-Ti-Al system. 1305-1321B
- Low alloy steels, Rolling**
Mathematical modeling of the hot strip rolling of microalloyed Nb, multiply alloyed Cr-Mo, and plain C-Mn steels. 511-530A
- Low alloy steels, Welding**
Modeling of inclusion growth and dissolution in the weld pool. 161-169B
The mechanism of brittle fracture in a microalloyed steel. I. Inclusion-induced cleavage. 641-652A
The mechanism of brittle fracture in a microalloyed steel. II. Mechanistic modeling. 653-667A
- Low carbon steels, Casting**
Argon solubility in molten iron. 216-218B
- Low carbon steels, Coating**
Mechanical properties of laser-deposited composite boride coating using nanoindentation. 401-408A
Elevated temperature oxidation of laser surface engineered composite boride coating on steel. 461-473A
Dynamic reactive wetting and its role in hot dip coating of steel sheet with an Al-Zn-Si alloy. 1069-1079B
Correlation of microstructure with the wear resistance and fracture toughness of hardfacing alloys reinforced with complex carbides. 3041-3052A
- Low carbon steels, Crystal growth**
Interfacial heat transfer and nucleation of steel on metallic substrates. 1081-1089B
- Low carbon steels, Heat treatment**
Modeling of dissolution, growth, and coarsening of aluminum nitride in low-carbon steels. 1907-1916A
- Low carbon steels, Magnetic properties**
Insight into the microstructural characterization of ferritic steel using micromagnetic parameters. 1053-1065A
- Low carbon steels, Metal working**
Strength and formability of ultra-low-carbon Ti-IF steels. 1305-1307A
- Low carbon steels, Rolling**
Microstructural model for hot strip rolling of high-strength low-alloy steels. 1247-1259A
- Low carbon steels, Steel making**
Behavior of nonmetallic inclusions in front of the solid-liquid interface in low-carbon steels. 1013-1021B
Modeling of gas-liquid reactions in ladle metallurgy. I. Physical modeling. 1447-1455B
Modeling of gas-liquid reactions in ladle metallurgy. II. Numerical simulation. 1457-1464B
- Low carbon steels, Welding**
The mechanism of brittle fracture in a microalloyed steel. I. Inclusion-induced cleavage. 641-652A
The mechanism of brittle fracture in a microalloyed steel. II. Mechanistic modeling. 653-667A
Microstructural evolution in ultra-low-carbon steel weldments. I. Controlled thermal cycling and continuous cooling transformation diagram of the weld metal. 2145-2153A

- Low cycle fatigue, Temperature effects**
Thermal activation of fatigue damage. 63-69A
- Lubrication**
Identification of rolling-sliding damage mechanisms in porous alloys. 3091-3099A
- Magnesium, Alloying additive**
The influence of Mg on creep properties and fracture behaviors of Mar-M247 superalloy under 1255 K/200 MPa. 1365-1373A
Solidification characteristics of the Al-8.3Fe-0.8V-0.9Si alloy. 1599-1610A
- Magnesium, Composite materials**
On the infiltration behavior of Al, Al-Li, and Mg melts through SiC_p bed. 319-325A
Characteristics of Mg-based composites synthesized using a novel mechanical disintegration and deposition technique. 1873-1881A
- Magnesium, Extraction**
Solubilities and Raman spectra of NdOCl in some chloride melts of interest for the electrowinning of magnesium from its oxide. 631-639B
- Magnesium, Reactions (chemical)**
Activity measurement of the constituents in liquid Cu-Mg and Cu-Ca alloys with mass spectrometry. 927-935B
- Magnesium base alloys, Casting**
On the detection and selective separation of inclusions in liquid metal cleanliness analyzer (LMCA) systems. 767-777B
- Magnesium base alloys, Microstructure**
The role of solute in grain refinement of magnesium. 2895-2906A
- Magnesium oxide, Impurities**
Grain-growth-inhibiting effects of primary inclusion particles of ZrO₂ and MgO in Fe-10 mass% Ni alloy. 1213-1223A
- Magnetic fields**
The effect of a uniform direct current magnetic field on the stability of a stratified liquid flux/molten steel system. 317-326B
- Magnetic induction, Microstructural effects**
Insight into the microstructural characterization of ferritic steel using micromagnetic parameters. 1053-1065A
- Manganese, Alloying elements**
Alloy design of FeMnSiCrNi shape-memory alloys related to stacking-fault energy. 581-584A
- Manganese, Binary systems**
Driving force for $\gamma \rightarrow \epsilon$ martensitic transformation and stacking fault energy of γ in Fe-Mn binary system. 355-360A
- Manganese base alloys, Reactions (chemical)**
Kinetics of manganese ore reduction by carbon monoxide. 477-490B
- Marine environments**
Influence of thermal aging on the reactivity of duplex stainless steel surfaces. 2015-2024A
- Martensite**
Effects of martensite morphology and volume fraction on quasi-static and dynamic deformation behavior of dual-phase steels. 1753-1760A
- Martensite, Deformation effects**
Investigation on the cold deformation strengthening mechanism in MP 159 alloy. 5-13A
- Martensite, Welding effects**
Correlation of the microstructure and fracture toughness of the heat-affected zones of an SA 508 steel. 1107-1119A
- Martensitic stainless steels, Mechanical properties**
Influence of alloying elements on the strain rate and temperature dependence of the flow stress of steels. 825-830A
Atom probe field ion microscopy investigation of boron containing martensitic 9% chromium steel. 975-984A
- Martensitic transformations**
Driving force for $\gamma \rightarrow \epsilon$ martensitic transformation and stacking fault energy of γ in Fe-Mn binary system. 355-360A
Surface relief of α'' martensite in a Ti-Mo alloy. 599-605A
A model for nonclassical nucleation of solid-solid structural phase transformations. 1321-1331A
Displacive transformations in Au-18 wt.% Cu-6 wt.% Al. 1917-1923A
Experimental studies on tribological properties of pseudoclastic TiNi alloy with comparison to stainless steel 304. 2773-2783A
- Martensitic transformations, Alloying effects**
Experimental investigation and thermodynamic calculation of the Ti-Ni-Cu shape memory alloys. 2423-2430A
- Martensitic transformations, Composition effects**
Alloy design of FeMnSiCrNi shape-memory alloys related to stacking-fault energy. 581-584A
- Martensitic transformations, Cooling effects**
Microstructural evolution in ultra-low-carbon steel weldments. I. Controlled thermal cycling and continuous cooling transformation diagram of the weld metal. 2145-2153A
- Martensitic transformations, Deformation effects**
Effect of microstructure variations on the formation of deformation-induced martensite and associated tensile properties in a β metastable Ti alloy. 1095-1106A
- Martensitic transformations, Heating effects**
Influence of aging on transformation characteristics in shape memory CuZnAl alloys. 349-354A
Effects of thermal cycling on the kinetics of the $\gamma \rightarrow \epsilon$ martensitic transformation in an Fe-17 wt.% Mn alloy. 2735-2738A
- Mass transfer**
Evaporation behavior of aluminum during the cold crucible induction skull melting of titanium aluminum alloys. 837-844B
Influence of ash on mass transfer and interfacial reaction between natural graphite and liquid iron. 1099-1104B
- Mathematical analysis**
Application of, and precautions for the use of, the Rule of Additivity in phase transformation. 675-682B
The limiting speeds of dislocations. 811-814A
Comparison between high and low strain-rate deformation of tantalum. 815-823A
Evaporation behavior of aluminum during the cold crucible induction skull melting of titanium aluminum alloys. 837-844B
Quantitative description of damage evolution in ductile fracture of tantalum. 845-851A
Transient liquid-phase bonding in two-phase ternary systems. 1187-1192A
Determining the three-dimensional morphology of γ -particles in γ - γ' superalloys. 1333-1342A
Interdiffusion of Sn and Pb in liquid Pb-Sn alloys. 1343-1352A
Dynamic materials testing, texture, and yield-surface calculation of an automotive sheet steel. 2439-2448A
Yield vertices for {123}<111> multiple slip. 2449-2456A
An oscillatory behavior of planar interface motion in the naphthalene-camphor system. 2678-2681A
Coarsening of intermetallic or compound precipitates in binary systems. 3195-3197A
Pseudobinary diffusion coefficients in the Ti-Mo-Ta system. 3198-3199A
- Mathematical models**
A numerical and experimental study of the rate of transformation in three directionally grown peritectic systems. 29-34A
Mechanical properties, microstructural stability and kinetics of α -phase formation in 29Cr-6Ni-2Mo-0.38N superduplex stainless steel. 35-45A
Finding boundary conditions: a coupling strategy for the modeling of metal casting processes. I. Experimental study and correlation development. 75-86B
Finding boundary conditions: a coupling strategy for the modeling of metal casting processes. II. Numerical study and analysis. 87-96B
Stress-strain response of a cast 319-T6 aluminum under thermomechanical loading. 139-151A
Modeling of inclusion growth and dissolution in the weld pool. 161-169B
Modeling of turbulent flow in electromagnetically levitated metal droplets. 171-178B
Modeling the dynamics of magnetic semilevitation melting. 179-189B
Modeling of the vacuum oxygen decarburization refining process. 197-206B
Numerical simulation of the flow and the solid transport when tilting a holding furnace. 207-214B
Dissolution rates of coals and graphite in Fe-C-S melts in direct ironmaking: dependence of carbon dissolution rate on carbon structure. 215-216B
Prediction of cracks in continuously cast steel beam blank through fully coupled analysis of fluid flow, heat transfer, and deformation behavior of a solidifying shell. 225-237A
Fluid flow and inclusion removal in continuous casting tundish. 253-266B
A model of the interfacial heat-transfer coefficient during unidirectional solidification of an aluminum alloy. 285-295B
Equilibrium shape of a molten silicon drop in an electromagnetic levitator in microgravity environment. 327-329B
Modeling of interdendritic strain and macrosegregation for dendritic solidification processes. I. Theory and experiments. 331-343B
Modeling of interdendritic strain and macrosegregation for dendritic solidification processes. II. Computation of interdendritic strain and segregation fields in steel ingots. 345-355B
Numerical studies of the motion of particles in current-carrying liquid metals flowing in a circular pipe. 357-364B
Thermodynamic-kinetic simulation of constrained dendrite growth in steels. 365-379B
Coal pyrolysis in a rotary kiln. I. Model of the pyrolysis of a single grain. 381-390B
Coal pyrolysis in a rotary kiln. II. Overall model of the furnace. 391-402B
Modeling thermomechanical fatigue life of high-temperature titanium alloy IMI 834. 431-444A
A mathematical model of aluminum depth filtration with ceramic foam filters. I. Validation for short-term filtration. 491-502B
A mathematical model of aluminum depth filtration with ceramic foam filters. II. Application to long-term filtration. 503-513B
Mathematical modeling of the hot strip rolling of microalloyed Nb, multiply alloyed Cr-Mo, and plain C-Mn steels. 511-530A
A computational model for defect prediction in shape castings based on the interaction of free surface flow, heat transfer, and solidification phenomena. 515-527B
Three-dimensional Monte Carlo simulation of grain growth in the heat-affected zone of a 2.25Cr-1Mo steel weld. 529-536B
The effect of matrix microstructure on the tensile and fatigue behavior of SiC particle-reinforced 2080 Al matrix composites. 531-540A
Prediction of properties of intermetallics using a chemical bonding model. 603-607B
The power of thermodynamic modeling: examples from molten halide mixtures. 641-650B
The modified quasicrystalline model I—binary solutions. 651-659B
The mechanism of brittle fracture in a microalloyed steel. II. Mechanistic modeling. 653-667A
Pore transport-controlled shrinking-core systems involving diffusion, migration, and homogeneous reactions. I. Formulation of model and rate equation for PbSO₄-carbonate system. 683-691B
Pore transport-controlled shrinking-core systems involving diffusion, migration, and homogeneous reactions. II. Application of model for PbSO₄-carbon system to experimental data. 693-703B
An integrated model for dendritic and planar interface growth and morphological transition in rapid solidification. 735-746A
On the detection and selective separation of inclusions in liquid metal cleanliness analyzer (LMCA) systems. 767-777B
Effect of albite particles on the coefficient of thermal expansion

- behavior of the Al6061 alloy composites. 773-780A
- Depth of oscillation marks forming in continuous casting of steel. 813-826B
- Influence of alloying elements on the strain rate and temperature dependence of the flow stress of steels. 825-830A
- Study of microsegregation buildup during solidification of spheroidal graphite cast iron. 827-836B
- Damage leading to ductile fracture under high strain-rate conditions. 831-844A
- Aluminum volatilization and inclusion removal in the electron beam cold hearth melting of Ti alloys. 845-854B
- Numerical studies of the motion of spheroidal particles flowing with liquid metals through an electric sensing zone. 855-866B
- Two-fluid simulation on the mixed convection flow pattern in a nonisothermal water model of continuous casting tundish. 867-875B
- On the approximation of the partial areas method in the calculation of the fraction of solid. 877-879B
- Deformation and fracture of a particle-reinforced aluminum alloy composite. II. Modeling. 937-950A
- Comparison between sulfide flash smelting and coal combustion—with implications for the flash smelting of high-grade concentrate. 1005-1012B
- A process model for the heat-affected zone microstructure evolution in duplex stainless steel weldments. II. Application to electron beam welding. 1035-1048A
- Hydrodynamics of fluid flow approaching a moving boundary. Heat generation during the fatigue of a cellular Al alloy. 1117-1123B
- Erratum: "Numerical studies of the motion of spheroidal particles flowing with liquid metals through an electric sensing zone". 1129-1136A
- Modeling of microstructure and residual stress in cast iron calender rolls. 1143B
- Microstructural model for hot strip rolling of high-strength low-alloy steels. 1201-1211A
- Equilibria involving the reciprocal spinel solid solution ($Mg_xFe_{1-x}(Al,Cr_{1-y})_2O_4$): modeling and experiment. 1247-1259A
- A model for prediction of pressure and redistribution of gas-forming elements in multicomponent casting alloys. 1247-1259B
- Thermal and grain-structure simulation in a land-based turbine blade directionally solidified with the liquid metal cooling process. 1283-1292B
- A model for nonclassical nucleation of solid-solid structural phase transformations. 1293-1304B
- Thermal analysis of the arc welding process. I. General solutions. 1321-1331A
- Numerical modeling of enhanced nitrogen dissolution during gas tungsten arc welding. 1353-1370B
- Unsteady Marangoni flow in a molten pool when welding dissimilar metals. 1371-1385B
- Creep-behavior modeling of the single-crystal superalloy CMSX-4. 1387-1403B
- Alpha case thickness modeling in investment castings. 1401-1411A
- An analysis of the effect of cavity nucleation rate and cavity coalescence on the tensile behavior of superplastic materials. 1419-1427B
- Modeling of gas-liquid reactions in ladle metallurgy. II. Numerical simulation. 1425-1434A
- Two-phase modeling of mushy zone parameters associated with hot tearing. 1457-1464B
- Mathematical modeling of the dynamic behavior of gas tungsten arc weld pools. 1461-1472A
- Hydrogen trapping models in steel. 1465-1473B
- Formulation of rod-forming models and their application in spray forming. 1475-1482B
- Analysis of secondary oxide-scale failure at entry into the roll gap. 1479-1488A
- Modeling of molten metal flow in a continuous casting process considering the effects of argon gas injection and static magnetic-field application. 1483-1490B
- On homogenization of a binary alloy after dissolution of planar and spherical precipitates. 1491-1503B
- Numerical calculation of the electromagnetic expulsive force upon nonmetallic inclusions in an aluminum melt. I. Spherical particles. 1525-1530A
- Numerical calculation of the electromagnetic expulsive force upon nonmetallic inclusions in an aluminum melt. II. Cylindrical particles. 1527-1533B
- A new approach to numerical simulation of melt flows and interface instability in Hall-Héroult cells. 1535-1540B
- A Scheil-Gulliver model with back-diffusion applied to the microsegregation of chromium in Fe-Cr-C alloys. 1541-1550B
- On convection in mushy phase and its effect on macrosegregation. 1682-1684A
- A model for creep-fatigue interaction in terms of crack-tip stress relaxation. 1687-1692A
- Tensile stress-strain analysis of single-structure steels. 1761-1775A
- Experimental investigation and thermodynamic modeling of the Cr-Ni-Si system. 1785-1794A
- Strain-localization in sheet metal containing a geometric defect. 1795-1803A
- Modeling of dissolution, growth, and coarsening of aluminum nitride in low-carbon steels. 1883-1886A
- The mechanical threshold stress constitutive-strength model description of HY-100 steel. 1907-1916A
- The influence of crystallographic texture and interstitial impurities on the mechanical behavior of zirconium. 1985-1996A
- Significance of the small crack growth law and its practical application. 1997-2003A
- Simulation of eutectic solidification structures of binary alloys: a multiparticle diffusion limited aggregation model. 2005-2013A
- A two-dimensional model for the description of the columnar-to-equiaxed transition in competing gray and white iron eutectics and its application to calender rolls. 2049-2057A
- A process model for the distortion induced by the electron-beam welding of a nickel-based superalloy. 2059-2068A
- Modeling gas diffusion into metals with a moving-boundary phase transformation. 2261-2273A
- Modeling creep and fatigue of copper alloys. 2411-2421A
- Development of a freckle predictor via Rayleigh number method for single-crystal nickel-base superalloy castings. 2491-2502A
- A dynamic model for the interaction between a solid particle and an advancing solid/liquid interface. 2545-2557A
- Simulation of polymer removal from a powder injection molding compact by thermal debinding. 2559-2568A
- Microstructural parameters related to liquid-phase sintering. 2597-2606A
- On the Gibbs-Thomson effect in concentrated binary systems. 2607-2614A
- Cyclic deformation, dislocation structure, and internal fatigue crack generation in a Ti-Fe-O alloy at liquid nitrogen temperature. 2659-2661A
- Modeling of spray-formed materials: geometrical considerations. 2793-2805A
- Influence of elastic inclusion morphology and matrix hardening behavior on Bauschinger effect in metal matrix composites. 2917-2929A
- Interpretation of microstructural evolution using dynamic materials modeling. 2943-2948A
- Fundamental aspects of hot isostatic pressing: an overview. 2973-2974A
- Effects of processing variables on the microsegregation of directionally cast samples. 2981-3000A
- Correlation between unsteady-state solidification conditions, dendrite spacings, and mechanical properties of Al-Cu alloys. 3137-3148A
- 3167-3178A
- ### Measurement
- Experimental difficulties associated with permeability measurements in aluminum alloys. 3149-3153A
- ### Mechanical alloying
- The role of dispersed particles in strengthening and fracture mechanisms in a Mo-ZrC alloy processed by mechanical alloying. 715-721A
- Phase transitions in reactive formation of $Ti_3Si_2/TiAl$ in situ composites. 763-771A
- Correlation of microstructure with dynamic deformation behavior and penetration performance of tungsten heavy alloys fabricated by mechanical alloying. 2475-2489A
- Neutron diffraction and phase evolution of the mechanically alloyed intermetallic compound ξ -FeZn₁₃. 2739-2745A
- Thermal transformations in mechanically alloyed Fe-Zn-Si materials. 2747-2754A
- ### Mechanical tests
- The use of the finite-element method to design an optimized tool for the plain-strain punch stretching test. 93-98A
- ### Mechanisms
- Mechanical behavior and damage kinetics in nodular cast iron. I. Damage mechanisms. 3063-3074A
- Mechanical behavior and damage kinetics in nodular cast iron. II. Hardening and damage. 3075-3085A
- ### Medium carbon steels, Heat treatment
- Theoretical and experimental investigations of electron beam surface remelting and alloying. 1405-1417B
- ### Medium carbon steels, Mechanical properties
- Influence of alloying elements on the strain rate and temperature dependence of the flow stress of steels. 825-830A
- Ultrasonic attenuation peak in steel and aluminum alloy during rotating bending fatigue. 1121-1128A
- Significance of the small crack growth law and its practical application. 2005-2013A
- ### Melt spinning
- Effect of long-term room-temperature storage on the structure and properties of glassy melt-spun Mg-Al-Ca alloys. 2155-2162A
- ### Melting
- Electrode potential studies of liquid-solid equilibrium in Na₃Bi-saturated Na-Bi melts. 411-414B
- Eutectic interface configurations during melting. 1261-1269A
- An experimental investigation on the kinetics of solute driven remelting. 2713-2720A
- ### Melting points
- Liquidus temperature determination in multicomponent alloys by thermal analysis. 497-501A
- ### Melting points, Composition effects
- Development of a low-melting-point filler metal for brazing aluminum alloys. 2239-2245A
- ### Melts, Electrochemistry
- Solubilities and Raman spectra of NdOCl in some chloride melts of interest for the electrowinning of magnesium from its oxide. 631-639B
- ### Melts, Transport properties
- The ionic properties of CaSiO₃ melt. 1241-1245B
- ### Metal carbonyls, Powder technology
- Length change and deformation of powder injection-molded compacts during solvent debinding. 1473-1478A
- Improved densification of carbonyl iron compacts by the addition of fine alumina powders. 1645-1652A
- ### Metal matrix composites, Mechanical properties
- Influence of elastic inclusion morphology and matrix hardening behavior on Bauschinger effect in metal matrix composites. 2943-2948A
- ### Metal matrix composites, Synthesis
- Investigation on reduction of CoAl₂O₄ by hydrogen gas using TGA. 540-542B
- ### Metal scrap, Recycling
- Contactless electrochemical reduction of titanium (II) chloride

- by aluminum. 713-721B
- Metallic glasses, Mechanical properties**
Effect of long-term room-temperature storage on the structure and properties of glassy melt-spun Mg-Al-Ca alloys. 2155-2162A
Hydrogen effects on an amorphous Fe-Si-B alloy. 2517-2526A
- Metallic glasses, Phase transformations**
Crystallization of amorphous Fe₈₂P₁₈. 1067-1073A
- Metallizing**
Growth of a Au-Ni-Sn intermetallic compound on the solder-substrate interface after aging. 798-800A
- Metallurgy**
Modified predominance diagrams for gas-solid reactions. 1429-1437B
- Metastable phases, Composition effects**
Effects of Cu content and preaging on precipitation characteristics in aluminum alloy 6022. 361-371A
- Metastable phases, Heating effects**
Spontaneous deformation during aging under stress in a copper-beryllium alloy. 2765-2771A
- Microgravity**
Equilibrium shape of a molten silicon drop in an electromagnetic levitator in microgravity environment. 327-329B
Surface tension of molten silicon measured by the electromagnetic levitation method under microgravity. 1585-1589A
Further discussion of "Particle engulfment and pushing by solidifying interfaces. II. Microgravity experiments and theoretical analysis". 1695-1700A
Authors' reply to: Further discussion of "Particle engulfment and pushing by solidifying interfaces. II. Microgravity experiments and theoretical analysis". 1700-1704A
- Microhardness**
Effect of long-term room-temperature storage on the structure and properties of glassy melt-spun Mg-Al-Ca alloys. 2155-2162A
Microhardness study of the nonlinear optical crystal L-arginine hydrochloride monohydrate. 3087-3090A
- Microhardness, Alloying effects**
Mechanical properties of austenitic stainless steel single crystals: influence of nitrogen and hydrogen content. 153-161A
- Microhardness, Processing effects**
Preparation and mechanical properties of highly densified nanocrystalline Al. 1017-1024A
- Microporosity**
A model for prediction of pressure and redistribution of gas-forming elements in multicomponent casting alloys. 1283-1292B
- Modulus of elasticity, Coating effects**
Mechanical properties of laser-deposited composite boride coating using nanoindentation. 401-408A
- Modulus of elasticity, Composition effects**
Effect of particle-size distribution on the properties of high-volume-fraction SiC₂-Al-based composites. 2351-2359A
- Modulus of elasticity, Microstructural effects**
Creep expansion of porous Ti-6Al-4V sandwich structures. 261-273A
- Modulus of elasticity, Processing effects**
An investigation of the synthesis of Ti-50 at.% Ni alloys through combustion synthesis and conventional powder sintering. 1867-1871A
- Molybdenum, Alloying additive**
Role of Mo and W during sensitization of superaustenitic stainless steel—crystallography and composition of precipitates. 1893-1905A
- Molybdenum, Alloying elements**
Chemical synthesis and characterization of low thermal expansion-high conductivity Cu-Mo and Ag-Mo composites. 2396-2398A
Synchrotron x-ray study of bulk lattice strains in externally loaded Cu-Mo composites. 2949-2962A
- Molybdenum, Composite materials**
Characterization of Mo-SiO₂ functionally graded materials. Design and fabrication of W-Mo-Ti-TiAl-Al system functionally graded material. 299-308A
2369-2376A
- Molybdenum, Diffusion**
Pseudobinary diffusion coefficients in the Ti-Mo-Ta system. 3198-3199A
- Molybdenum base alloys, Mechanical properties**
The role of dispersed particles in strengthening and fracture mechanisms in a Mo-ZrC alloy processed by mechanical alloying. 715-721A
- Molybdenum base alloys, Powder technology**
Synthesis of MoSi₂-TiSi₂ pseudobinary alloys by reactive sintering. 747-753A
- Molybdenum compounds, Composite materials**
Interfacial modification and impact properties of Nb/MoSi₂ laminate composites by the addition of ZrO₂, NbSi₂, and SiC particles. 2075-2081A
- Molybdenum compounds, Powder technology**
Synthesis of MoSi₂-TiSi₂ pseudobinary alloys by reactive sintering. 747-753A
- Monitoring**
Solid-state amperometric sensor for the in-situ monitoring of slag composition and transport properties. 733-753B
Numerical studies of the motion of spheroidal particles flowing with liquid metals through an electric sensing zone. 855-866B
Erratum: "Numerical studies of the motion of spheroidal particles flowing with liquid metals through an electric sensing zone". 1143B
- Morphology**
Early-stage Widmanstätten growth of the γ phase in a duplex steel. 15-19A
Determining the three-dimensional morphology of γ -particles in γ - γ' superalloys. 1333-1342A
- Influence of microstructure on the flow behavior of duplex stainless steels at high temperatures. 1353-1364A
- Effects of martensite morphology and volume fraction on quasi-static and dynamic deformation behavior of dual-phase steels. 1753-1760A
Banded microstructure formation in off-eutectic alloys. 1819-1832A
Aligned monotectic growth in unidirectionally solidified Zn-Bi alloys. 1833-1842A
Mushy zone morphology during directional solidification of Pb-5.8 wt.% Sb alloy. 2275-2285A
Microstructural studies on lattice imperfections in deformed zincium-base alloys by x-ray diffraction. 2405-2410A
- Morphology, Alloying effects**
Solidification characteristics of the Al-8.3Fe-0.8V-0.9Si alloy. 1599-1610A
- Morphology, Cooling effects**
The effect of cooling rate on the microstructures formed during solidification of ferritic steel. 3155-3166A
- Morphology, Deformation effects**
Computer simulation of the initial rafting process of a nickel-base single-crystal superalloy. 585-597A
Microstructural model for hot strip rolling of high-strength low-alloy steels. 1247-1259A
Recovery and ordering in cold-rolled boron-doped Ni₇₆Al₂₄. 2127-2134A
- Morphology, Heating effects**
Insight into the microstructural characterization of ferritic steel using micromagnetic parameters. 1053-1065A
Study of microstructure of low-temperature plasma-nitrided AISI 304 stainless steel. 1193-1199A
- Morphology, Processing effects**
Modeling of microstructure and residual stress in cast iron candle rolls. 1201-1211A
Characteristics of Mg-based composites synthesized using a novel mechanical disintegration and deposition technique. 1873-1881A
Microstructural evolution in wire-drawn Ti-22Al-26Nb powder. 2931-2941A
Microstructural characterization of novel in-situ Al-Be composites. 2963-2971A
Correlation between unsteady-state solidification conditions, dendrite spacings, and mechanical properties of Al-Cu alloys. 3167-3178A
- Morphology, Welding effects**
Dispersoid-free zones in the heat-affected zone of aluminum alloy welds. 1453-1459A
- Mossbauer spectroscopy**
Phase analysis of two steel work rolls using Mössbauer spectroscopy. 793-798A
- Nanomaterials, Coatings**
Mechanical properties of laser-deposited composite boride coating using nanoindentation. 401-408A
Synthesis of nanostructured WC-12%Co coating using mechanical milling and high velocity oxygen fuel thermal spraying. 541-553A
Synthesis of nanostructured Cr₃C₂-25(Ni₂₀Cr) coatings. 555-564A
- Nanomaterials, Powder technology**
Sintering behavior of nanocrystalline γ -Ni-Fe powders. 503-510A
Preparation and mechanical properties of highly densified nanocrystalline Al. 1017-1024A
- Near net shaping**
Simulation of polymer removal from a powder injection molding compact by thermal debinding. 2597-2606A
Near-net-shape forming of Al-Al₃Ni functionally graded material over eutectic melting temperature. 2627-2636A
- Necking**
Strain-localization in sheet metal containing a geometric defect. 1883-1886A
- Neodymium, Extraction**
Preparation of Nd(III) carbonate by precipitation stripping of Nd(III)-loaded VA10. 5-13B
- Neodymium compounds, Electrochemistry**
Thermodynamic and nonstoichiometric behavior of promising H₂-Ni cuprate systems via electromotive force measurements: a short review. 661-666B
- Neutron flux**
A Bayesian analysis of the influence of neutron irradiation on embrittlement in ferritic submerged arc weld metal. 445-459A
- Nickel, Alloying elements**
Design of quaternary Ir-Nb-Ni-Al refractory superalloys. 173-178A
Microstructure and formability of ZnNi alloy electrodeposited sheet steel. 475-485A
Alloy design of FeMnSiCrNi shape-memory alloys related to stacking-fault energy. 581-584A
- Nickel, Coatings**
Growth of a Au-Ni-Sn intermetallic compound on the solder-substrate interface after aging. 798-800A
- Nickel, Extraction**
The thermodynamics of the Ni-Co-S ternary system. Characterization of scales obtained during continuous nickel laterite pilot-plant leaching. 1175-1186B
Rate of slag reduction in a laboratory electric furnace—alternating vs. direct current. 1187-1194B
The anomalous behavior of Al³⁺ in nickel electrowinning from sulfate electrolytes. 1203-1211B
Phase equilibrium and minor-element distribution between Ni₃S₂-FeS matte and calcium ferrite slag under high partial pressures of SO₂. 1231-1239B
- Nickel, Microstructure**
Grain boundary faceting and abnormal grain growth in nickel. 985-994A

- Nickel, Physical properties**
Modeling of turbulent flow in electromagnetically levitated metal droplets. 171-178B
- Nickel, Powder technology**
Sintering behavior of nanocrystalline γ -Ni-Fe powders. 503-510A
- Nickel, Ternary systems**
Enthalpy of mixing of liquid Ni-Zr and Cu-Ni-Zr alloys. 277-284B
The 900°C isothermal section of Ti-Ni-V alloys. 1679-1682A
Experimental investigation and thermodynamic modeling of the Cr-Ni-Si system. 1795-1803A
- Nickel, Welding**
Unsteady Marangoni flow in a molten pool when welding dissimilar metals. 1387-1403B
- Nickel base alloys, Bonding**
Transient liquid-phase bonding in the Ni-Al-B system. 2835-2847A
- Nickel base alloys, Casting**
Freckle formation and freckle criterion in superalloy castings. A model for prediction of pressure and redistribution of gas-forming elements in multicomponent casting alloys. 801-811B
Development of a freckle predictor via Rayleigh number method for single-crystal nickel-base superalloy castings. 1283-1292B
2545-2557A
- Nickel base alloys, Coating**
Effects of sulfur on the fatigue and fracture resistance of interfaces between γ -Ni(Cr) and α -Al₂O₃. 1977-1983A
Effect of prealuminizing diffusion treatment on microstructural evolution of high-activity Pt-aluminide coatings. 2037-2047A
Nondestructive evaluation of residual stress for thermal barrier coated turbine blades by Cr³⁺ photoluminescence piezospectroscopy. 2388-2391A
- Nickel base alloys, Composite materials**
Reaction steps in the combustion synthesis of NiAl/TiB₂ composites. 433-438B
Reactive infiltration processing and secondary compressive creep of NiAl and NiAl-W composites. 781-792A
An investigation of the effects of ductile-layer thickness on the fracture behavior of nickel aluminide microlaminates. 1385-1399A
Effect of particle size and volume fraction in hot extrusion reaction synthesis of SiC particle reinforced NiAl. 1663-1670A
Reaction synthesis, microstructure, and mechanical properties of in situ composite NiAl-Al₂O₃-TiC. 1692-1695A
- Nickel base alloys, Corrosion**
Grain-boundary chemistry and intergranular corrosion in alloy 825. 1163-1173A
- Nickel base alloys, Crystal growth**
Effects of boron doping on the grain-growth kinetics and mechanical properties of γ/γ' nickel-aluminum alloys. 3179-3186A
- Nickel base alloys, Diffusion**
An interdiffusion study of a NiAl alloy using single-phase diffusion couples. 1519-1524A
- Nickel base alloys, Directional solidification**
Directional and single-crystal solidification of Ni-base superalloys. I. The role of curved isotherms on grain selection. 2877-2886A
Directional and single-crystal solidification of Ni-base superalloys. II. Coincidence site lattice character of grain boundaries. 2887-2893A
- Nickel base alloys, Extrusion**
Hot deformation mechanisms in a powder metallurgy nickel-base superalloy IN 625. 2317-2325A
- Nickel base alloys, Mechanical properties**
Fatigue crack path prediction in Udimet 720 nickel-based alloy single crystals. 109-123A
Effect of plastic anisotropy on the creep strength of single crystals of a nickel-based superalloy. 421-430A
The influence of Mg on creep properties and fracture behaviors of Mar-M247 superalloy under 1255 K/200 MPa. 1365-1373A
Creep-behavior modeling of the single-crystal superalloy CMSX-4. 1401-1411A
Creep properties of Ni₃(AlTiTa) γ phase single crystals. 1733-1740A
The effect of high-temperature oxidation on the creep behavior of a superalloy (Nimonic-105). 1777-1784A
Stress corrosion cracking mechanisms of Alloy 600 polycrystals and single crystals in primary water—influence of hydrogen. 2025-2036A
The influence of sulfur on stress-rupture fracture in Inconel 718 superalloys. 2135-2144A
On the primary creep of CMSX-4 superalloy single crystals. 2219-2228A
Environmentally enhanced deformation of ultra-high-purity Ni-16Cr-9Fe alloys. 2383-2388A
Experimental studies on tribological properties of pseudoelectrodeposited TiNi alloy with comparison to stainless steel 304. 2773-2783A
- Nickel base alloys, Microstructure**
Influence of solidification variables on the dendrite arm spacings of Ni-based superalloys. 546-551B
Determining the three-dimensional morphology of γ' -particles in γ/γ' superalloys. 1333-1342A
Recovery and ordering in cold-rolled boron-doped Ni₇₆Al₂₄. 2127-2134A
- Nickel base alloys, Oxidation**
Selective oxidation and internal nitridation during high-temperature exposure of single-crystalline nickel-base superalloys. 47-56A
- Nickel base alloys, Phase transformations**
Computer simulation of the initial rafting process of a nickel-base single-crystal superalloy. 585-597A
Experimental investigation and thermodynamic calculation of the Ti-Ni-Cu shape memory alloys. 2423-2430A
- Nickel base alloys, Phases (state of matter)**
Liquidus temperature determination in multicomponent alloys by thermal analysis. 497-501A
- Nickel base alloys, Powder technology**
An investigation of the synthesis of Ti-50 at.% Ni alloys through combustion synthesis and conventional powder sintering. 1867-1871A
- Nickel base alloys, Rolling**
Deformation behavior of a Ni₃Al(B,Zr) alloy during cold rolling. I. Changes in order and structure. 3001-3010A
Deformation behavior of a Ni₃Al(B,Zr) alloy during cold rolling. II. Microstructural and textural changes. 3011-3021A
- Nickel base alloys, Welding**
A process model for the distortion induced by the electron-beam welding of a nickel-based superalloy. 2261-2273A
- Nickel chromium molybdenum steels, Mechanical properties**
The effect of microstructural banding on failure initiation of HY-100 steel. 995-1005A
Residual strains in HY100 polycrystals: comparisons of experiments and simulations. 1543-1555A
The mechanical threshold stress constitutive-strength model description of HY-100 steel. 1985-1996A
- Nickel chromium molybdenum steels, Phases (state of matter)**
Crystallographic details of precipitates in Fe-22Cr-21Ni-6Mo-(N) super-austenitic stainless steels aged at 900°C. 1713-1723A
- Nickel chromium molybdenum steels, Welding**
Correlation of the microstructure and fracture toughness of the heat-affected zones of an SA 508 steel. 1107-1119A
- Nickel chromium steels, Mechanical properties**
An investigation of dynamic failure in 2.3Ni-1.3Cr-0.17C steel. 1147-1154A
- Nickel compounds, Composite materials**
Reaction steps in the combustion synthesis of NiAl/TiB₂ composites. 433-438B
Reactive infiltration processing and secondary compressive creep of NiAl and NiAl-W composites. 781-792A
An investigation of the effects of ductile-layer thickness on the fracture behavior of nickel aluminide microlaminates. 1385-1399A
Effect of particle size and volume fraction in hot extrusion reaction synthesis of SiC particle reinforced NiAl. 1663-1670A
Reaction synthesis, microstructure, and mechanical properties of in situ composite NiAl-Al₂O₃-TiC. 1692-1695A
Near-net-shape forming of Al₂Al₃Ni functionally graded material over eutectic melting temperature. 2627-2636A
- Nickel compounds, Crystal growth**
Effects of boron doping on the grain-growth kinetics and mechanical properties of γ/γ' nickel-aluminum alloys. 3179-3186A
- Nickel compounds, Diffusion**
An interdiffusion study of a NiAl alloy using single-phase diffusion couples. 1519-1524A
- Nickel compounds, Mechanical properties**
Creep properties of Ni₃(AlTiTa) γ phase single crystals. 1733-1740A
Experimental studies on tribological properties of pseudoelectrodeposited TiNi alloy with comparison to stainless steel 304. 2773-2783A
- Nickel compounds, Microstructure**
Recovery and ordering in cold-rolled boron-doped Ni₇₆Al₂₄. 2127-2134A
- Nickel compounds, Phase transformations**
Experimental investigation and thermodynamic calculation of the Ti-Ni-Cu shape memory alloys. 2423-2430A
- Nickel compounds, Rolling**
Deformation behavior of a Ni₃Al(B,Zr) alloy during cold rolling. I. Changes in order and structure. 3001-3010A
Deformation behavior of a Ni₃Al(B,Zr) alloy during cold rolling. II. Microstructural and textural changes. 3011-3021A
- Nickel mattes, Reactions (chemical)**
Phase equilibrium and minor-element distribution between Ni₃S₂-FeS matte and calcium ferrite slag under high partial pressures of SO₂. 1231-1239B
- Niobium, Alloying additive**
The influence of additions of Nb and Cr on the aluminizing behavior of TiAl alloy. 2391-2394A
- Niobium, Alloying elements**
Design of quaternary Ir-Nb-Ni-Al refractory superalloys. 173-178A
Strength and ductility of heavily drawn bundled Cu-Nb filamentary microcomposite wires with various Nb contents. 2457-2462A
- Niobium, Composite materials**
Interfacial modification and impact properties of Nb/MoSi₂ laminate composites by the addition of ZrO₂, NbSi₂, and SiC particles. 2075-2081A
- Niobium, Ternary systems**
Examination of solidification pathways and the liquidus surface in the Nb-Ti-Al system. 1305-1321B
- Niobium base alloys, Composite materials**
Effect of fiber volume fraction on the fracture behavior of Nb-1 wt.% Zr/218W composites at elevated temperatures. 873-887A
An investigation of the effects of ductile-layer thickness on the fracture behavior of nickel aluminide microlaminates. 1385-1399A
- Niobium base alloys, Crystal growth**
Examination of solidification pathways and the liquidus surface in the Nb-Ti-Al system. 1305-1321B
- Niobium base alloys, Mechanical properties**
Fatigue and fracture toughness of a Nb-Ti-Cr-Al-X single-phase alloy at ambient temperature. 1075-1084A
- Niobium compounds, Composite materials**
Development of a thermodynamic database for cemented carbides for design and processing simulations. 615-619B
Interfacial modification and impact properties of Nb/MoSi₂ laminate composites by the addition of ZrO₂, NbSi₂, and SiC particles. 2075-2081A
- Niobium compounds, Powder technology**

- Microstructural evolution in wire-drawn Ti-22Al-26Nb powder. 2931-2941A
- Nitrides, Crystal growth**
Modeling of dissolution, growth, and coarsening of aluminum nitride in low-carbon steels. 1907-1916A
- Nitrogen, Alloying additive**
Mechanical properties of austenitic stainless steel single crystals: influence of nitrogen and hydrogen content. 153-161A
Crystallographic details of precipitates in Fe-22Cr-21Ni-6Mo-(N) superaustenitic stainless steels aged at 900°C. 1713-1723A
- Nitrogen, Alloying elements**
Constitutive properties of hard-alpha titanium. 3029-3040A
- Nitrogen, Diffusion**
Selective oxidation and internal nitridation during high-temperature exposure of single-crystalline nickel-base superalloys. 47-56A
- Nitrogen, Reactions (chemical)**
Effects of aluminum, silicon, and boron on the dissolution rate of nitrogen into molten iron. 899-904B
Numerical modeling of enhanced nitrogen dissolution during gas tungsten arc welding. 1371-1385B
- Nitrogenized steels, Steel making**
Nitrogen alloying of carbon and stainless steels by gas injection. 905-912B
- Nodular iron, Crystal growth**
Study of microsegregation buildup during solidification of spherical graphite cast iron. 827-836B
- Nodular iron, Mechanical properties**
Mechanical behavior and damage kinetics in nodular cast iron. I. Damage mechanisms. 3063-3074A
Mechanical behavior and damage kinetics in nodular cast iron. II. Hardening and damage. 3075-3085A
- Nodular iron, Microstructure**
Microstructural development and austempering kinetics of ductile iron during thermomechanical processing. 2575-2585A
- Nonferrous castings, Crystal growth**
A model for prediction of pressure and redistribution of gas-forming elements in multicomponent casting alloys. 1283-1292B
Two-phase modeling of mushy zone parameters associated with hot tearing. 1461-1472A
Correlation between unsteady-state solidification conditions, dendrite spacings, and mechanical properties of Al-Cu alloys. 3167-3178A
- Nonferrous castings, Microstructure**
Porosity nucleation in metal-matrix composites. 2069-2074A
- Nonferrous castings, Quality control**
Freckle formation and freckle criterion in superalloy castings. 801-811B
- Nonmetallic inclusions**
Numerical simulation of the flow and the solid transport when tilting a holding furnace. 207-214B
Fluid flow and inclusion removal in continuous casting tundish. 253-266B
Microstructural characterization and analysis of inclusions in C-Mn steel and weld metals. 615-628A
The mechanism of brittle fracture in a microalloyed steel. I. Inclusion-induced cleavage. 641-652A
The mechanism of brittle fracture in a microalloyed steel. II. Mechanistic modeling. 653-667A
Behavior of nonmetallic inclusions in front of the solid-liquid interface in low-carbon steels. 1013-1021B
Numerical calculation of the electromagnetic expulsive force upon nonmetallic inclusions in an aluminum melt. I. Spherical particles. 1527-1533B
Numerical calculation of the electromagnetic expulsive force upon nonmetallic inclusions in an aluminum melt. II. Cylindrical particles. 1535-1540B
- Nonmetallic inclusions, Impurities**
Grain-growth-inhibiting effects of primary inclusion particles of ZrO₂ and MgO in Fe-10 mass% Ni alloy. 1213-1223A
- Nonmetallic inclusions, Reactions (chemical)**
In situ observations of inclusions at the (Mn,Si)-killed steel/CaO-Al₂O₃ interface. 1135-1139B
- Nonmetallic inclusions, Solubility**
Modeling of inclusion growth and dissolution in the weld pool. 161-169B
- Notch sensitivity**
Effect of plastic anisotropy on the creep strength of single crystals of a nickel-based superalloy. 421-430A
- Notch sensitivity, Microstructural effects**
Impact fracture toughness of porous iron and high-strength steels. 1443-1451A
- Nuclear reactor components, Mechanical properties**
Anisotropy of yielding in a Zr-2.5Nb pressure tube material. 409-420A
Anisotropic behavior and rupture of hydridized Zircaloy-4 sheets. 679-690A
Environmentally enhanced deformation of ultra-high-purity Ni-16Cr-9Fe alloys. 2383-2388A
- Nuclear reactor components, Microstructure**
Microstructural studies on lattice imperfections in deformed zirconium-base alloys by x-ray diffraction. 2405-2410A
- Nuclear reactor components, Welding**
Microstructural characterization and analysis of inclusions in C-Mn steel and weld metals. 615-628A
Creep deformation and fracture behavior of types 316 and 316L(N) stainless steels and their weld metals. 1175-1185A
Relation between microstructure, composition, and hot cracking in Ti-stabilized austenitic stainless steel weldments. 3109-3122A
- Nucleation**
Application of, and precautions for the use of, the Rule of Additivity in phase transformation. 675-682B
- Interfacial heat transfer and nucleation of steel on metallic substrates. 1081-1089B
An analysis of the effect of cavity nucleation rate and cavity coalescence on the tensile behavior of superplastic materials. 1425-1434A
- Nucleation, Composition effects**
Nucleation on ceramic particles in cast metal-matrix composites. 1295-1304A
- Nucleation, Processing effects**
Porosity nucleation in metal-matrix composites. 2069-2074A
- Order disorder, Deformation effects**
Recovery and ordering in cold-rolled boron-doped Ni₇₅Al₂₅. 2127-2134A
Deformation behavior of a Ni₃Al(B,Zr) alloy during cold rolling. I. Changes in order and structure. 3001-3010A
Deformation behavior of a Ni₃Al(B,Zr) alloy during cold rolling. II. Microstructural and textural changes. 3011-3021A
- Organic compounds, Mechanical properties**
Microhardness study of the nonlinear optical crystal L-arginine hydrochloride monohydrate. 3087-3090A
- Orientation relationships**
Early-stage Widmanstätten growth of the γ phase in a duplex steel. 15-19A
The fracture resistance of a binary TiAl alloy. 71-80A
Surface relief of α' martensite in a Ti-Mo alloy. 599-605A
Island grains of low misorientation angles formed during abnormal grain growth in Cu. 1489-1491A
Near-threshold fatigue crack growth behavior of 2195 aluminum-lithium alloy—prediction of crack propagation direction and influence of stress ratio. 1531-1541A
Aligned monotectic growth in unidirectionally solidified Zn-Bi alloys. 1833-1842A
Evolution of texture and grain misorientation in an Al-Mg alloy exhibiting low-temperature superplasticity. 2169-2180A
On the primary creep of CMSX-4 superalloy single crystals. 2219-2228A
- Orientation relationships, Alloying effects**
Crystallographic details of precipitates in Fe-22Cr-21Ni-6Mo-(N) superaustenitic stainless steels aged at 900°C. 1713-1723A
- Orientation relationships, Deformation effects**
Investigation on the cold deformation strengthening mechanism in MP 159 alloy. 5-13A
Computer simulation of the initial rafting process of a nickel-base single-crystal superalloy. 585-597A
- Orientation relationships, Processing effects**
Directional and single-crystal solidification of Ni-base superalloys. I. The role of curved isotherms on grain selection. 2877-2886A
Directional and single-crystal solidification of Ni-base superalloys. II. Coincidence site lattice character of grain boundaries. 2887-2893A
- Oscillations**
A model of convection-induced oscillatory structure formation in peritectic alloys. 1233-1246A
- Outokumpu flash smelting process**
Comparison between sulfide flash smelting and coal combustion—with implications for the flash smelting of high-grade concentrate. 1005-1012B
- Oxidation rate, High temperature effects**
The effect of high-temperature oxidation on the creep behavior of a superalloy (Nimonic-105). 1777-1784A
- Oxidation resistance, Coating effects**
Elevated temperature oxidation of laser surface engineered composite boride coating on steel. 461-473A
- Oxidation resistance, Composition effects**
Synthesis of MoSi₂-TiSi₂ pseudobinary alloys by reactive sintering. 747-753A
- Oxide coatings, Reactions (chemical)**
Modification of the interface in SiC/Al composites. 2361-2368A
- Oxides, Electrochemistry**
Thermodynamic and nonstoichiometric behavior of promising Hi-Tc cuprate systems via electromotive force measurements: a short review. 661-666B
- Oxygen, Diffusion**
The chemical diffusivity of oxygen in liquid iron oxide and a calcium ferrite. 1059-1068B
Alpha case thickness modeling in investment castings. 1419-1427B
Diffusion of oxygen in the Al₂O₃ oxidation product of TiAl₃. 3023-3028A
- Oxygen, Reactions (chemical)**
Thermodynamics of surfaces and adsorption in the Fe-C-S-O system. 267-276B
- Oxygen steel making**
Equilibria involving the reciprocal spinel solid solution (Mg_xFe_{1-x})(Al,Cr_{1-y/2}O₄)₂: modeling and experiment. 1247-1259B
Spinel-corundum equilibria and activities in the system MgO-Al₂O₃-Cr₂O₃ at 1473K. 1323-1332B
- Palladium, Ternary systems**
The prediction of the hydriding thermodynamics of Pd-Rh-Co ternary alloys. 667-673B
- Palladium base alloys, Phases (state of matter)**
The prediction of the hydriding thermodynamics of Pd-Rh-Co ternary alloys. 667-673B
- Palladium base alloys, Powder technology**
Solute segregation behavior in spray-atomized Pd-Rh-V(Co) powders. 1843-1855A
Factors influencing solute segregation of spray-atomized palladium alloy powders. 2681-2686A
- Partial pressure**

- Thermodynamic and nonstoichiometric behavior of promising Hi-Tc cuprate systems via electromotive force measurements: a short review. 661-666B
- Phase equilibrium and minor element distribution between $\text{FeO}_x\text{-SiO}_2\text{-MgO}$ -based slag and $\text{Cu}_2\text{S-FeS}$ matte at 1573K under high partial pressures of SO_2 . 705-712B
- Particle size**
Particulate penetration into solid droplets. 387-396A
- Particle size distribution**
The influence of reinforcement particle size distribution on the mechanical behavior of a stainless steel/TiN composite. 309-318A
Modeling of dissolution, growth, and coarsening of aluminum nitride in low-carbon steels. 1907-1916A
Effect of particle-size distribution on the properties of high-volume-fraction $\text{SiC}_p\text{-Al}$ -based composites. 2351-2359A
- Particles, Coating**
Modification of the interface in SiC/Al composites. 2361-2368A
- Particles, Crystal growth**
Nucleation on ceramic particles in cast metal-matrix composites. 1295-1304A
- Particles, Physical properties**
Optimum parameters for wetting silicon carbide by aluminum alloys. 565-573A
- Particulate composites, Casting**
Tribological properties of centrifugally cast copper alloy-graphite particle composite. 1283-1293A
Porosity nucleation in metal-matrix composites. 2069-2074A
- Particulate composites, Crystal growth**
Further discussion of "Particle engulfment and pushing by solidifying interfaces. II. Microgravity experiments and theoretical analysis". 1695-1700A
Authors' reply to: Further discussion of "Particle engulfment and pushing by solidifying interfaces. II. Microgravity experiments and theoretical analysis". 1700-1704A
A dynamic model for the interaction between a solid particle and an advancing solid/liquid interface. 2559-2568A
- Particulate composites, Extrusion**
Study of 6061- Al_2O_3 composites produced by reciprocating extrusion. 2587-2596A
- Particulate composites, Forging**
Plastic flow behavior during the forging of a 6061 Al/10 vol% Al_2O_3 (p) composite. 1310-1313A
- Particulate composites, Mechanical properties**
The influence of reinforcement particle size distribution on the mechanical behavior of a stainless steel/TiN composite. 309-318A
On the infiltration behavior of Al, Al-Li, and Mg melts through SiC_p bed. 319-325A
The effect of matrix microstructure on the tensile and fatigue behavior of SiC particle-reinforced 2080 Al matrix composites. 531-540A
Optimum parameters for wetting silicon carbide by aluminum alloys. 565-573A
Deformation and fracture of a particle-reinforced aluminum alloy composite. I. Experiments. 921-936A
Deformation and fracture of a particle-reinforced aluminum alloy composite. II. Modeling. 937-950A
The interactive role of inclusions and SiC reinforcement on the high-cycle fatigue resistance of particle reinforced metal matrix composites. 951-957A
The quasi-static and cyclic fatigue fracture behavior of 2014 aluminum alloy metal-matrix composites. 959-974A
High-temperature fracture and fatigue-crack growth behavior of an XD gamma-based titanium aluminide intermetallic alloy. 1413-1423A
Characteristics of Mg-based composites synthesized using a novel mechanical disintegration and deposition technique. 1873-1881A
Microstructure and properties of in situ Al/TiB₂ composite fabricated by in-melt reaction method. 1959-1964A
Interfacial modification and impact properties of Nb/MoSi₂ laminate composites by the addition of ZrO_2 , NbSi₂, and SiC particles. 2075-2081A
Effect of particle-size distribution on the properties of high-volume-fraction $\text{SiC}_p\text{-Al}$ -based composites. 2351-2359A
- Particulate composites, Metal working**
Effect of volume fraction of SiC_p reinforcement on the processing maps for 2124 Al matrix composites. 629-639A
- Particulate composites, Microstructure**
Nucleation on ceramic particles in cast metal-matrix composites. 1295-1304A
- Particulate composites, Powder technology**
Particulate penetration into solid droplets. 387-396A
Reaction steps in the combustion synthesis of NiAl/TiB₂ composites. 433-438B
Phase transitions in reactive formation of $\text{Ti}_3\text{Si}_2/\text{TiAl}$ in situ composites. 763-771A
Effect of particle size and volume fraction in hot extrusion reaction synthesis of SiC particle reinforced NiAl. 1663-1670A
Reaction synthesis, microstructure, and mechanical properties of in situ composite NiAl- $\text{Al}_2\text{O}_3\text{-TiC}$. 1692-1695A
- Particulate composites, Reactions (chemical)**
Modification of the interface in SiC/Al composites. 2361-2368A
- Particulate composites, Synthesis**
Chemically induced reduction: a viable process for synthesizing $\gamma\text{-TiAl}$ based intermetallic matrix composite powders containing nanocrystalline TiC. 151-159B
- Particulate composites, Thermal properties**
Effect of albite particles on the coefficient of thermal expansion behavior of the Al6061 alloy composites. 773-780A
- Pearlite, Structural hardening**
Effects of microstructural parameters on work hardening of pearlite at small strains. 2665-2669A
- Penetration, Size effects**
Particulate penetration into solid droplets. 387-396A
- Percolation, Processing effects**
Simulation of percolation structure of grain bonding in liquid-phase sintering by three-dimensional grain structure reconstruction. 3187-3193A
- Peritectic reactions**
A numerical and experimental study of the rate of transformation in three directionally grown peritectic systems. 29-34A
Kinetics of peritectic reaction and transformation in Fe-C alloys. 981-991B
A model of convection-induced oscillatory structure formation in peritectic alloys. 1233-1246A
- Permeability**
Experimental difficulties associated with permeability measurements in aluminum alloys. 3149-3153A
- Permeameters, Design**
Experimental difficulties associated with permeability measurements in aluminum alloys. 3149-3153A
- Phase boundary**
Liquidus temperature determination in multicomponent alloys by thermal analysis. 497-501A
- Phase decomposition, Heating effects**
Differential scanning calorimetry and electron diffraction investigation on low-temperature aging in Al-Zn-Mg alloys. 339-348A
- Phase diagram reactions**
Application of, and precautions for the use of, the Rule of Additivity in phase transformation. 675-682B
Some generalities in the analyses of equilibria in ionic solutions. 2105-2118A
Modeling gas diffusion into metals with a moving-boundary phase transformation. 2411-2421A
Measurement of the activity of boron in liquid copper using a four-phase equilibrium technique. 2674-2678A
- Phase diagrams**
Phase diagram for the system $\text{CaO-Al}_2\text{O}_3\text{-ZrO}_2$. 25-33B
A numerical and experimental study of the rate of transformation in three directionally grown peritectic systems. 29-34A
The 900°C isothermal section of Ti-Ni-V alloys. 1679-1682A
- Phase stability**
Phase diagram study for the alkali metal-oxychloride system. 795-799B
- Phase stability, Heating effects**
Displacive transformations in Au-18 wt.% Cu-6 wt.% Al. 1917-1923A
- Phosphorus, Reactions (chemical)**
The effects of alkaline earth metal ions and halogen ions on the chromium oxide activities in alkaline earth metal oxide-halide- Cr_2O_3 system fluxes. 469-475B
- Phosphorus compounds, Phase transformations**
Crystallization of amorphous $\text{Fe}_{82}\text{P}_{18}$. 1067-1073A
- Photoluminescence**
Nondestructive evaluation of residual stress for thermal barrier coated turbine blades by Cr^{3+} photoluminescence piezospectroscopy. 2388-2391A
- Physical chemistry**
Kinetics of manganese ore reduction by carbon monoxide. 477-490B
Distribution equilibria of Pb and Cu between $\text{CaO-SiO}_2\text{-Al}_2\text{O}_3$ melts and liquid copper. 1261-1266B
Activity of calcium in dilute liquid Si-Ca alloy. 1267-1272B
- Physical simulation**
Numerical simulation of the flow and the solid transport when tilting a holding furnace. 207-214B
Water model study of horizontal molten steel—Ar two-phase jet in a continuous casting mold. 453-460B
Dynamics of the spout of gas plumes discharging from a melt: experimental investigation with a large-scale water model. 461-468B
Eutectic interface configurations during melting. 1261-1269A
Modeling of gas-liquid reactions in ladle metallurgy. I. Physical modeling. 1447-1455B
Melt flow control in a multistrand tundish using a turbulence inhibitor. 1505-1515B
Banded microstructure formation in off-eutectic alloys. 1819-1832A
An oscillatory behavior of planar interface motion in the naphthalene-camphor system. 2678-2681A
- Pilot plants**
Electrodeposition of zinc from sodium zincate/hydroxide electrolytes in a spouted bed electrode. 755-766B
- Pipelines, Mechanical properties**
Analysis and prevention of yield strength drop during spiral piping of two high-strength API-X70 steels. 2669-2674A
- Piping, Mechanical properties**
Analysis and prevention of yield strength drop during spiral piping of two high-strength API-X70 steels. 2669-2674A
- Pitting (corrosion), Alloying effects**
Role of Mo and W during sensitization of superaustenitic stainless steel—crystallography and composition of precipitates. 1893-1905A
- Plasma processing**
Preparation and mechanical properties of highly densified nanocrystalline Al. 1017-1024A
- Plastic deformation**
Anisotropy of yielding in a Zr-2.5Nb pressure tube material. 409-420A
 δ/γ interface boundary sliding as a mechanism of strain accommodation during hot deformation in a duplex stainless steel. 1671-1677A
Synchrotron x-ray study of bulk lattice strains in externally

- loaded Cu-Mo composites. 2949-2962A
- Plastic deformation, Deformation effects**
Load sharing between austenite and ferrite in a duplex stainless steel during cyclic loading. 1557-1570A
- Plastic deformation, Microstructural effects**
The influence of crystallographic texture and interstitial impurities on the mechanical behavior of zirconium. 1997-2003A
- Plastic flow**
Flow behavior of the billet surface layer in porthole die extrusion of aluminum.
Interpretation of microstructural evolution using dynamic materials modeling. 1635-1643A
2973-2974A
- Plastic flow, Composition effects**
Constitutive properties of hard-alpha titanium. 3029-3040A
- Plastic flow, Microstructural effects**
Correlation between former alpha boundary growth kinetics and superplastic flow in Zn-22% Al.
Influence of microstructure on the flow behavior of duplex stainless steels at high temperatures. 163-172A
1353-1364A
- Plasticity**
The role of plasticity in bimaterial fracture with ductile interlayers.
The mechanical threshold stress constitutive-strength model description of HY-100 steel. 863-872A
1985-1996A
- Plate metal, Mechanical properties**
Simulation of shear plugging through thin plates using the GRIM Eulerian hydrocode. 853-860A
- Plating baths, Electrochemistry**
Electrodeposition of zinc from sodium zincate/hydroxide electrolytes in a spouted bed electrode. 755-766B
- Platinum compounds, Coatings**
Effect of prealuminizing diffusion treatment on microstructural evolution of high-activity Pt-aluminide coatings. 2037-2047A
- Pole figures**
Anisotropy of yielding in a Zr-2.5Nb pressure tube material.
Application of the phase-field method to the solidification of hot-dipped galvanized coatings. 409-420A
487-495A
Near-threshold fatigue crack growth behavior of 2195 aluminum-lithium alloy—prediction of crack propagation direction and influence of stress ratio. 1531-1541A
Role of foreign-object damage on thresholds for high-cycle fatigue in Ti-6Al-4V. 1571-1583A
1653-1662A
Through-thickness texture gradients in cold-rolled aluminum. Microstructure-ultrasonic inspectability relationships in Ti6242: signal-to-noise in fine-grain-processed Ti6242. 2119-2125A
Evolution of texture and grain misorientation in an Al-Mg alloy exhibiting low-temperature superplasticity. 2169-2180A
A study of through-thickness texture gradients in rolled sheets. 2299-2315A
- Porosity**
Creep expansion of porous Ti-6Al-4V sandwich structures.
Impact fracture toughness of porous iron and high-strength steels. 261-273A
1443-1451A
- Porosity, Coating effects**
On the evolution of porosity in spray-deposited tool steels. 723-733A
- Porosity, Processing effects**
Sintering behavior of nanocrystalline γ -Ni-Fe powders. 503-510A
Preparation of high porosity metal foams. 1345-1352B
An investigation of the synthesis of Ti-50 at.% Ni alloys through combustion synthesis and conventional powder sintering. 1867-1871A
Characteristics of Mg-based composites synthesized using a novel mechanical disintegration and deposition technique. 1873-1881A
Porosity nucleation in metal-matrix composites. 2069-2074A
- Porosity, Welding effects**
Improved microstructure and properties of 6061 aluminum alloy weldments using a double-sided arc welding process. 2537-2543A
- Powder coating**
Correlation of microstructure with the wear resistance and fracture toughness of hardfacing alloys reinforced with complex carbides. 3041-3052A
- Powder coatings, Mechanical properties**
Correlation of microstructure with the wear resistance and fracture toughness of hardfacing alloys reinforced with complex carbides. 3041-3052A
- Powder coatings, Synthesis**
Synthesis of nanostructured WC-12%Co coating using mechanical milling and high velocity oxygen fuel thermal spraying. 541-553A
Synthesis of nanostructured Cr_3C_2 -25(Ni20Cr) coatings. 555-564A
- Powder compacts, Extrusion**
Hot deformation mechanisms in a powder metallurgy nickel-base superalloy IN 625. 2317-2325A
- Powder compacts, Reactions (chemical)**
Modeling the reaction synthesis of shock-densified titanium-silicon powder mixture compacts. 307-316B
- Powder metallurgy**
Simulation of polymer removal from a powder injection molding compact by thermal debinding. 2597-2606A
- Powder metallurgy parts, Extrusion**
Hot deformation mechanisms in a powder metallurgy nickel-base superalloy IN 625. 2317-2325A
Study of 6061- Al_2O_3 composites produced by reciprocating extrusion. 2587-2596A
- Powder metallurgy parts, Mechanical properties**
Preparation and mechanical properties of highly densified nanocrystalline Al. 1017-1024A
- Powder spraying**
Solute segregation behavior in spray-atomized Pd-Rh-V(Co) powders. 1843-1855A
- Precipitates, Reactions (chemical)**
On homogenization of a binary alloy after dissolution of planar and spherical precipitates. 1525-1530A
- Precipitates, Solubility**
On the Gibbs-Thomson effect in concentrated binary systems. 2659-2661A
- Precipitation**
Anisotropic behavior and rupture of hydrided Zircaloy-4 sheets. 679-690A
Crystallization of amorphous $\text{Fe}_{82}\text{P}_{18}$. 1067-1073A
Nature of precipitates and constituent particles present in a ternary Al-Ge-Si alloy. 2093-2097A
Catalyzed precipitation in Al-Cu-Si. 2697-2711A
Transient liquid-phase bonding in the Ni-Al-B system. 2835-2847A
Coarsening of intermetallic or compound precipitates in binary systems. 3195-3197A
- Precipitation, Alloying effects**
Solidification characteristics of the Al-8.3Fe-0.8V-0.9Si alloy. 1599-1610A
Role of Mo and W during sensitization of superaustenitic stainless steel—crystallography and composition of precipitates. 1893-1905A
Precipitation processes in Al-Cu-Mg alloys microalloyed with Si. 2721-2733A
- Precipitation, Composition effects**
Effects of Cu content and preaging on precipitation characteristics in aluminum alloy 6022. 361-371A
- Precipitation, Deformation effects**
Microstructural model for hot strip rolling of high-strength low-alloy steels. 1247-1259A
- Precipitation, Heating effects**
Insight into the microstructural characterization of ferritic steel using micromagnetic parameters. 1053-1065A
Modeling of dissolution, growth, and coarsening of aluminum nitride in low-carbon steels. 1907-1916A
Spontaneous deformation during aging under stress in a copper-beryllium alloy. 2765-2771A
- Precipitation, Processing effects**
The effect of gravity on solution-precipitation during liquid phase sintering. 397-400A
Microstructure and mechanical behavior of spray-deposited Al-Cu-Mg(Ag-Mn) alloys. 2287-2298A
- Precipitation hardening alloys, Microstructure**
Determining the three-dimensional morphology of γ' -particles in γ - γ' superalloys. 1333-1342A
- Pressure castings, Mechanical properties**
Effect of testing frequency on the corrosion fatigue of a squeeze-cast aluminum alloy. 1137-1145A
- Pressure castings, Quality control**
Prevention of macrodefects in squeeze casting of an Al-7 wt.% Si alloy. 297-305B
- Pressure leaching**
Characterization of scales obtained during continuous nickel laterite pilot-plant leaching. 1175-1186B
- Pressure vessels, Welding**
Microstructural characterization and analysis of inclusions in C-Mn steel and weld metals. 615-628A
- Prestraining**
A model for predicting the effect of deformation after solution treatment on the subsequent artificial aging behavior of AA7030 and AA7108 alloys. 2327-2338A
- Process control**
Length change and deformation of powder injection-molded compacts during solvent debinding. 1473-1478A
- Process parameters**
Flow behavior of the billet surface layer in porthole die extrusion of aluminum. 1635-1643A
Superplastic forming of duplex stainless steel. 2394-2396A
- Proof stress, Deformation effects**
Equal-channel angular pressing of commercial aluminum alloys: grain refinement, thermal stability and tensile properties. 691-701A
- Proof stress, Microstructural effects**
An investigation of the effect of fatigue deformation on the residual mechanical properties of Ti-6Al-4V ELI. 1937-1948A
- Protective coatings, Crystal growth**
Application of the phase-field method to the solidification of hot-dipped galvanized coatings. 487-495A
- Protective coatings, Mechanical properties**
Mechanical properties of laser-deposited composite boride coating using nanoindentation. 401-408A
Microstructure and formability of ZnNi alloy electrodeposited sheet steel. 475-485A
Effects of sulfur on the fatigue and fracture resistance of interfaces between γ -Ni(Cr) and α - Al_2O_3 . 1977-1983A
Nondestructive evaluation of residual stress for thermal barrier coated turbine blades by Cr^{3+} photoluminescence piezospectroscopy. 2388-2391A
Correlation of microstructure with the wear resistance and fracture toughness of hardfacing alloys reinforced with complex carbides. 3041-3052A
Surface amorphous and crystalline microstructure by alloying zirconium using Nd:YAG pulsed laser. 3123-3127A
- Protective coatings, Microstructure**
Microstructural evolution during laser cladding of M2 high-speed steel. 2615-2625A

Protective coatings, Oxidation

Elevated temperature oxidation of laser surface engineered composite boride coating on steel.

461-473A

Pseudoelasticity

Experimental studies on tribological properties of pseudoelastic TiNi alloy with comparison to stainless steel 304.

2773-2783A

Punching

The use of the finite-element method to design an optimized tool for the plain-strain punch stretching test.

93-98A

Pyrolysis

Coal pyrolysis in a rotary kiln. I. Model of the pyrolysis of a single grain.

381-390B

Coal pyrolysis in a rotary kiln. II. Overall model of the furnace.

391-402B

Pyrometallurgy

Lead solubility in $\text{FeO}_x\text{-CaO-SiO}_2$ slags at iron saturation.

15-24B

Effect of a catalyst on the kinetics of reduction of celestite (SrSO_4) by active charcoal.

35-41B

Kinetics of oxidation of carbonaceous materials by CO_2 and H_2O between 1300° and 1500°C.

43-54B

The thermodynamics of the Ni-Co-S ternary system.

121-128B

Dissolution rates of coals and graphite in Fe-C-S melts in direct ironmaking: influence of melt carbon and sulfur on carbon dissolution.

243-251B

Phase equilibrium and minor element distribution between $\text{FeO}_x\text{-SiO}_2\text{-MgO}$ -based slag and $\text{Cu}_2\text{S-FeS}$ matte at 1573K under high partial pressures of SO_2 .

705-712B

Contactless electrochemical reduction of titanium (II) chloride by aluminum.

713-721B

The study of chlorination kinetics of copper (I) sulfide by calcium chloride in the presence of oxygen.

723-731B

Rate of slag reduction in a laboratory electric furnace—alternating vs. direct current.

1187-1194B

Experimental study of phase equilibria in the systems Fe-Zn-O and Fe-Zn-Si-O at metallic iron saturation.

1195-1201B

Quantitative metallography

Phase analysis of two steel work rolls using Mössbauer spectroscopy.

793-798A

Quenching (cooling)

Effects of strain rate and anisotropy on the tensile deformation properties of extruded AlZnMg alloys.

669-678A

Microstructural effects on fracture toughness in AA7010 plate.

2503-2515A

Spontaneous deformation during aging under stress in a copper-beryllium alloy.

2765-2771A

Radioactive waste

Grain-boundary chemistry and intergranular corrosion in alloy 825.

1163-1173A

Rapid solidification

Processing and microstructural characterization of Al-Cu alloys produced from rapidly solidified powders.

249-260A

Microstructural characterization of a rapidly solidified ultrahigh strength $\text{Al}_{94.5}\text{Cr}_{5.5}\text{Co}_{0.5}\text{Ce}_2$ alloy.

607-614A

An integrated model for dendritic and planar interface growth and morphological transition in rapid solidification.

735-746A

Monosize droplet deposition as a means to investigate droplet behavior during spray deposition.

1333-1344B

The atomic-structure changes in Al-16% Si alloy above the liquidus.

2163-2168A

High-temperature creep of an Al-8.5Fe-1.3V-1.7Si alloy processed by rapid solidification.

2229-2237A

Rare earth metals, Recovering

A novel process for recovering rare earth from weathered black earth.

191-196B

Rare gases, Environment

Effects of inert gases on fatigue crack growth and their transportation into subsurface regions in titanium.

1435-1441A

Reaction kinetics

A numerical and experimental study of the rate of transformation in three directionally grown peritectic systems.

29-34A

Effect of a catalyst on the kinetics of reduction of celestite (SrSO_4) by active charcoal.

35-41B

Kinetics of oxidation of carbonaceous materials by CO_2 and H_2O between 1300° and 1500°C.

43-54B

Galvanic interaction between chalcopyrite and manganese dioxide in sulfuric acid medium.

55-61B

The electrochemical property of acetylene black suspension solution with ozone bubbling and its effects on copper dissolution.

235-241B

Modeling the reaction synthesis of shock-densified titanium-silicon powder mixture compacts.

307-316B

Coal pyrolysis in a rotary kiln. I. Model of the pyrolysis of a single grain.

381-390B

Coal pyrolysis in a rotary kiln. II. Overall model of the furnace.

391-402B

Kinetics of Al_2O_3 dissolution in $\text{CaO-MgO-SiO}_2\text{-Al}_2\text{O}_3$ slags: in situ observations and analysis.

406-410B

The effect of lead on the activity of sodium in liquid zinc.

414-418B

Thermodynamic study of zinc-rich zinc-sodium alloys.

419-424B

Kinetics of manganese ore reduction by carbon monoxide.

477-490B

Investigation on reduction of CoAl_2O_4 by hydrogen gas using TGA.

540-542B

CoCl^+ : unique in all of molten salt? Pore transport-controlled shrinking-core systems involving diffusion, migration, and homogeneous reactions. I. Formulation of model and rate equation for PbSO_4 -carbonate system.

597-602B

Pore transport-controlled shrinking-core systems involving diffusion, migration, and homogeneous reactions. II. Application of model for PbSO_4 -carbon system to experimental data.

683-691B

Phase equilibrium and minor element distribution between $\text{FeO}_x\text{-SiO}_2\text{-MgO}$ -based slag and $\text{Cu}_2\text{S-FeS}$ matte at 1573K

693-703B

under high partial pressures of SO_2 .

705-712B

The study of chlorination kinetics of copper (I) sulfide by calcium chloride in the presence of oxygen.

723-731B

Recent advances in the fundamentals of the kinetics of steel-making reactions.

891-898B

Activity measurement of the constituents in liquid Cu-Mg and Cu-Ca alloys with mass spectrometry.

927-935B

Redox equilibria and kinetics of gas-slag reactions.

937-943B

Interfacial kinetics of hydrogen with liquid slag containing iron oxide.

945-955B

Dynamic and equilibrium interfacial phenomena in liquid steel-slag systems.

957-971B

Interfacial phenomena in some slag-metal reactions.

973-980B

Kinetics of peritectic reaction and transformation in Fe-C alloys.

981-991B

Rate of interfacial reaction between liquid iron oxide and CO-CO_2 .

1049-1057B

Crystallization of amorphous $\text{Fe}_{80}\text{P}_{10}$.

1067-1073A

Quantifying the heats of coal devolatilization.

1125-1131B

Rate of slag reduction in a laboratory electric furnace—alternating vs. direct current.

1187-1194B

Modified predominance diagrams for gas-solid reactions.

1429-1437B

Some generalities in the analyses of equilibria in ionic solutions.

2105-2118A

An experimental investigation on the kinetics of solute driven remelting.

2713-2720A

Reaction kinetics, Alloying effects

Effects of aluminum, silicon, and boron on the dissolution rate of nitrogen into molten iron.

899-904B

Reaction kinetics, Diffusion effects

On the mobility of the austenite-ferrite interface in Fe-Co and Fe-Cu.

379-385A

Reaction kinetics, Heating effects

Effects of thermal cycling on the kinetics of the $\gamma \rightarrow \epsilon$ martensitic transformation in an Fe-17 wt.% Mn alloy.

2735-2738A

Reaction kinetics, Temperature effects

Reduction of titania by methane-hydrogen-argon gas mixture.

129-139B

Effect of temperature on cementite formation by reaction of iron ore with $\text{H}_2\text{-CH}_4\text{-Ar}$ gas.

1139-1142B

Reaction mechanisms

Preparation of Nd(III) carbonate by precipitation stripping of Nd(III)-loaded VA10.

5-13B

On methane generation and decarburization in low-alloy Cr-Mo steels during hydrogen attack.

125-137A

Reduction of titania by methane-hydrogen-argon gas mixture.

129-139B

Chemically induced reduction: a viable process for synthesizing $\gamma\text{-TiAl}$ based intermetallic matrix composite powders containing nanocrystalline TiC.

151-159B

A novel process for recovering rare earth from weathered black earth.

191-196B

The electrochemical property of acetylene black suspension solution with ozone bubbling and its effects on copper dissolution.

235-241B

Modeling the reaction synthesis of shock-densified titanium-silicon powder mixture compacts.

307-316B

Reaction steps in the combustion synthesis of NiAl/TiB₂ composites.

433-438B

CoCl^+ : unique in all of molten salt? Selective arsenic-fixing roast of refractory gold concentrate.

597-602B

Mixed solvent systems for the extraction and stripping of iron(III) from concentrated acid chloride solutions.

1163-1168B

Characterization of scales obtained during continuous nickel laterite pilot-plant leaching.

1175-1186B

The anomalous behavior of Al^{3+} in nickel electrowinning from sulfate electrolytes.

1203-1211B

Some generalities in the analyses of equilibria in ionic solutions.

2105-2118A

Reactivity, Heating effects

Influence of thermal aging on the reactivity of duplex stainless steel surfaces.

2015-2024A

Recovery

Macroscopic and microscopic evolutions of a shot-peened layer during isothermal recovery.

213-224A

Recovery, Deformation effects

Recovery and ordering in cold-rolled boron-doped $\text{Ni}_{76}\text{Al}_{24}$.

2127-2134A

Recovery, High temperature effects

Stress-strain response of a cast 319-T6 aluminum under thermomechanical loading.

139-151A

Recrystallization

Effects of strain rate and anisotropy on the tensile deformation properties of extruded AlZnMg alloys.

669-678A

Microstructural effects on fracture toughness in AA7010 plate.

2503-2515A

Recrystallization, Alloying effects

Effects of boron doping on the grain-growth kinetics and mechanical properties of γ/γ' nickel-aluminum alloys.

3179-3186A

Recrystallization, Deformation effects

Substructural changes during hot deformation of a Fe-26Cr ferritic stainless steel.

21-27A

Mathematical modeling of the hot strip rolling of microalloyed Nb, multiply alloyed Cr-Mo, and plain C-Mn steels.

511-530A

Interpretation of microstructural evolution using dynamic materials modeling.

2973-2974A

Recrystallization, Heating effects

Effect of intermediate annealing on texture evolution and plastic anisotropy in an Al-Mg autobody alloy.

99-107A

Red mud, End uses

Formation of aluminum titanate-mullite composite from bauxite red mud.

551-553B

Reduction of area, Alloying effects

A comparison study of microstructure and mechanical properties of Ti-24Al-14Nb-3V-0.5Mo with and without Si.

2205-2217A

Residual stress, Alloying effects

Mechanical properties of austenitic stainless steel single crystals: influence of nitrogen and hydrogen content.

153-161A

Residual stress, Coating effects

Nondestructive evaluation of residual stress for thermal barrier coated turbine blades by Cr³⁺ photoluminescence piezospectroscopy.

2388-2391A

Residual stress, Deformation effects

Residual strains in HY100 polycrystals: comparisons of experiments and simulations.

1543-1555A

Load sharing between austenite and ferrite in a duplex stainless steel during cyclic loading.

1557-1570A

Dynamic materials testing, texture, and yield-surface calculation of an automotive sheet steel.

2439-2448A

Residual stress, Processing effects

Modeling of microstructure and residual stress in cast iron cinder rolls.

1201-1211A

Residual stress, Welding effects

Improved microstructure and properties of 6061 aluminum alloy weldments using a double-sided arc welding process.

2537-2543A

Resistivity

The ionic properties of CaSiO₃ melt.

1241-1245B

Resistivity, Composition effects

Characterization of Mo-SiO₂ functionally graded materials. Chemical synthesis and characterization of low thermal expansion-high conductivity Cu-Mo and Ag-Mo composites.

299-308A

2396-2398A

Rheological properties, Deformation effects

Thin-wall back extrusion of partially remelted semi-solid Sn-Pb.

57-62A

Rhodium, Ternary systems

The prediction of the hydriding thermodynamics of Pd-Rh-Co ternary alloys.

667-673B

Roasting

A novel process for recovering rare earth from weathered black earth.

191-196B

Selective arsenic-fixing roast of refractory gold concentrate.

1163-1168B

Rolling friction

Identification of rolling-sliding damage mechanisms in porous alloys.

3091-3099A

Rolling mill rolls, Casting

Modeling of microstructure and residual stress in cast iron cinder rolls.

1201-1211A

Rolling mill rolls, Phases (state of matter)

Phase analysis of two steel work rolls using Mössbauer spectroscopy.

793-798A

Rolling texture

Near-threshold fatigue crack growth behavior of 2195 aluminum-lithium alloy—prediction of crack propagation direction and influence of stress ratio.

1531-1541A

Through-thickness texture gradients in cold-rolled aluminum.

1653-1662A

A study of through-thickness texture gradients in rolled sheets.

2299-2315A

Deformation behavior of a Ni₃Al(B,Zr) alloy during cold rolling.

3001-3010A

I. Changes in order and structure.

3011-3021A

Deformation behavior of a Ni₃Al(B,Zr) alloy during cold rolling.

3011-3021A

II. Microstructural and textural changes.

Room temperature

Fatigue and fracture toughness of a Nb-Ti-Cr-Al-X single-phase alloy at ambient temperature.

1075-1084A

Sandwich construction, Mechanical properties

Creep expansion of porous Ti-6Al-4V sandwich structures.

261-273A

Scale (corrosion), Alloying effects

Formation of pegs during high-temperature oxidation of Fe₃Al containing yttrium.

1685-1687A

Scale (corrosion), Coating effects

Elevated temperature oxidation of laser surface engineered composite boride coating on steel.

461-473A

Scale (corrosion), Composition effects

The effect of aluminum content on the corrosion behavior of Fe-Al alloys in reducing environments at 700°C.

1805-1817A

Scale (corrosion), Processing effects

Analysis of secondary oxide-scale failure at entry into the roll gap.

1483-1490B

Scale (corrosion), Welding effects

Relevance of high-temperature oxidation in life assessment and microstructural degradation of Cr-Mo steel weldments.

3101-3108A

Sea water, Environment

Influence of thermal aging on the reactivity of duplex stainless steel surfaces.

2015-2024A

Segregations

A comparative study of the microstructures observed in statically cast and continuously cast Bi-In-Sn ternary eutectic alloy.

239-248A

Modeling of interdendritic strain and macrosegregation for dendritic solidification processes. I. Theory and experiments.

331-343B

Modeling of interdendritic strain and macrosegregation for dendritic solidification processes. II. Computation of interdendritic strain and segregation fields in steel ingots.

345-355B

Study of microsegregation buildup during solidification of spherical graphite cast iron.

827-836B

A model for prediction of pressure and redistribution of gas-forming elements in multicomponent casting alloys.

1283-1292B

On convection in mushy phase and its effect on macrosegregation.

1687-1692A

Monte Carlo sampling for microsegregation measurements in cast structures.

2569-2574A

Factors influencing solute segregation of spray-atomized palladium alloy powders.

2681-2686A

Effect of computational domain size on the mathematical modeling of transport processes and segregation during directional solidification.

3129-3135A

Segregations, Diffusion effects

A Scheil-Gulliver model with back-diffusion applied to the microsegregation of chromium in Fe-Cr-C alloys.

1682-1684A

Segregations, Processing effects

Solute segregation behavior in spray-atomized Pd-Rh-V(Co) powders.

1843-1855A

Macrosegregation in quiescent melting and liquid-phase sintering.

2907-2916A

Effects of processing variables on the microsegregation of directionally cast samples.

3137-3148A

Self-propagating synthesis

Reaction steps in the combustion synthesis of NiAl/TiB₂ composites.

433-438B

Phase transitions in reactive formation of Ti₅Si₃/TiAl in situ composites.

763-771A

Effect of particle size and volume fraction in hot extrusion reaction synthesis of SiC particle reinforced NiAl.

1663-1670A

Reaction synthesis, microstructure, and mechanical properties of in situ composite NiAl-Al₂O₃-TiC.

1692-1695A

An investigation of the synthesis of Ti-50 at.% Ni alloys through combustion synthesis and conventional powder sintering.

1867-1871A

Semi-solid processing

Thin-wall back extrusion of partially remelted semi-solid Sn-Pb.

57-62A

On the approximation of the partial areas method in the calculation of the fraction of solid.

877-879B

Sensitizing, Alloying effects

Role of Mo and W during sensitization of superaustenitic stainless steel—crystallography and composition of precipitates.

1893-1905A

Sensitizing, High temperature effects

Grain-boundary chemistry and intergranular corrosion in alloy 825.

1163-1173A

Sensors, Design

Solid-state amperometric sensor for the in-situ monitoring of slag composition and transport properties.

733-753B

Separation

Preparation of Nd(III) carbonate by precipitation stripping of Nd(III)-loaded VA10.

5-13B

X-ray fluorescence observations of bubble formation and separation at a metal-slag interface.

537-540B

On the detection and selective separation of inclusions in liquid metal cleanliness analyzer (LMCA) systems.

767-777B

Shape, Field effects

Equilibrium shape of a molten silicon drop in an electromagnetic levitator in microgravity environment.

327-329B

Shape memory, Alloying effects

Experimental investigation and thermodynamic calculation of the Ti-Ni-Cu shape memory alloys.

2423-2430A

Shape memory, Composition effects

Alloy design of FeMnSiCrNi shape-memory alloys related to stacking-fault energy.

581-584A

Shape memory alloys, Mechanical properties

Experimental studies on tribological properties of pseudoelastic TiNi alloy with comparison to stainless steel 304.

2773-2783A

Shape memory alloys, Phase transformations

Influence of aging on transformation characteristics in shape memory Cu₂ZnAl alloys.

349-354A

Alloy design of FeMnSiCrNi shape-memory alloys related to stacking-fault energy.

581-584A

Displacive transformations in Au-18 wt.% Cu-6 wt.% Al.

1917-1923A

Experimental investigation and thermodynamic calculation of the Ti-Ni-Cu shape memory alloys.

2423-2430A

Shape memory alloys, Powder technology

An investigation of the synthesis of Ti-50 at.% Ni alloys through combustion synthesis and conventional powder sintering.

1867-1871A

Shear strength, Processing effects

Correlation of microstructure with dynamic deformation behavior and penetration performance of tungsten heavy alloys fabricated by mechanical alloying.

2475-2489A

Sheet metal, Coating

Microstructure and formability of ZnNi alloy electrodeposited sheet steel.

475-485A

Dynamic reactive wetting and its role in hot dip coating of steel sheet with an Al-Zn-Si alloy.

1069-1079B

Sheet metal, Mechanical properties

Effect of intermediate annealing on texture evolution and plastic anisotropy in an Al-Mg autobody alloy.

99-107A

Anisotropic behavior and rupture of hydrided Zircaloy-4 sheets.

679-690A

Strain-localization in sheet metal containing a geometric defect.

1883-1886A

Dynamic materials testing, texture, and yield-surface calculation of an automotive sheet steel.

2439-2448A

Sheet metal, Metal working

Strength and formability of ultra-low-carbon Ti-IF steels.

1305-1307A

Sheet metal, Texture

A study of through-thickness texture gradients in rolled sheets.

2299-2315A

Shot peening

Macroscopic and microscopic evolutions of a shot-peened layer during isothermal recovery.

213-224A

Shrinkage

- Enhanced densification of cavitated dispersion-strengthened aluminum by thermal cycling. 2647-2657A
- Sigma phase, Alloying effects**
Crystallographic details of precipitates in Fe-22Cr-21Ni-6Mo-(N) superaustenitic stainless steels aged at 900°C. 1713-1723A
- Sigma phase, Crystal growth**
Mechanical properties, microstructural stability and kinetics of σ -phase formation in 29Cr-6Ni-2Mo-0.38N superduplex stainless steel. 35-45A
- Silicates, Composite materials**
Effect of albite particles on the coefficient of thermal expansion behavior of the Al6061 alloy composites. 773-780A
- Silicates, Physical properties**
Estimation of viscosities of ternary silicate melts using the excess Gibbs energy of mixing. 105-109B
Estimation of liquidus temperatures for multicomponent silicates from activation energies for viscous flow. 111-119B
- Silicates, Transport properties**
The ionic properties of CaSiO₃ melt. 1241-1245B
- Silicides, Composite materials**
Phase transitions in reactive formation of Ti₃Si₂/TiAl in situ composites. 763-771A
Interfacial modification and impact properties of Nb/MoSi₂ laminate composites by the addition of ZrO₂, NbSi₂, and SiC particles. 2075-2081A
- Silicides, Powder technology**
Modeling the reaction synthesis of shock-densified titanium-silicon powder mixture compacts. 307-316B
Synthesis of MoSi₂-TiSi₂ pseudobinary alloys by reactive sintering. 747-753A
- Silicon, Alloying additive**
Effects of aluminum, silicon, and boron on the dissolution rate of nitrogen into molten iron. 899-904B
A comparison study of microstructure and mechanical properties of Ti-24Al-14Nb-3V-0.5Mo with and without Si. 2205-2217A
Precipitation processes in Al-Cu-Mg alloys microalloyed with Si. 2721-2733A
The role of solute in grain refinement of magnesium. 2895-2906A
- Silicon, Alloying elements**
Alloy design of FeMnSiCrNi shape-memory alloys related to stacking-fault energy. 581-584A
Creep deformation of TiAl-Si alloys with aligned γ/α_2 lamellar microstructures. 2463-2473A
- Silicon, Physical properties**
Equilibrium shape of a molten silicon drop in an electromagnetic levitator in microgravity environment. 327-329B
- Silicon, Reactions (chemical)**
Activity of calcium in dilute liquid Si-Ca alloy. 1267-1272B
- Silicon, Surface properties**
Surface tension of molten silicon measured by the electromagnetic levitation method under microgravity. 1585-1589A
- Silicon, Ternary systems**
Experimental investigation and thermodynamic modeling of the Cr-Ni-Si system. 1795-1803A
- Silicon carbide, Composite materials**
On the infiltration behavior of Al, Al-Li, and Mg melts through SiC_p bed. 319-325A
Particulate penetration into solid droplets. 387-396A
The effect of matrix microstructure on the tensile and fatigue behavior of SiC particle-reinforced 2080 Al matrix composites. 531-540A
Optimum parameters for wetting silicon carbide by aluminum alloys. 565-573A
Effect of volume fraction of SiC_p reinforcement on the processing maps for 2124 Al matrix composites. 629-639A
Texture and residual strain in two SiC/Ti-6-2-4-2 titanium composites. 889-898A
Deformation and fracture of a particle-reinforced aluminum alloy composite. I. Experiments. 921-936A
Deformation and fracture of a particle-reinforced aluminum alloy composite. II. Modeling. 937-950A
The interactive role of inclusions and SiC reinforcement on the high-cycle fatigue resistance of particle reinforced metal matrix composites. 951-957A
Mechanisms, models and simulations of metal-coated fiber consolidation. 1271-1282A
Nucleation on ceramic particles in cast metal-matrix composites. 1295-1304A
Effect of particle size and volume fraction in hot extrusion reaction synthesis of SiC particle reinforced NiAl. 1663-1670A
Characteristics of Mg-based composites synthesized using a novel mechanical disintegration and deposition technique. 1873-1881A
Microstructure and properties of in situ Al/TiB₂ composite fabricated by in-melt reaction method. 1959-1964A
Interfacial modification and impact properties of Nb/MoSi₂ laminate composites by the addition of ZrO₂, NbSi₂, and SiC particles. 2075-2081A
Fatigue crack growth resistance of unidirectional fiber-reinforced titanium metal-matrix composites under transverse loading. 2083-2092A
Effect of particle-size distribution on the properties of high-volume-fraction SiC_p-Al-based composites. 2351-2359A
Modification of the interface in SiC/Al composites. 2361-2368A
Effect of interfacial debonding and sliding on matrix crack initiation during isothermal fatigue of SCS-6/Ti-15-3 composites. 2637-2645A
- Silicon dioxide, Bonding**
The role of plasticity in bimaterial fracture with ductile interlayers. 863-872A
- Silicon dioxide, Composite materials**
Thermal activation of fatigue damage. 63-69A
Characterization of Mo-SiO₂ functionally graded materials. 299-308A
- Silicon dioxide, Reactions (chemical)**
Microscale simulation of settler processes in copper matte smelting. 439-451B
- Silver, Binary systems**
A numerical and experimental study of the rate of transformation in three directionally grown peritectic systems. 29-34A
- Silver, Composite materials**
Thermal expansion behavior of silver matrix composites. 291-298A
- Silver, Ternary systems**
Tin-silver-copper eutectic temperature and composition. 1155-1162A
- Silver base alloys, Electrical properties**
Chemical synthesis and characterization of low thermal expansion-high conductivity Cu-Mo and Ag-Mo composites. 2396-2398A
- Simulation**
Two-fluid simulation on the mixed convection flow pattern in a nonisothermal water model of continuous casting tundish. 867-875B
- Single crystals, Crystal growth**
Morphological stability of Sm123 superconductor during peritectic solidification from Sm211 + L mixture. 141-149B
- Single crystals, Mechanical properties**
Fatigue crack path prediction in Udimet 720 nickel-based alloy single crystals. 109-123A
Creep-behavior modeling of the single-crystal superalloy CMSX-4. 1401-1411A
On the primary creep of CMSX-4 superalloy single crystals. 2219-2228A
- Sintering (powder metallurgy)**
Sintering behavior of nanocrystalline γ -Ni-Fe powders. 503-510A
The role of dispersed particles in strengthening and fracture mechanisms in a Mo-ZrC alloy processed by mechanical alloying. 715-721A
Preparation and mechanical properties of highly densified nanocrystalline Al. 1017-1024A
Improved densification of carbonyl iron compacts by the addition of fine alumina powders. 1645-1652A
An investigation of the synthesis of Ti-50 at.% Ni alloys through combustion synthesis and conventional powder sintering. 1867-1871A
Design and fabrication of W-Mo-Ti-TiAl-Al system functionally graded material. 2369-2376A
Correlation of microstructure with dynamic deformation behavior and penetration performance of tungsten heavy alloys fabricated by mechanical alloying. 2475-2489A
Fundamental aspects of hot isostatic pressing: an overview. 2981-3000A
- Sintering (powder metallurgy), Alloying effects**
Dilatometry study of the sintering behavior of boron-alloyed Fe-1.5% Mo powder. 1497-1506A
- Skull melting**
Evaporation behavior of aluminum during the cold crucible induction skull melting of titanium aluminum alloys. 837-844B
- Slab casting**
Argon solubility in molten iron. 216-218B
Modeling of molten metal flow in a continuous casting process considering the effects of argon gas injection and static magnetic-field application. 1491-1503B
- Slab casting, Field effects**
The effect of a uniform direct current magnetic field on the stability of a stratified liquid flux/molten steel system. 317-326B
- Slab casting, Quality control**
Depth of oscillation marks forming in continuous casting of steel. 813-826B
- Slags, Crystal growth**
The effect of water vapor on mold slag crystallization. 403-406B
- Slags, Physical properties**
Viscosity of a CaO-MgO-Al₂O₃-SiO₂ melt containing spinel particles at 1646K. 97-104B
Estimation of viscosities of ternary silicate melts using the excess Gibbs energy of mixing. 105-109B
Estimation of liquidus temperatures for multicomponent silicates from activation energies for viscous flow. 111-119B
The surface tensions and foaming behavior of melts in the system CaO-FeO-SiO₂. 921-925B
- Slags, Reactions (chemical)**
Phase diagram for the system CaO-Al₂O₃-ZrO₂. 25-33B
Kinetics of Al₂O₃ dissolution in CaO-MgO-SiO₂-Al₂O₃ slags: in situ observations and analysis. 406-410B
Microscale simulation of settler processes in copper matte smelting. 439-451B
X-ray fluorescence observations of bubble formation and separation at a metal-slag interface. 537-540B
Coupled experimental and thermodynamic modeling studies for metallurgical smelting and coal combustion slag systems. 621-630B
Phase equilibrium and minor element distribution between FeO_x-SiO₂-MgO-based slag and Cu₂S-FeS matte at 1573K under high partial pressures of SO₂. 705-712B
Solid-state amperometric sensor for the in-situ monitoring of slag composition and transport properties. 733-753B
Recent advances in the fundamentals of the kinetics of steel-making reactions. 891-898B
Redox equilibria and kinetics of gas-slag reactions. 937-943B
Interfacial kinetics of hydrogen with liquid slag containing iron oxide. 945-955B
Dynamic and equilibrium interfacial phenomena in liquid steel-slag systems. 957-971B
Interfacial phenomena in some slag-metal reactions. 973-980B
Rate of interfacial reaction between liquid iron oxide and CO-

- CO₂.
Equilibrium slag losses in ferrovanadium production.
Some observations on the draining of CaO-SiO₂-Al₂O₃ slag bubble films.
In situ observations of inclusions at the (Mn,Si)-killed steel/CaO-Al₂O₃ interface.
Rate of slag reduction in a laboratory electric furnace—alternating vs. direct current.
Experimental study of phase equilibria in the systems Fe-Zn-O and Fe-Zn-Si-O at metallic iron saturation.
Phase equilibrium and minor-element distribution between Ni₃S₂-FeS matte and calcium ferrite slag under high partial pressures of SO₂.
Distribution equilibria of Pb and Cu between CaO-SiO₂-Al₂O₃ melts and liquid copper.
Spinel-corundum equilibria and activities in the system MgO-Al₂O₃-Cr₂O₃ at 1473K.
Copper and minor elements distribution between metal, matte, and fluorine slags.
- Slags, Solubility**
Lead solubility in FeO_x-CaO-SiO₂ slags at iron saturation. 15-24B
- Sliding friction**
Identification of rolling-sliding damage mechanisms in porous alloys. 3091-3099A
- Sliding friction, Processing effects**
Tribological properties of centrifugally cast copper alloy-graphite particle composite. 1283-1293A
- Slip**
The influence of crystallographic texture and interstitial impurities on the mechanical behavior of zirconium.
Yield vertices for {123}<111> multiple slip. 1997-2003A
2449-2456A
- Slip bands**
The effect of microstructural banding on failure initiation of HY-100 steel. 995-1005A
- Slip planes**
Effect of plastic anisotropy on the creep strength of single crystals of a nickel-based superalloy. 421-430A
- Smelting**
Microscale simulation of settler processes in copper matte smelting. 439-451B
Dissolution of lead and bismuth in white metal (Cu₂S_{0.5}) at matte-smelting temperatures. 543-546B
Coupled experimental and thermodynamic modeling studies for metallurgical smelting and coal combustion slag systems. 621-630B
Phase equilibrium and minor element distribution between FeO_x-SiO₂-MgO-based slag and Cu₂S-FeS matte at 1573K under high partial pressures of SO₂. 705-712B
Recent advances in the fundamentals of the kinetics of steel-making reactions. 891-898B
Influence of ash on mass transfer and interfacial reaction between natural graphite and liquid iron. 1099-1104B
Some observations on the draining of CaO-SiO₂-Al₂O₃ slag bubble films. 1105-1115B
Rate of slag reduction in a laboratory electric furnace—alternating vs. direct current. 1187-1194B
Phase equilibrium and minor-element distribution between Ni₃S₂-FeS matte and calcium ferrite slag under high partial pressures of SO₂. 1231-1239B
Equilibria involving the reciprocal spinel solid solution (Mg_xFe_{1-x})(Al_{1-x}Cr_x)₂O₄: modeling and experiment. 1247-1259B
Spinel-corundum equilibria and activities in the system MgO-Al₂O₃-Cr₂O₃ at 1473K. 1323-1332B
Copper and minor elements distribution between metal, matte, and fluorine slags. 1551-1553B
- Sodium, Reactions (chemical)**
Thermodynamic study of zinc-rich zinc-sodium alloys. 419-424B
- Sodium, Solubility**
The effect of lead on the activity of sodium in liquid zinc. 414-418B
- Sodium base alloys, Phase transformations**
Electrode potential studies of liquid-solid equilibrium in Na₃Bi-saturated Na-Bi melts. 411-414B
- Solderability, Coating effects**
Thermal stability of electroless-nickel/solder interface: A. Interfacial chemistry and microstructure. 2857-2866A
Thermal stability of electroless-nickel/solder interface: B. Interfacial fatigue resistance. 2867-2875A
- Soldered joints, Thermal properties**
Thermal stability of electroless-nickel/solder interface: A. Interfacial chemistry and microstructure. 2857-2866A
Thermal stability of electroless-nickel/solder interface: B. Interfacial fatigue resistance. 2867-2875A
- Soldering**
Growth of a Au-Ni-Sn intermetallic compound on the solder-substrate interface after aging. 798-800A
- Solders, Phases (state of matter)**
Tin-silver-copper eutectic temperature and composition. 1155-1162A
- Solid phases**
The identification of hydrogen trapping states in an Al-Li-Cu-Zr alloy using thermal desorption spectroscopy. 179-193A
Phase analysis of two steel work rolls using Mössbauer spectroscopy. 793-798A
- Solid phases, Crystal growth**
Application of, and precautions for the use of, the Rule of Additivity in phase transformation. 675-682B
- Solidification**
Morphological stability of Sm123 superconductor during peritectic solidification from Sm211 + L mixture. 141-149B
- Prediction of cracks in continuously cast steel beam blank through fully coupled analysis of fluid flow, heat transfer, and deformation behavior of a solidifying shell. 225-237A
A comparative study of the microstructures observed in statically cast and continuously cast Bi-In-Sn ternary eutectic alloy. 239-248A
Modeling of interdendritic strain and macrosegregation for dendritic solidification processes. I. Theory and experiments. 331-343B
Modeling of interdendritic strain and macrosegregation for dendritic solidification processes. II. Computation of interdendritic strain and segregation fields in steel ingots. 345-355B
Thermodynamic-kinetic simulation of constrained dendrite growth in steels. 365-379B
Electrode potential studies of liquid-solid equilibrium in Na₃Bi-saturated Na-Bi melts. 411-414B
A computational model for defect prediction in shape castings based on the interaction of free surface flow, heat transfer, and solidification phenomena. 515-527B
Influence of solidification variables on the dendrite arm spacings of Ni-based superalloys. 546-551B
Study of microsegregation buildup during solidification of spherical graphite cast iron. 827-836B
On the approximation of the partial areas method in the calculation of the fraction of solid. 877-879B
Behavior of nonmetallic inclusions in front of the solid-liquid interface in low-carbon steels. 1013-1021B
Mechanisms of initial melt/substrate heat transfer pertinent to strip casting. 1023-1030B
Measurements, simulations, and analyses of instantaneous heat fluxes from solidifying steels to the surfaces of twin roll casters and of aluminum to plasma-coated metal substrates. 1031-1047B
Interfacial heat transfer and nucleation of steel on metallic substrates. 1081-1089B
Quantifying the heats of coal devolatilization. 1125-1131B
Transient liquid-phase bonding in two-phase ternary systems. 1187-1192A
A model for prediction of pressure and redistribution of gas-forming elements in multicomponent casting alloys. 1283-1292B
Examination of solidification pathways and the liquidus surface in the Nb-Ti-Al system. 1305-1321B
Two-phase modeling of mushy zone parameters associated with hot tearing. 1461-1472A
Solidification parameters during the columnar-to-equiaxed transition in lead-tin alloys. 1611-1625A
On convection in mushy phase and its effect on macrosegregation. 1687-1692A
Banded microstructure formation in off-eutectic alloys. 1819-1832A
Simulation of eutectic solidification structures of binary alloys: a multiparticle diffusion limited aggregation model. 2049-2057A
A two-dimensional model for the description of the columnar-to-equiaxed transition in competing gray and white iron eutectics and its application to calendar rolls. 2059-2068A
A dynamic model for the interaction between a solid particle and an advancing solid/liquid interface. 2559-2568A
An experimental investigation on the kinetics of solute driven remelting. 2713-2720A
The effect of cooling rate on the microstructures formed during solidification of ferritic steel. 3155-3166A
Correlation between unsteady-state solidification conditions, dendrite spacings, and mechanical properties of Al-Cu alloys. 3167-3178A
- Solidification, Alloying effects**
Solidification characteristics of the Al-3.3Fe-0.8V-0.9Si alloy. 1599-1610A
- Solidification, Coating effects**
Application of the phase-field method to the solidification of hot-dipped galvanized coatings. 487-495A
- Solution heat treatment**
Part II. Metallurgical factors governing the H-assisted intergranular cracking of peak-aged Ti-3Al-8V-6Cr-4Mo-4Zr (Beta-C). Effects of strain rate and anisotropy on the tensile deformation properties of extruded AlZnMg alloys. 669-678A
A model for predicting the effect of deformation after solution treatment on the subsequent artificial aging behavior of AA7030 and AA7108 alloys. 2327-2338A
Microstructural effects on fracture toughness in AA7010 plate. 2503-2515A
Spontaneous deformation during aging under stress in a copper-beryllium alloy. 2765-2771A
- Solvent extraction**
Mixed solvent systems for the extraction and stripping of iron(III) from concentrated acid chloride solutions. 1169-1174B
- Spacecraft components, Mechanical properties**
The effect of processing and microstructure development on the slip and fracture behavior of the 2.1 wt.% Li AF/C-489 and 1.8 wt.% Li AF/C-458 Al-Li-C-X alloys. 1965-1976A
- Spalling**
Hydrogen effects on the spall strength and fracture characteristics of amorphous Fe-Si-B alloy at very high strain rates. 1085-1093A
- Spectroscopy**
Nondestructive evaluation of residual stress for thermal barrier coated turbine blades by Cr³⁺ photoluminescence piezospectroscopy. 2388-2391A
- Spinel, Reactions (chemical)**
Equilibria involving the reciprocal spinel solid solution (Mg_xFe_{1-x})(Al_{1-x}Cr_x)₂O₄: modeling and experiment. 1247-1259B
Spinel-corundum equilibria and activities in the system MgO-Al₂O₃-Cr₂O₃ at 1473K. 1323-1332B
- Splat cooling**
An integrated model for dendritic and planar interface growth and morphological transition in rapid solidification. 735-746A
- Spray forming**

- Monosize droplet deposition as a means to investigate droplet behavior during spray deposition. 1333-1344B
- Formulation of rod-forming models and their application in spray forming. 1479-1488A
- Modeling of spray-formed materials: geometrical considerations. 2917-2929A
- Spray forming, Size effects**
- Particulate penetration into solid droplets. 387-396A
- Sprayed coatings, Microstructure**
- On the evolution of porosity in spray-deposited tool steels. 723-733A
- Spraying**
- Microstructure and mechanical behavior of spray-deposited Al-Cu-Mg(Ag-Mn) alloys. 2287-2298A
- Squeeze casting**
- Effect of testing frequency on the corrosion fatigue of a squeeze-cast aluminum alloy. 1137-1145A
- Effect of particle-size distribution on the properties of high-volume-fraction SiC_p-Al-based composites. 2351-2359A
- Squeeze casting, Quality control**
- Prevention of macrodefects in squeeze casting of an Al-7 wt.% Si alloy. 297-305B
- Stacking fault energy**
- Driving force for $\gamma \rightarrow \epsilon$ martensitic transformation and stacking fault energy of γ in Fe-Mn binary system. 355-360A
- Stacking fault energy, Composition effects**
- Alloy design of FeMnSiCrNi shape-memory alloys related to stacking-fault energy. 581-584A
- Stainless steels, Refining**
- Modeling of the vacuum oxygen decarburization refining process. 197-206B
- Stainless steels, Steel making**
- Nitrogen alloying of carbon and stainless steels by gas injection. 905-912B
- Equilibria involving the reciprocal spinel solid solution (Mg,Fe_{1-x})(Al,Cr_{1-y})₂O₄: modeling and experiment. 1247-1259B
- Spinel-corundum equilibria and activities in the system MgO-Al₂O₃-Cr₂O₃ at 1473K. 1323-1332B
- Steels, Casting**
- Phase diagram for the system CaO-Al₂O₃-ZrO₂. 25-33B
- Prediction of cracks in continuously cast steel beam blank through fully coupled analysis of fluid flow, heat transfer, and deformation behavior of a solidifying shell. 225-237A
- Fluid flow and inclusion removal in continuous casting tundish. The effect of a uniform direct current magnetic field on the stability of a stratified liquid flux/molten steel system. 253-266B
- Water model study of horizontal molten steel—Ar two-phase jet in a continuous casting mold. 317-326B
- Dynamics of the spout of gas plumes discharging from a melt: experimental investigation with a large-scale water model. 453-460B
- On the detection and selective separation of inclusions in liquid metal cleanliness analyzer (LiMCA) systems. 461-468B
- A new criterion for internal crack formation in continuously cast steels. 767-777B
- Depth of oscillation marks forming in continuous casting of steel. 779-794B
- Two-fluid simulation on the mixed convection flow pattern in a nonisothermal water model of continuous casting tundish. 813-826B
- Measurements, simulations, and analyses of instantaneous heat fluxes from solidifying steels to the surfaces of twin roll casters and of aluminum to plasma-coated metal substrates. 867-875B
- Phase diagram cupidine (3CaO•2SiO₂•CaF₂)•CaF₂. 1031-1047B
- Modeling of molten metal flow in a continuous casting process considering the effects of argon gas injection and static magnetic-field application. 1273-1281B
- 1491-1503B
- Steels, Coating**
- Microstructure and formability of ZnNi alloy electrodeposited sheet steel. 475-485A
- Steels, Diffusion**
- Hydrogen trapping models in steel. 1475-1482B
- Steels, Mechanical properties**
- Tensile stress-strain analysis of single-structure steels. 1785-1794A
- Steels, Phase transformations**
- On the mobility of the austenite-ferrite interface in Fe-Co and Fe-Cu. 379-385A
- Steels, Reactions (chemical)**
- The effects of alkaline earth metal ions and halogen ions on the chromium oxide activities in alkaline earth metal oxide-halide-Cr₂O₃ system fluxes. 469-475B
- A Monte Carlo simulation study of dissolution of graphite in iron-carbon melts. 1517-1525B
- Steels, Refining**
- Dynamic and equilibrium interfacial phenomena in liquid steel-slag systems. 957-971B
- Steels, Rolling**
- Analysis of secondary oxide-scale failure at entry into the roll gap. 1483-1490B
- Steels, Structural hardening**
- Effects of microstructural parameters on work hardening of pearlite at small strains. 2665-2669A
- Steels, Welding**
- Thermal analysis of the arc welding process. I. General solutions. 1353-1370B
- Stoichiometry**
- An interdiffusion study of a NiAl alloy using single-phase diffusion couples. 1519-1524A
- Strain**
- Texture and residual strain in two SiC/Ti-6-2-4-2 titanium composites. 889-898A
- Residual strains in HY100 polycrystals: comparisons of experiments and simulations. 1543-1555A
- Strain-localization in sheet metal containing a geometric defect. 1883-1886A
- Strain, Deformation effects**
- Synchrotron x-ray study of bulk lattice strains in externally loaded Cu-Mo composites. 2949-2962A
- Strain, Microstructural effects**
- Modeling of interdendritic strain and macrosegregation for dendritic solidification processes. I. Theory and experiments. 331-343B
- Modeling of interdendritic strain and macrosegregation for dendritic solidification processes. II. Computation of interdendritic strain and segregation fields in steel ingots. 345-355B
- Strain aging**
- Dynamic bake hardening of interstitial-free steels. 1375-1384A
- Strain hardening**
- Macroscopic and microscopic evolutions of a shot-peened layer during isothermal recovery. 213-224A
- Effects of microstructural parameters on work hardening of pearlite at small strains. 2665-2669A
- Strain hardening, Temperature effects**
- Mechanical behavior of a fine-grained duplex γ -TiAl alloy. 1007-1016A
- Strain rate**
- Influence of alloying elements on the strain rate and temperature dependence of the flow stress of steels. 825-830A
- Damage leading to ductile fracture under high strain-rate conditions. 831-844A
- Creep properties of Ni₃(AlTiTa) γ' phase single crystals. 1733-1740A
- Stress corrosion cracking**
- Environmentally enhanced deformation of ultra-high-purity Ni-16Cr-9Fe alloys. 2383-2388A
- Stress corrosion cracking, Temperature effects**
- Stress corrosion cracking mechanisms of Alloy 600 polycrystals and single crystals in primary water—influence of hydrogen. 2025-2036A
- Stress strain curves**
- Effect of volume fraction of SiC_p reinforcement on the processing maps for 2124 Al matrix composites. 629-639A
- The role of dispersed particles in strengthening and fracture mechanisms in a Mo-ZrC alloy processed by mechanical alloying. 715-721A
- Mechanical behavior of a fine-grained duplex γ -TiAl alloy. 1007-1016A
- Preparation and mechanical properties of highly densified nanocrystalline Al. 1017-1024A
- Effect of microstructure variations on the formation of deformation-induced martensite and associated tensile properties in a β metastable Ti alloy. 1095-1106A
- Effect of strain rate on damage evolution in a cast Al-Si-Mg base alloy. 1725-1731A
- Effects of martensite morphology and volume fraction on quasi-static and dynamic deformation behavior of dual-phase steels. 1753-1760A
- Evolution of texture and grain misorientation in an Al-Mg alloy exhibiting low-temperature superplasticity. 2169-2180A
- Analysis and prevention of yield strength drop during spiral piping of two high-strength API-X70 steels. 2669-2674A
- Stretching**
- The use of the finite-element method to design an optimized tool for the plain-strain punch stretching test. 93-98A
- Strip, Rolling**
- Mathematical modeling of the hot strip rolling of microalloyed Nb, multiply alloyed Cr-Mo, and plain C-Mn steels. 511-530A
- Strip casting**
- Mechanisms of initial melt/substrate heat transfer pertinent to strip casting. 1023-1030B
- Strontium, Alloying additive**
- The role of solute in grain refinement of magnesium. 2895-2906A
- Strontium, Extraction**
- Effect of a catalyst on the kinetics of reduction of celestite (SrSO₄) by active charcoal. 35-41B
- Structural steels, Welding**
- Characteristics of a pulsed-current, vertical-up gas metal arc weld in steel. 2247-2259A
- Fracture mechanism and toughness of the welding heat-affected zone in structural steel under static and dynamic loading. 2785-2791A
- Submerged arc welding**
- A Bayesian analysis of the influence of neutron irradiation on embrittlement in ferritic submerged arc weld metal. 445-459A
- Submerged arc welding, Quality control**
- Modeling of inclusion growth and dissolution in the weld pool. 161-169B
- Sulfur, Impurities**
- The influence of sulfur on stress-rupture fracture in Inconel 718 superalloys. 2135-2144A
- Sulfur, Reactions (chemical)**
- The thermodynamics of the Ni-Co-S ternary system. 121-128B
- Thermodynamics of surfaces and adsorption in the Fe-C-S-O system. 267-276B
- Sulfuric acid, Environment**
- Galvanic interaction between chalcopyrite and manganese dioxide in sulfuric acid medium. 55-61B
- Superalloys, Casting**
- Freckle formation and freckle criterion in superalloy castings. A model for prediction of pressure and redistribution of gas- 801-811B

- forming elements in multicomponent casting alloys.
Development of a freckle predictor via Rayleigh number method for single-crystal nickel-base superalloy castings. 1283-1292B
- Superalloys, Coating**
Effect of prealuminizing diffusion treatment on microstructural evolution of high-activity Pt-aluminide coatings. 2545-2557A
Nondestructive evaluation of residual stress for thermal barrier coated turbine blades by Cr^{3+} photoluminescence piezospectroscopy. 2037-2047A
- Superalloys, Corrosion**
Grain-boundary chemistry and intergranular corrosion in alloy 825. 2388-2391A
- Superalloys, Directional solidification**
Thermal and grain-structure simulation in a land-based turbine blade directionally solidified with the liquid metal cooling process. 1163-1173A
Directional and single-crystal solidification of Ni-base superalloys. I. The role of curved isotherms on grain selection. 1293-1304B
Directional and single-crystal solidification of Ni-base superalloys. II. Coincidence site lattice character of grain boundaries. 2877-2886A
- Superalloys, Extrusion**
Hot deformation mechanisms in a powder metallurgy nickel-base superalloy IN 625. 2887-2893A
- Superalloys, Mechanical properties**
Fatigue crack path prediction in Udimet 720 nickel-based alloy single crystals. 2317-2325A
Effect of plastic anisotropy on the creep strength of single crystals of a nickel-based superalloy. 109-123A
Infrared temperature mapping of UTMET alloy during high-cycle fatigue tests. 421-430A
The influence of Mg on creep properties and fracture behaviors of Mar-M247 superalloy under 1255 K/200 MPa. 1307-1310A
Creep-behavior modeling of the single-crystal superalloy CMSX-4. 1365-1373A
The effect of high-temperature oxidation on the creep behavior of a superalloy (Nimonic-105). 1401-1411A
Stress corrosion cracking mechanisms of Alloy 600 polycrystals and single crystals in primary water—influence of hydrogen. 1777-1784A
The influence of sulfur on stress-rupture fracture in Inconel 718 superalloys. 2025-2036A
On the primary creep of CMSX-4 superalloy single crystals. 2135-2144A
Environmentally enhanced deformation of ultra-high-purity Ni-16Cr-9Fe alloys. 2219-2228A
- Superalloys, Microstructure**
Investigation on the cold deformation strengthening mechanism in MP 159 alloy. 2383-2388A
Influence of solidification variables on the dendrite arm spacings of Ni-based superalloys. 5-13A
Determining the three-dimensional morphology of γ' -particles in γ - γ' superalloys. 546-551B
- Superalloys, Oxidation**
Selective oxidation and internal nitridation during high-temperature exposure of single-crystalline nickel-base superalloys. 1333-1342A
- Superalloys, Phase transformations**
Computer simulation of the initial rafting process of a nickel-base single-crystal superalloy. 47-56A
- Superalloys, Phases (state of matter)**
Liquidus temperature determination in multicomponent alloys by thermal analysis. 585-597A
- Superalloys, Welding**
A process model for the distortion induced by the electron-beam welding of a nickel-based superalloy. 497-501A
- Superconductors, Crystal growth**
Morphological stability of Sm123 superconductor during peritectic solidification from $\text{Sm211} + \text{L}$ mixture. 2261-2273A
- Superplastic forming**
An analysis of the effect of cavity nucleation rate and cavity coalescence on the tensile behavior of superplastic materials. 141-149B
Superplastic forming of duplex stainless steel. 1425-1434A
- Superplasticity**
An analysis of the effect of cavity nucleation rate and cavity coalescence on the tensile behavior of superplastic materials. 2394-2396A
Superplastic forming of duplex stainless steel. 1425-1434A
- Superplasticity, Composition effects**
Effect of volume fraction of SiC_2 reinforcement on the processing maps for 2124 Al matrix composites. 2394-2396A
- Superplasticity, Deformation effects**
Evolution of texture and grain misorientation in an Al-Mg alloy exhibiting low-temperature superplasticity. 629-639A
Interpretation of microstructural evolution using dynamic materials modeling. 2169-2180A
- Superplasticity, Microstructural effects**
Correlation between former alpha boundary growth kinetics and superplastic flow in Zn-22% Al. 2973-2974A
- Surface alloying**
Theoretical and experimental investigations of electron beam surface remelting and alloying. 163-172A
Microstructural analysis of vanadium carbide/steel surface-alloyed materials fabricated by high-energy electron-beam irradiation. 1405-1417B
Surface amorphous and crystalline microstructure by alloying zirconium using Nd:YAG pulsed laser. 2849-2855A
- Surface defects**
Depth of oscillation marks forming in continuous casting of steel. 3123-3127A
- Surface pretreatments**
Effect of prealuminizing diffusion treatment on microstructural evolution of high-activity Pt-aluminide coatings. 813-826B
- Surface structure, Deformation effects**
Macroscopic and microscopic evolutions of a shot-peened layer during isothermal recovery. 2037-2047A
- Surface structure, Heating effects**
Microstructural and compositional evolution of compound layers during gaseous nitrocarburizing. 213-224A
Erratum: Microstructural and compositional evolution of compound layers during gaseous nitrocarburizing. 195-211A
Study of microstructure of low-temperature plasma-nitrided AISI 304 stainless steel. 801A
- Surface tension**
Thermodynamics of surfaces and adsorption in the Fe-C-S-O system. 1193-1199A
The surface tensions and foaming behavior of melts in the system CaO-FeO-SiO_2 . 267-276B
- Surface tension, Field effects**
Surface tension of molten silicon measured by the electromagnetic levitation method under microgravity. 921-925B
- Tailored blanks, Welding**
Weld metal ductility in aluminum tailor welded blanks. 1585-1589A
- Tantalum, Alloying additive**
Creep properties of $\text{Ni}_3(\text{AlTiTa})$ γ' phase single crystals. 2755-2763A
- Tantalum, Diffusion**
Pseudobinary diffusion coefficients in the Ti-Mo-Ta system. 1733-1740A
- Tantalum, Mechanical properties**
Comparison between high and low strain-rate deformation of tantalum. 3198-3199A
Quantitative description of damage evolution in ductile fracture of tantalum. 815-823A
- Tantalum compounds, Composite materials**
Development of a thermodynamic database for cemented carbides for design and processing simulations. 845-851A
- Tapes (metallic), Mechanical properties**
Effect of fiber volume fraction on the fracture behavior of Nb-1 wt.% Zr/218W composites at elevated temperatures. 615-619B
- Tearing**
Two-phase modeling of mushy zone parameters associated with hot tearing. 873-887A
- Technology transfer**
Aspects of technology transfer. 1461-1472A
- Temperature control**
Physical and mathematical models of steel flow and heat transfer in a tundish heated by plasma. 1153-1162B
- Temperature distribution, Cooling effects**
Determination of thermophysical properties and boundary conditions of direct chill-cast aluminum alloys using inverse methods. 63-74B
- Temperature distribution, Welding effects**
Thermal analysis of the arc welding process. I. General solutions. 1627-1634A
- Tempering**
Insight into the microstructural characterization of ferritic steel using micromagnetic parameters. 1353-1370B
- Tensile properties, Deformation effects**
Equal-channel angular pressing of commercial aluminum alloys: grain refinement, thermal stability and tensile properties. 1053-1065A
- Tensile strength**
Effect of microstructure variations on the formation of deformation-induced martensite and associated tensile properties in a β metastable Ti alloy. 691-701A
Creep-behavior modeling of the single-crystal superalloy CMSX-4. 1095-1106A
- Tensile strength, Alloying effects**
A comparison study of microstructure and mechanical properties of Ti-24Al-14Nb-3V-0.5Mo with and without Si. 1401-1411A
- Tensile strength, Composition effects**
Microstructure and properties of in situ Al/TiB₂ composite fabricated by in-melt reaction method. 2205-2217A
- Tensile strength, Deformation effects**
The effect of matrix microstructure on the tensile and fatigue behavior of SiC particle-reinforced 2080 Al matrix composites. 1959-1964A
- Tensile strength, Impurity effects**
The influence of sulfur on stress-rupture fracture in Inconel 718 superalloys. 531-540A
- Tensile strength, Microstructural effects**
Correlation of the microstructure and fracture toughness of the heat-affected zones of an SA 508 steel. 2135-2144A
An investigation of the effect of fatigue deformation on the residual mechanical properties of Ti-6Al-4V ELI. 1107-1119A
The effect of processing and microstructure development on the slip and fracture behavior of the 2.1 wt.% Li AF/C-489 and 1.8 wt.% Li AF/C-458 Al-Li-C-X alloys. 1937-1948A
- Tensile strength, Processing effects**
Effects of strain rate and anisotropy on the tensile deformation properties of extruded AlZnMg alloys. 1965-1976A
The role of dispersed particles in strengthening and fracture mechanisms in a Mo-ZrC alloy processed by mechanical 669-678A

- alloying. 715-721A
- Preparation and mechanical properties of highly densified nanocrystalline Al. 1017-1024A
- Reaction synthesis, microstructure, and mechanical properties of in situ composite NiAl-Al₂O₃-TiC. 1692-1695A
- Tensile stress-strain analysis of single-structure steels. 1785-1794A
- Characteristics of Mg-based composites synthesized using a novel mechanical disintegration and deposition technique. 1873-1881A
- Microstructure and mechanical behavior of spray-deposited Al-Cu-Mg-(Ag-Mn) alloys. 2287-2298A
- Tensile strength, Welding effects**
- Friction-stir welding effects on microstructure and fatigue of aluminum alloy 7050-T7451. 2181-2192A
- Characteristics of a pulsed-current, vertical-up gas metal arc weld in steel. 2247-2259A
- Ternary systems, Phase transformations**
- Enthalpy of mixing of liquid Ni-Zr and Cu-Ni-Zr alloys. 277-284B
- Transient liquid-phase bonding in two-phase ternary systems. 1187-1192A
- Examination of solidification pathways and the liquidus surface in the Nb-Ti-Al system. 1305-1321B
- Ternary systems, Phases (state of matter)**
- The prediction of the hydriding thermodynamics of Pd-Rh-Co ternary alloys. 667-673B
- Tin-silver-copper eutectic temperature and composition. 1155-1162A
- The 900°C isothermal section of Ti-Ni-V alloys. 1679-1682A
- Experimental investigation and thermodynamic modeling of the Cr-Ni-Si system. 1795-1803A
- Texture**
- The influence of crystallographic texture and interstitial impurities on the mechanical behavior of zirconium. 1997-2003A
- Microstructure-ultrasonic inspectability relationships in Ti6242: signal-to-noise in fine-grain-processed Ti6242. 2119-2125A
- Evolution of texture and grain misorientation in an Al-Mg alloy exhibiting low-temperature superplasticity. 2169-2180A
- Dynamic materials testing, texture, and yield-surface calculation of an automotive sheet steel. 2439-2448A
- Yield vertices for {123}<111> multiple slip. 2449-2456A
- Texture, Deformation effects**
- Texture and residual strain in two SiC/Ti-6-2-4-2 titanium composites. 889-898A
- Load sharing between austenite and ferrite in a duplex stainless steel during cyclic loading. 1557-1570A
- Evolution of texture in the β (B2) phase of a two phase titanium aluminide intermetallic alloy Ti-24Al-11Nb. 2339-2350A
- Texture, Heating effects**
- Effect of intermediate annealing on texture evolution and plastic anisotropy in an Al-Mg autobody alloy. 99-107A
- Texture, Processing effects**
- Directional and single-crystal solidification of Ni-base superalloys. I. The role of curved isotherms on grain selection. 2877-2886A
- Directional and single-crystal solidification of Ni-base superalloys. II. Coincidence site lattice character of grain boundaries. 2887-2893A
- Thermal analysis**
- Liquidus temperature determination in multicomponent alloys by thermal analysis. 497-501A
- Thermal barriers, Coatings**
- Nondestructive evaluation of residual stress for thermal barrier coated turbine blades by Cr³⁺ photoluminescence piezospectroscopy. 2388-2391A
- Thermal conductivity**
- A model of the interfacial heat-transfer coefficient during unidirectional solidification of an aluminum alloy. 285-295B
- Determination of thermophysical properties and boundary conditions of direct chill-cast aluminum alloys using inverse methods. 1627-1634A
- Thermal cycling**
- Enhanced densification of cavitated dispersion-strengthened aluminum by thermal cycling. 2647-2657A
- Effects of thermal cycling on the kinetics of the $\gamma \rightarrow \epsilon$ martensitic transformation in an Fe-17 wt.% Mn alloy. 2735-2738A
- Thermal expansion, Composition effects**
- Thermal expansion behavior of silver matrix composites. 291-298A
- Characterization of Mo-SiO₂ functionally graded materials. 299-308A
- Effect of albite particles on the coefficient of thermal expansion behavior of the Al6061 alloy composites. 773-780A
- Effect of particle-size distribution on the properties of high-volume-fraction SiC_p-Al-based composites. 2351-2359A
- Chemical synthesis and characterization of low thermal expansion-high conductivity Cu-Mo and Ag-Mo composites. 2396-2398A
- Thermal fatigue**
- Modeling thermomechanical fatigue life of high-temperature titanium alloy IMI 834. 431-444A
- Modeling creep and fatigue of copper alloys. 2491-2502A
- Thermal stability**
- Grain-boundary chemistry and intergranular corrosion in alloy 825. 1163-1173A
- Thermal stability, Coating effects**
- Thermal stability of electroless-nickel/solder interface: A. Interfacial chemistry and microstructure. 2857-2866A
- Thermal stability of electroless-nickel/solder interface: B. Interfacial fatigue resistance. 2867-2875A
- Thermal stability, Deformation effects**
- Equal-channel angular pressing of commercial aluminum alloys: grain refinement, thermal stability and tensile properties. 691-701A
- Thermodynamics**
- Estimation of viscosities of ternary silicate melts using the excess Gibbs energy of mixing. 105-109B
- The thermodynamics of the Ni-Co-S ternary system. 121-128B
- Thermodynamics of surfaces and adsorption in the Fe-C-S-O system. 267-276B
- Thermodynamic-kinetic simulation of constrained dendrite growth in steels. 365-379B
- Electrode potential studies of liquid-solid equilibrium in Na₃Bi-saturated Na-Bi melts. 411-414B
- The effect of lead on the activity of sodium in liquid zinc. 414-418B
- Thermodynamic study of zinc-rich zinc-sodium alloys. 419-424B
- Fundamental theories and concepts for predicting thermodynamic properties of high temperature ionic and metallic liquid solutions and vapor molecules. 579-586B
- Ideal and cooperative bond-lattice representations of excitations in glass-forming liquids: excitation profiles, fragilities, and phase transitions. 587-596B
- Prediction of properties of intermetallics using a chemical bonding model. 603-607B
- Solutions of iron oxides in molten cryolite. 609-613B
- Development of a thermodynamic database for cemented carbides for design and processing simulations. 615-619B
- Coupled experimental and thermodynamic modeling studies for metallurgical smelting and coal combustion slag systems. 621-630B
- Solubilities and Raman spectra of NdOCl in some chloride melts of interest for the electrowinning of magnesium from its oxide. 631-639B
- The power of thermodynamic modeling: examples from molten halide mixtures. 641-650B
- The modified quasichemical model I—binary solutions. 651-659B
- Thermodynamic and nonstoichiometric behavior of promising Hf-Tc cuprate systems via electromotive force measurements: a short review. 661-666B
- The prediction of the hydriding thermodynamics of Pd-Rh-Co ternary alloys. 667-673B
- Phase equilibrium and minor element distribution between FeO₂-SiO₂-MgO-based slag and Cu₂S-FeS matte at 1573K under high partial pressures of SO₂. 705-712B
- Activity measurement of the constituents in liquid Cu-Mg and Cu-Ca alloys with mass spectrometry. 927-935B
- Quantifying the heats of coal devolatilization. 1125-1131B
- Experimental study of phase equilibria in the systems Fe-Zn-O and Fe-Zn-Si-O at metallic iron saturation. 1195-1201B
- Modified predominance diagrams for gas-solid reactions. 1429-1437B
- A Scheil-Gulliver model with back-diffusion applied to the microsegregation of chromium in Fe-Cr-C alloys. 1682-1684A
- Experimental investigation and thermodynamic modeling of the Cr-Ni-Si system. 1795-1803A
- Modeling of dissolution, growth, and coarsening of aluminum nitride in low-carbon steels. 1907-1916A
- Transient liquid-phase bonding in the Ni-Al-B system. 2835-2847A
- Thermomechanical treatment**
- Evolution of texture and grain misorientation in an Al-Mg alloy exhibiting low-temperature superplasticity. 2169-2180A
- Evolution of texture in the β (B2) phase of a two phase titanium aluminide intermetallic alloy Ti-24Al-11Nb. 2339-2350A
- Microstructural development and austempering kinetics of ductile iron during thermomechanical processing. 2575-2585A
- Thermomechanical treatment, Composition effects**
- The effect of matrix microstructure on the tensile and fatigue behavior of SiC particle-reinforced 2080 Al matrix composites. 531-540A
- Thin films, Bonding**
- The role of plasticity in bimaterial fracture with ductile interlayers. 863-872A
- Thin films, Crystal growth**
- Application of the phase-field method to the solidification of hot-dipped galvanized coatings. 487-495A
- Tin, Binary systems**
- A numerical and experimental study of the rate of transformation in three directionally grown peritectic systems. 29-34A
- A model of convection-induced oscillatory structure formation in peritectic alloys. 1233-1246A
- Tin, Casting**
- Finding boundary conditions: a coupling strategy for the modeling of metal casting processes. I. Experimental study and correlation development. 75-86B
- Finding boundary conditions: a coupling strategy for the modeling of metal casting processes. II. Numerical study and analysis. 87-96B
- Tin, Diffusion**
- Interdiffusion of Sn and Pb in liquid Pb-Sn alloys. 1343-1352A
- Tin, Ternary systems**
- Tin-silver-copper eutectic temperature and composition. 1155-1162A
- Tin base alloys, Crystal growth**
- Solidification parameters during the columnar-to-equiaxed transition in lead-tin alloys. 1611-1625A
- Tin base alloys, Directional solidification**
- Effect of computational domain size on the mathematical modeling of transport processes and segregation during directional solidification. 3129-3135A
- Tin base alloys, Phases (state of matter)**
- Tin-silver-copper eutectic temperature and composition. 1155-1162A
- Tin base alloys, Physical properties**
- Thin-wall back extrusion of partially remelted semi-solid Sn-Pb. 57-62A
- Tin base alloys, Powder technology**
- Monosize droplet deposition as a means to investigate droplet behavior during spray deposition. 1333-1344B

- Titanium, Alloying additive**
Creep properties of $\text{Ni}_3(\text{AlTiTa})$ γ phase single crystals. 1733-1740A
Relation between microstructure, composition, and hot cracking in Ti-stabilized austenitic stainless steel weldments. 3109-3122A
- Titanium, Binary systems**
Evaporation behavior of aluminum during the cold crucible induction skull melting of titanium aluminum alloys. 837-844B
- Titanium, Diffusion**
Pseudobinary diffusion coefficients in the Ti-Mo-Ta system. 3198-3199A
- Titanium, Extraction**
Reduction of titania by methane-hydrogen-argon gas mixture. 129-139B
Contactless electrochemical reduction of titanium (II) chloride by aluminum. 713-721B
A model for the role of carbon on carbochlorination of TiO_2 . 1439-1446B
- Titanium, Mechanical properties**
Effects of inert gases on fatigue crack growth and their transportation into subsurface regions in titanium. 1435-1441A
- Titanium, Ternary systems**
Examination of solidification pathways and the liquidus surface in the Nb-Ti-Al system. 1305-1321B
The 900°C isothermal section of Ti-Ni-V alloys. 1679-1682A
- Titanium base alloys, Casting**
Aluminum volatilization and inclusion removal in the electron beam cold hearth melting of Ti alloys. 845-854B
Alpha case thickness modeling in investment castings. 1419-1427B
- Titanium base alloys, Coating**
The influence of additions of Nb and Cr on the aluminizing behavior of TiAl alloy. 2391-2394A
- Titanium base alloys, Composite materials**
Chemically induced reduction: a viable process for synthesizing γ -TiAl based intermetallic matrix composite powders containing nanocrystalline TiC. 151-159B
Creep expansion of porous Ti-6Al-4V sandwich structures. 261-273A
Phase transitions in reactive formation of $\text{Ti}_5\text{Si}_3/\text{TiAl}$ in situ composites. 763-771A
Texture and residual strain in two SiC/Ti-6-2-4-2 titanium composites. 889-898A
Mechanisms, models and simulations of metal-coated fiber consolidation. 1271-1282A
High-temperature fracture and fatigue-crack growth behavior of an XD gamma-based titanium aluminide intermetallic alloy. 1413-1423A
Fatigue crack growth resistance of unidirectional fiber-reinforced titanium metal-matrix composites under transverse loading. 2083-2092A
Design and fabrication of W-Mo-Ti-TiAl-Al system functionally graded material. 2369-2376A
Effect of interfacial debonding and sliding on matrix crack initiation during isothermal fatigue of SCS-6/Ti-15-3 composites. 2637-2645A
- Titanium base alloys, Diffusion**
Hydrogen diffusion coefficients in the titanium alloys IMI 834, Ti 10-2-3, Ti 21 S, and Alloy C. 1507-1517A
- Titanium base alloys, Mechanical properties**
The fracture resistance of a binary TiAl alloy. 71-80A
Part II. Metallurgical factors governing the H-assisted intergranular cracking of peak-aged Ti-3Al-8V-6Cr-4Mo-4Zr (Beta-C). 81-92A
Modeling thermomechanical fatigue life of high-temperature titanium alloy IMI 834. 431-444A
Effect of mean stress (stress ratio) and aging on fatigue-crack growth in a metastable beta titanium alloy, Ti-10V-2Fe-3Al. 703-714A
Simulation of shear plugging through thin plates using the GRIM Eulerian hydrocode. 853-860A
Mechanical behavior of a fine-grained duplex γ -TiAl alloy. 1007-1016A
Effect of microstructure variations on the formation of deformation-induced martensite and associated tensile properties in a β metastable Ti alloy. 1095-1106A
Role of foreign-object damage on thresholds for high-cycle fatigue in Ti-6Al-4V. 1571-1583A
The effect of impact damage on the room-temperature fatigue behavior of γ -TiAl. 1741-1752A
An investigation of the effect of fatigue deformation on the residual mechanical properties of Ti-6Al-4V ELI. 1937-1948A
Effects of microstructure on the short fatigue crack initiation and propagation characteristics of biomedical α/β titanium alloys. 1949-1958A
A comparison study of microstructure and mechanical properties of Ti-24Al-14Nb-3V-0.5Mo with and without Si. 2205-2217A
Creep deformation of TiAl-Si alloys with aligned γ/α_2 lamellar microstructures. 2463-2473A
Cyclic deformation, dislocation structure, and internal fatigue crack generation in a Ti-Fe-O alloy at liquid nitrogen temperature. 2793-2805A
Constitutive properties of hard-alpha titanium. 3029-3040A
Dynamic fracture toughness of a Ti-45Al-1.6Mn alloy at high temperature. 3053-3061A
- Titanium base alloys, Microstructure**
Microstructure-ultrasonic inspectability relationships in Ti6242: signal-to-noise in fine-grain-processed Ti6242. 2119-2125A
Evolution of texture in the $\beta(\text{B2})$ phase of a two phase titanium aluminide intermetallic alloy Ti-24Al-11Nb. 2339-2350A
Discussion of "Surface relief and the displacive transformation to the lamellar microstructure in TiAl" and "Nanometer-scale, fully lamellar microstructure in an aged TiAl-based alloy". 2377-2379A
Author's reply to: Discussion of "Surface relief and the displacive transformation to the lamellar microstructure in TiAl" and "Nanometer-scale, fully lamellar microstructure in an aged TiAl-based alloy". 2379-2383A
Interaction of deformation twin and 120°-rotational order fault domain boundary in the lamellar structure of two-phase TiAl-based alloys. 2823-2834A
- Titanium base alloys, Phase transformations**
Surface relief of α' martensite in a Ti-Mo alloy. 599-605A
Evaporation behavior of aluminum during the cold crucible induction skull melting of titanium aluminum alloys. 837-844B
- Titanium base alloys, Powder technology**
Modeling the reaction synthesis of shock-densified titanium-silicon powder mixture compacts. 307-316B
Preparation of high porosity metal foams. 1345-1352B
Microstructural evolution in wire-drawn Ti-22Al-26Nb powder. 2931-2941A
- Titanium carbide, Coatings**
Correlation of microstructure with the wear resistance and fracture toughness of hardfacing alloys reinforced with complex carbides. 3041-3052A
- Titanium carbide, Composite materials**
Chemically induced reduction: a viable process for synthesizing γ -TiAl based intermetallic matrix composite powders containing nanocrystalline TiC. 151-159B
Reaction synthesis, microstructure, and mechanical properties of in situ composite NiAl-Al₂O₃-TiC. 1692-1695A
- Titanium compounds, Coating**
The influence of additions of Nb and Cr on the aluminizing behavior of TiAl alloy. 2391-2394A
- Titanium compounds, Composite materials**
Chemically induced reduction: a viable process for synthesizing γ -TiAl based intermetallic matrix composite powders containing nanocrystalline TiC. 151-159B
Development of a thermodynamic database for cemented carbides for design and processing simulations. 615-619B
Phase transitions in reactive formation of $\text{Ti}_5\text{Si}_3/\text{TiAl}$ in situ composites. 763-771A
High-temperature fracture and fatigue-crack growth behavior of an XD gamma-based titanium aluminide intermetallic alloy. 1413-1423A
Design and fabrication of W-Mo-Ti-TiAl-Al system functionally graded material. 2369-2376A
- Titanium compounds, Mechanical properties**
The fracture resistance of a binary TiAl alloy. 71-80A
Mechanical behavior of a fine-grained duplex γ -TiAl alloy. 1007-1016A
The effect of impact damage on the room-temperature fatigue behavior of γ -TiAl. 1741-1752A
A comparison study of microstructure and mechanical properties of Ti-24Al-14Nb-3V-0.5Mo with and without Si. 2205-2217A
Creep deformation of TiAl-Si alloys with aligned γ/α_2 lamellar microstructures. 2463-2473A
Experimental studies on tribological properties of pseudoelastic TiNi alloy with comparison to stainless steel 304. 2773-2783A
Dynamic fracture toughness of a Ti-45Al-1.6Mn alloy at high temperature. 3053-3061A
- Titanium compounds, Microstructure**
Evolution of texture in the $\beta(\text{B2})$ phase of a two phase titanium aluminide intermetallic alloy Ti-24Al-11Nb. 2339-2350A
Discussion of "Surface relief and the displacive transformation to the lamellar microstructure in TiAl" and "Nanometer-scale, fully lamellar microstructure in an aged TiAl-based alloy". 2377-2379A
Author's reply to: Discussion of "Surface relief and the displacive transformation to the lamellar microstructure in TiAl" and "Nanometer-scale, fully lamellar microstructure in an aged TiAl-based alloy". 2379-2383A
Interaction of deformation twin and 120°-rotational order fault domain boundary in the lamellar structure of two-phase TiAl-based alloys. 2823-2834A
- Titanium compounds, Oxidation**
Diffusion of oxygen in the Al₂O₃ oxidation product of TiAl₃. 3023-3028A
- Titanium compounds, Phase transformations**
Experimental investigation and thermodynamic calculation of the Ti-Ni-Cu shape memory alloys. 2423-2430A
- Titanium compounds, Powder technology**
Modeling the reaction synthesis of shock-densified titanium-silicon powder mixture compacts. 307-316B
Synthesis of MoSi₂-TiSi₂ pseudobinary alloys by reactive sintering. 747-753A
Microstructural evolution in wire-drawn Ti-22Al-26Nb powder. 2931-2941A
- Titanium diboride, Coatings**
Mechanical properties of laser-deposited composite boride coating using nanoindentation. 401-408A
Elevated temperature oxidation of laser surface engineered composite boride coating on steel. 461-473A
- Titanium diboride, Composite materials**
Particulate penetration into solid droplets. 387-396A
Reaction steps in the combustion synthesis of NiAl/TiB₂ composites. 433-438B
High-temperature fracture and fatigue-crack growth behavior of an XD gamma-based titanium aluminide intermetallic alloy. 1413-1423A
Microstructure and properties of in situ Al/TiB₂ composite fabricated by in-melt reaction method. 1959-1964A
- Titanium dioxide, Reactions (chemical)**
A model for the role of carbon on carbochlorination of TiO_2 . 1439-1446B
- Titanium dioxide, Reduction (chemical)**
Reduction of titania by methane-hydrogen-argon gas mixture. 129-139B
- Titanium nitride, Composite materials**
The influence of reinforcement particle size distribution on the mechanical behavior of a stainless steel/TiN composite. 309-318A
- Titanium nitride, Impurities**
The mechanism of brittle fracture in a microalloyed steel. I. Inclusion-induced cleavage. 641-652A
The mechanism of brittle fracture in a microalloyed steel. II. Mechanistic modeling. 653-667A

- Length change and deformation of powder injection-molded compacts during solvent debinding. 1473-1478A
- Tool steels, Coatings**
On the evolution of porosity in spray-deposited tool steels. 723-733A
- Tool steels, Heat treatment**
Theoretical and experimental investigations of electron beam surface remelting and alloying. 1405-1417B
- Tool steels, Mechanical properties**
Influence of alloying elements on the strain rate and temperature dependence of the flow stress of steels. 825-830A
- Tool steels, Phase transformations**
Quantitative approach to coagulation, coalescence, and polygonization of carbides in the NCWV/D3 tool steel. 2661-2665A
- Torsion, Processing effects**
Correlation of microstructure with dynamic deformation behavior and penetration performance of tungsten heavy alloys fabricated by mechanical alloying. 2475-2489A
- Toughness**
The role of plasticity in bimaterial fracture with ductile interlayers. 863-872A
- Toughness, Alloying effects**
Effects of boron doping on the grain-growth kinetics and mechanical properties of γ/γ' nickel-aluminum alloys. 3179-3186A
- Toughness, Composition effects**
Characterization of Mo-SiO₂ functionally graded materials. The influence of reinforcement particle size distribution on the mechanical behavior of a stainless steel/TiN composite. 299-308A
309-318A
- Transgranular fracture**
A model for creep-fatigue interaction in terms of crack-tip stress relaxation. 1761-1775A
- Transgranular fracture, Alloying effects**
Effects of boron doping on the grain-growth kinetics and mechanical properties of γ/γ' nickel-aluminum alloys. 3179-3186A
- Transgranular fracture, Processing effects**
Preparation and mechanical properties of highly densified nanocrystalline Al. 1017-1024A
- Transition joints, Physical properties**
Unsteady Marangoni flow in a molten pool when welding dissimilar metals. 1387-1403B
- Transition metal compounds, Electrochemistry**
Prediction of properties of intermetallics using a chemical bonding model. 603-607B
- Tribology**
Experimental studies on tribological properties of pseudoelastic TiNi alloy with comparison to stainless steel 304. 2773-2783A
- Tribology, Processing effects**
Tribological properties of centrifugally cast copper alloy-graphite particle composite. 1283-1293A
- TTT curves**
Mechanical properties, microstructural stability and kinetics of α -phase formation in 29Cr-6Ni-2Mo-0.38N superduplex stainless steel. 35-45A
Modeling of inclusion growth and dissolution in the weld pool. 161-169B
Application of, and precautions for the use of, the Rule of Additivity in phase transformation. 675-682B
- Tubes, Mechanical properties**
Anisotropy of yielding in a Zr-2.5Nb pressure tube material. Strain-localization in sheet metal containing a geometric defect. 409-420A
1883-1886A
- Tubes, Quality control**
A process model for the heat-affected zone microstructure evolution in duplex stainless steel weldments. II. Application to electron beam welding. 1035-1048A
- Tungsten, Alloying additive**
Role of Mo and W during sensitization of superaustenitic stainless steel—crystallography and composition of precipitates. 1893-1905A
- Tungsten, Bonding**
The role of plasticity in bimaterial fracture with ductile interlayers. 863-872A
- Tungsten, Composite materials**
Reactive infiltration processing and secondary compressive creep of NiAl and NiAl-W composites. 781-792A
Effect of fiber volume fraction on the fracture behavior of Nb-1 wt.% Zr/218W composites at elevated temperatures. 873-887A
Design and fabrication of W-Mo-Ti-TiAl-Al system functionally graded material. 2369-2376A
- Tungsten base alloys, Mechanical properties**
Correlation of microstructure with dynamic deformation behavior and penetration performance of tungsten heavy alloys fabricated by mechanical alloying. 2475-2489A
- Tungsten base alloys, Phase transformations**
The effect of gravity on solution-precipitation during liquid phase sintering. 397-400A
- Tungsten base alloys, Powder technology**
Microstructural parameters related to liquid-phase sintering. Simulation of percolation structure of grain bonding in liquid-phase sintering by three-dimensional grain structure reconstruction. 2607-2614A
3187-3193A
- Tungsten carbide, Coatings**
Correlation of microstructure with the wear resistance and fracture toughness of hardfacing alloys reinforced with complex carbides. 3041-3052A
- Tungsten carbide, Composite materials**
Anisotropic grain growth based on the atomic adsorption model in WC-25% Co alloy. 1925-1935A
- Tungsten compounds, Composite materials**
Development of a thermodynamic database for cemented carbides for design and processing simulations. 615-619B
- Turbine blades, Coating**
Nondestructive evaluation of residual stress for thermal barrier coated turbine blades by Cr³⁺ photoluminescence piezospectroscopy. 2388-2391A
- Turbine blades, Directional solidification**
Thermal and grain-structure simulation in a land-based turbine blade directionally solidified with the liquid metal cooling process. 1293-1304B
- Turbine blades, Mechanical properties**
The effect of impact damage on the room-temperature fatigue behavior of γ -TiAl. 1741-1752A
On the primary creep of CMSX-4 superalloy single crystals. 2219-2228A
- Turbulence**
Melt flow control in a multistrand tundish using a turbulence inhibitor. 1505-1515B
- Turbulent flow**
Modeling of turbulent flow in electromagnetically levitated metal droplets. 171-178B
- Twin roll casting**
Measurements, simulations, and analyses of instantaneous heat fluxes from solidifying steels to the surfaces of twin roll casters and of aluminum to plasma-coated metal substrates. 1031-1047B
- Twinning**
Island grains of low misorientation angles formed during abnormal grain growth in Cu. 1489-1491A
The influence of crystallographic texture and interstitial impurities on the mechanical behavior of zirconium. 1997-2003A
Interaction of deformation twin and 120°-rotational order fault domain boundary in the lamellar structure of two-phase TiAl-based alloys. 2823-2834A
- Twinning, Deformation effects**
Investigation on the cold deformation strengthening mechanism in MP 159 alloy. 5-13A
- Ultrasonic testing**
Microstructure-ultrasonic inspectability relationships in Ti6242: signal-to-noise in fine-grain-processed Ti62642. 2119-2125A
- Vacuum oxygen decarburizing**
Modeling of the vacuum oxygen decarburization refining process. 197-206B
- Vanadium, Composite materials**
An investigation of the effects of ductile-layer thickness on the fracture behavior of nickel aluminide microlaminates. 1385-1399A
- Vanadium, Ternary systems**
The 900°C isothermal section of Ti-Ni-V alloys. 1679-1682A
- Vanadium carbide, Alloying additive**
Microstructural analysis of vanadium carbide/steel surface-alloyed materials fabricated by high-energy electron-beam irradiation. 2849-2855A
- Viscosity**
Viscosity of a CaO-MgO-Al₂O₃-SiO₂ melt containing spinel particles at 1646K. 97-104B
Estimation of viscosities of ternary silicate melts using the excess Gibbs energy of mixing. 105-109B
Estimation of liquidus temperatures for multicomponent silicates from activation energies for viscous flow. 111-119B
- Viscous flow**
Estimation of liquidus temperatures for multicomponent silicates from activation energies for viscous flow. 111-119B
- Volatility**
Quantifying the heats of coal devolatilization. 1125-1131B
- Volume fraction**
Effect of fiber volume fraction on the fracture behavior of Nb-1 wt.% Zr/218W composites at elevated temperatures. 873-887A
Influence of microstructure on the flow behavior of duplex stainless steels at high temperatures. 1353-1364A
Effects of martensite morphology and volume fraction on quasi-static and dynamic deformation behavior of dual-phase steels. 1753-1760A
The effect of processing and microstructure development on the slip and fracture behavior of the 2.1 wt.% Li AF/C-489 and 1.8 wt.% Li AF/C-458 Al-Li-C-X alloys. 1965-1976A
Fatigue crack growth resistance of unidirectional fiber-reinforced titanium metal-matrix composites under transverse loading. 2083-2092A
Effect of particle-size distribution on the properties of high-volume-fraction SiC_z-Al-based composites. 2351-2359A
Strength and ductility of heavily drawn bundled Cu-Nb filamentary microcomposite wires with various Nb contents. 2457-2462A
Influence of elastic inclusion morphology and matrix hardening behavior on Bauschinger effect in metal matrix composites. 2943-2948A
- Volume fraction, Welding effects**
Correlation of the microstructure and fracture toughness of the heat-affected zones of an SA 508 steel. 1107-1119A
- Waste disposal**
Phase diagram study for the alkali metal-oxychloride system. Grain-boundary chemistry and intergranular corrosion in alloy 825. 795-799B
1163-1173A
- Water vapor, Environment**
The effect of water vapor on mold slag crystallization. 403-406B
- Wear mechanisms**
Identification of rolling-sliding damage mechanisms in porous

- alloys. 3091-3099A
- Wear resistance**
Experimental studies on tribological properties of pseudoelastic TiNi alloy with comparison to stainless steel 304. 2773-2783A
- Wear resistance, Coating effects**
Correlation of microstructure with the wear resistance and fracture toughness of hardfacing alloys reinforced with complex carbides. 3041-3052A
Surface amorphous and crystalline microstructure by alloying zirconium using Nd:YAG pulsed laser. 3123-3127A
- Wear resistance, Processing effects**
Tribological properties of centrifugally cast copper alloy-graphite particle composite. 1283-1293A
- Weld metal, Mechanical properties**
A Bayesian analysis of the influence of neutron irradiation on embrittlement in ferritic submerged arc weld metal. 445-459A
- Weld metal, Microstructure**
Microstructural characterization and analysis of inclusions in C-Mn steel and weld metals. 615-628A
- Weld metal, Phase transformations**
Microstructural evolution in ultra-low-carbon steel weldments. I. Controlled thermal cycling and continuous cooling transformation diagram of the weld metal. 2145-2153A
- Weld metal pool**
Mathematical modeling of the dynamic behavior of gas tungsten arc weld pools. 1465-1473B
- Weld metal pool, Solubility**
Modeling of inclusion growth and dissolution in the weld pool. 161-169B
- Welded joints, Mechanical properties**
A Bayesian analysis of the influence of neutron irradiation on embrittlement in ferritic submerged arc weld metal. 445-459A
The mechanism of brittle fracture in a microalloyed steel. I. Inclusion-induced cleavage. 641-652A
The mechanism of brittle fracture in a microalloyed steel. II. Mechanistic modeling. 653-667A
Correlation of the microstructure and fracture toughness of the heat-affected zones of an SA 508 steel. 1107-1119A
Creep deformation and fracture behavior of types 316 and 316L(N) stainless steels and their weld metals. 1175-1185A
Friction-stir welding effects on microstructure and fatigue of aluminum alloy 7050-T7451. 2181-2192A
Characteristics of a pulsed-current, vertical-up gas metal arc weld in steel. 2247-2259A
Improved microstructure and properties of 6061 aluminum alloy weldments using a double-sided arc welding process. 2537-2543A
Weld metal ductility in aluminum tailor welded blanks. 2755-2763A
Fracture mechanism and toughness of the welding heat-affected zone in structural steel under static and dynamic loading. 2785-2791A
Relation between microstructure, composition, and hot cracking in Ti-stabilized austenitic stainless steel weldments. 3109-3122A
- Welded joints, Microstructure**
Three-dimensional Monte Carlo simulation of grain growth in the heat-affected zone of a 2.25Cr-1Mo steel weld. 529-536B
Microstructural characterization and analysis of inclusions in C-Mn steel and weld metals. 615-628A
Dispersoid-free zones in the heat-affected zone of aluminum alloy welds. 1453-1459A
- Welded joints, Oxidation**
Relevance of high-temperature oxidation in life assessment and microstructural degradation of Cr-Mo steel weldments. 3101-3108A
- Welded joints, Phase transformations**
Microstructural evolution in ultra-low-carbon steel weldments. I. Controlled thermal cycling and continuous cooling transformation diagram of the weld metal. 2145-2153A
- Welded joints, Physical properties**
Unsteady Marangoni flow in a molten pool when welding dissimilar metals. 1387-1403B
- Welded joints, Quality control**
Modeling of inclusion growth and dissolution in the weld pool. A process model for the heat-affected zone microstructure evolution in duplex stainless steel weldments. II. Application to electron beam welding. 161-169B
A process model for the distortion induced by the electron-beam welding of a nickel-based superalloy. 1035-1048A
2261-2273A
- Welded joints, Thermal properties**
Thermal analysis of the arc welding process. I. General solutions. 1353-1370B
- Welding parameters**
Improved microstructure and properties of 6061 aluminum alloy weldments using a double-sided arc welding process. 2537-2543A
- Weldments, Oxidation**
Relevance of high-temperature oxidation in life assessment and microstructural degradation of Cr-Mo steel weldments. 3101-3108A
- Weldments, Phase transformations**
Microstructural evolution in ultra-low-carbon steel weldments. I. Controlled thermal cycling and continuous cooling transformation diagram of the weld metal. 2145-2153A
- Weldments, Quality control**
Modeling of inclusion growth and dissolution in the weld pool. A process model for the heat-affected zone microstructure evolution in duplex stainless steel weldments. II. Application to electron beam welding. 1035-1048A
- Wetting**
Optimum parameters for wetting silicon carbide by aluminum alloys. 565-573A
- Wetting, Temperature effects**
Dynamic reactive wetting and its role in hot dip coating of steel sheet with an Al-Zn-Si alloy. 1069-1079B
- Whisker composites, Thermal properties**
Thermal expansion behavior of silver matrix composites. 291-298A
- White iron, Crystal growth**
A two-dimensional model for the description of the columnar-to-equiaxed transition in competing gray and white iron eutectics and its application to calendar rolls. 2059-2068A
- White iron, Heat treatment**
The effect of rolling on graphitization characteristics of strip cast Fe-C-Si white cast iron. 275-281A
- Widmanstätten structure**
Early-stage Widmanstätten growth of the γ phase in a duplex steel. 15-19A
An investigation of the effect of fatigue deformation on the residual mechanical properties of Ti-6Al-4V ELI. 1937-1948A
Effects of microstructure on the short fatigue crack initiation and propagation characteristics of biomedical α/β titanium alloys. 1949-1958A
- Wire, Casting**
A comparative study of the microstructures observed in statically cast and continuously cast Bi-In-Sn ternary eutectic alloy. 239-248A
- Wire, Mechanical properties**
Strength and ductility of heavily drawn bundled Cu-Nb filamentary microcomposite wires with various Nb contents. 2457-2462A
- Wire drawing**
Microstructural evolution in wire-drawn Ti-22Al-26Nb powder. 2931-2941A
- Workability, Composition effects**
Effect of volume fraction of SiC_p reinforcement on the processing maps for 2124 Al matrix composites. 629-639A
- Yield strength**
Anisotropy of yielding in a Zr-2.5Nb pressure tube material. 409-420A
Comparison between high and low strain-rate deformation of tantalum. 815-823A
Effect of microstructure variations on the formation of deformation-induced martensite and associated tensile properties in a β metastable Ti alloy. 1095-1106A
The mechanical threshold stress constitutive-strength model description of HY-100 steel. 1985-1996A
Dynamic materials testing, texture, and yield-surface calculation of an automotive sheet steel. 2439-2448A
Analysis and prevention of yield strength drop during spiral piping of two high-strength API-X70 steels. 2669-2674A
- Yield strength, Alloying effects**
A comparison study of microstructure and mechanical properties of Ti-24Al-14Nb-3V-0.5Mo with and without Si. 2205-2217A
- Yield strength, Composition effects**
Microstructure and properties of in situ Al/TiB₂ composite fabricated by in-melt reaction method. 1959-1964A
Strength and ductility of heavily drawn bundled Cu-Nb filamentary microcomposite wires with various Nb contents. 2457-2462A
Influence of elastic inclusion morphology and matrix hardening behavior on Bauschinger effect in metal matrix composites. 2943-2948A
Constitutive properties of hard-alpha titanium. 3029-3040A
- Yield strength, Deformation effects**
The effect of matrix microstructure on the tensile and fatigue behavior of SiC particle-reinforced 2080 Al matrix composites. 531-540A
Load sharing between austenite and ferrite in a duplex stainless steel during cyclic loading. 1557-1570A
- Yield strength, Heating effects**
A model for predicting the effect of deformation after solution treatment on the subsequent artificial aging behavior of AA7030 and AA7108 alloys. 2327-2338A
- Yield strength, Microstructural effects**
Impact fracture toughness of porous iron and high-strength steels. 1443-1451A
The effect of processing and microstructure development on the slip and fracture behavior of the 2.1 wt.% Li AF/C-489 and 1.8 wt.% Li AF/C-458 Al-Li-C-X alloys. 1965-1976A
- Yield strength, Processing effects**
Preparation and mechanical properties of highly densified nanocrystalline Al. 1017-1024A
Characteristics of Mg-based composites synthesized using a novel mechanical disintegration and deposition technique. 1873-1881A
- Yield strength, Temperature effects**
Influence of alloying elements on the strain rate and temperature dependence of the flow stress of steels. 825-830A
Mechanical behavior of a fine-grained duplex γ -TiAl alloy. 1007-1016A
- Yttrium, Dopants**
Formation of pegs during high-temperature oxidation of Fe₃Al containing yttrium. 1685-1687A
- Yttrium compounds, Electrochemistry**
Thermodynamic and nonstoichiometric behavior of promising Hi-Tc cuprate systems via electromotive force measurements: a short review. 661-666B
- Zinc, Extraction**
Coupled experimental and thermodynamic modeling studies for metallurgical smelting and coal combustion slag systems. 621-630B
- Zinc, Reactions (chemical)**
Thermodynamic study of zinc-rich zinc-sodium alloys. 419-424B
- Zinc, Solubility**
The effect of lead on the activity of sodium in liquid zinc. 414-418B

Zinc base alloys, Coatings		
Microstructure and formability of ZnNi alloy electrodeposited sheet steel.	475-485A	
Zinc base alloys, Directional solidification		
Aligned monotectic growth in unidirectionally solidified Zn-Bi alloys.	1833-1842A	
Zinc base alloys, Mechanical properties		
Correlation between former alpha boundary growth kinetics and superplastic flow in Zn-22% Al.	163-172A	
Zinc base alloys, Phase transformations		
Influence of aging on transformation characteristics in shape memory CuZnAl alloys.	349-354A	
Zinc base alloys, Powder technology		
Neutron diffraction and phase evolution of the mechanically alloyed intermetallic compound ξ -FeZn ₁₃ .	2739-2745A	
Zinc compounds, Crystal growth		
Neutron diffraction and phase evolution of the mechanically alloyed intermetallic compound ξ -FeZn ₁₃ .	2739-2745A	
Zinc compounds, Phase transformations		
Influence of aging on transformation characteristics in shape memory CuZnAl alloys.	349-354A	
Zinc plating		
Electrodeposition of zinc from sodium zincate/hydroxide electrolytes in a spouted bed electrode.	755-766B	
Zirconium, Alloying additive		
The role of solute in grain refinement of magnesium.	2895-2906A	
Zirconium, Coatings		
Surface amorphous and crystalline microstructure by alloying zirconium using Nd:YAG pulsed laser.	3123-3127A	
Zirconium, Mechanical properties		
The influence of crystallographic texture and interstitial impurities on the mechanical behavior of zirconium.	1997-2003A	
Zirconium, Ternary systems		
Enthalpy of mixing of liquid Ni-Zr and Cu-Ni-Zr alloys.	277-284B	
Zirconium base alloys, Mechanical properties		
Anisotropy of yielding in a Zr-2.5Nb pressure tube material.	409-420A	
Anisotropic behavior and rupture of hydrided Zircaloy-4 sheets.	679-690A	
Strain-localization in sheet metal containing a geometric defect.	1883-1886A	
Zirconium base alloys, Microstructure		
Microstructural studies on lattice imperfections in deformed zirconium-base alloys by x-ray diffraction.	2405-2410A	
Zirconium dioxide, Composite materials		
Further discussion of "Particle engulfment and pushing by solidifying interfaces. II. Microgravity experiments and theoretical analysis".	1695-1700A	
Authors' reply to: Further discussion of "Particle engulfment and pushing by solidifying interfaces. II. Microgravity experiments and theoretical analysis".	1700-1704A	
Interfacial modification and impact properties of Nb/MoSi ₂ laminate composites by the addition of ZrO ₂ , NbSi ₂ , and SiC particles.	2075-2081A	
A dynamic model for the interaction between a solid particle and an advancing solid/liquid interface.	2559-2568A	
Zirconium dioxide, End uses		
Solid-state amperometric sensor for the in-situ monitoring of slag composition and transport properties.	733-753B	
Zirconium dioxide, Impurities		
Grain-growth-inhibiting effects of primary inclusion particles of ZrO ₂ and MgO in Fe-10 mass% Ni alloy.	1213-1223A	
Zirconium dioxide, Reactions (chemical)		
Phase diagram for the system CaO-Al ₂ O ₃ -ZrO ₂ .	25-33B	

